

1

# UNIVERSITY OF BRISTOL

2

## DOCTORAL THESIS

3

---

4

# **Investigating, implementing, and creating methods for analysing large neuronal ensembles**

5

---

6

*Author:*

Thomas J. DELANEY

*Supervisors:*

Dr. Cian O'DONNELL

Dr. Michael C. ASHBY

7

9 *A thesis submitted in fulfillment of the requirements*

10 *for the degree of Doctor of Philosophy*

11

*in the*

12

Biological Intelligence & Machine Learning Unit

13

Department of Computer Science

14

July 12, 2020

15

Word count: 39000



<sup>16</sup> **Declaration of Authorship**

<sup>17</sup> I declare that the work in this dissertation was carried out in accordance with the requirements of the University's Regulations and Code of Practice for Research Degree Programmes  
<sup>18</sup> and that it has not been submitted for any other academic award. Except where indicated by  
<sup>19</sup> specific reference in the text, the work is the candidate's own work. Work done in collabora-  
<sup>20</sup> tion with, or with the assistance of, others, is indicated as such. Any views expressed in the  
<sup>21</sup> dissertation are those of the author.

<sup>22</sup> Signed:

<sup>23</sup> \_\_\_\_\_

<sup>24</sup> Date:

<sup>25</sup> \_\_\_\_\_



27

## *Abstract*

28     Since the use of multi-electrode recording in neuroscience began, the number neurons  
29     being recorded in parallel has been increasing. Recently developed methods using calcium  
30     or voltage imaging have also contributed to the growth in neuronal datasets. As datasets grow,  
31     the need for new analysis methods also grows. In this research we attempted to address some  
32     of the problems associated with reading from large neuronal ensembles using fluorescent  
33     calcium indicators, and some of the problems with analysing data read from large neuronal  
34     ensembles.

35       We created a biophysical model for the fluorescence trace produced by a calcium indicator  
36     responding to a given spike train. Our model reproduced the characteristics of a real  
37     fluorescence trace recognised by spike inference algorithms. This model will be useful for  
38     anyone using or considering calcium imaging.

39       To find order in the correlated behaviour of a large multi-region neuronal ensemble, we  
40     applied a novel method from network science to detect structure and communities in corre-  
41     lated behaviour. We investigated the similarities between these communities and their brain  
42     anatomy. Our results indicate local correlated networks function at shorter timescales (<  
43     50ms), while multi-region correlated networks function over longer timescales (> 100ms).  
44     This result agrees with previous findings from EEG data, but has not been shown before using  
45     spiking data.

46       We developed a statistical model for the number of neurons spiking in a neuronal ensem-  
47     ble based on the Conway-Maxwell-binomial distribution. Our aim was to capture correlated  
48     activity in a neuronal population without measuring correlation coefficients directly. The  
49     model captured correlated activity at very short timescales better than measuring correlation  
50     coefficients. We also replicated one of the findings of Churchland et al. (2010) relating to  
51     the quenching of neural variability at stimulus onset. We propose a connection between this  
52     result and the changes in association captured by our model.



## *Acknowledgements*

54 I would like to thank my supervisors, Cian O'Donnell and Mike Ashby, for their help, en-  
55 couragement, advice, and patience over the last four years. This includes not only helping  
56 with research, but also enabling and encouraging me to make the most of my opportunities  
57 during that time. Without their help, I would not have grown as much as I have done in those  
58 years. I very grateful for their time and effort.

59 I would also like to thank the members of the Bristol Computational Neuroscience Unit  
60 for introducing me to all the various aspects of computer science, neuroscience, and machine  
61 learning, of which I otherwise would not have heard. As the first person to introduce me to  
62 the concept of mathematical neuroscience during my undergraduate days, and a great source  
63 of advice and guidance during my PhD, I would also like to thank Conor Houghton.

64 Personally, I would to thank my girlfriend Ashley, who has been nothing but helpful since  
65 I met her.

66 Finally, I would like to that my father, mother, brother and sister. I am truly fortunate to  
67 have such a good family. I thank them for their love, encouragement, and excellent example.



# 68 **Contents**

|    |  |     |
|----|--|-----|
| 69 | <b>Declaration of Authorship</b>   | iii |
| 70 | <b>Abstract</b>  | v   |
| 71 | <b>Acknowledgements</b>  | vii |
| 72 | <b>1 Introduction</b>  | 1   |
| 73 | 1.1 Overview . . . . .   | 1   |
| 74 | 1.2 Modelling the fluorescence of calcium indicators . . . . .                             | 2   |
| 75 | 1.3 Functional networks . . . . .  | 4   |
| 76 | 1.4 A new statistical model for capturing correlated behaviour . . . . .                   | 6   |
| 77 | <b>2 Sensitivity of the spikes-to-fluorescence transform to calcium indicator and neu-</b> |     |
| 78 | <b>ron properties</b>  | 9   |
| 79 | 2.1 Introduction . . . . .   | 10  |
| 80 | 2.2 Methods . . . . .  | 12  |
| 81 | 2.2.1 Calcium dynamics model . . . . .   | 12  |
| 82 | Photon release & capture . . . . .   | 14  |
| 83 | 2.2.2 Parameter optimisation . . . . .   | 15  |
| 84 | Fixed parameters . . . . .   | 16  |
| 85 | 2.2.3 Julia . . . . .  | 18  |
| 86 | 2.2.4 Spike inference . . . . .  | 18  |
| 87 | Comparing spike inference quality . . . . .  | 20  |
| 88 | 2.2.5 Perturbation analysis . . . . .  | 20  |
| 89 | 2.2.6 Signal-to-noise ratio . . . . .  | 21  |
| 90 | 2.2.7 Data sources . . . . .   | 21  |
| 91 | 2.3 Results . . . . .  | 21  |
| 92 | 2.3.1 A biophysical computational model can generate accurate fluores-                     |     |
| 93 | cence traces from spike trains . . . . .   | 21  |

|     |          |  |           |
|-----|----------|--|-----------|
| 94  | 2.3.2    | Spike inference algorithms perform similarly on real data compared<br>with time series simulated from the model . . . . .                          | 22        |
| 95  | 2.3.3    | Relative effects of various buffers to the fluorescence signal . . . . .   | 23        |
| 96  | 2.3.4    | Spike inference accuracy is sensitive to indicator properties, and likely<br>varies within and between cells . . . . .                             | 26        |
| 97  | 2.3.5    | Single spike inference accuracy drops for high firing rates, but firing<br>rate itself can be estimated from mean fluorescence amplitude . . . . . | 31        |
| 98  | 2.4      | Discussion . . . . .   | 31        |
| 102 | <b>3</b> | <b>Functional networks expand across anatomical boundaries as correlation time-<br/>scale increases</b>  | <b>35</b> |
| 103 | 3.1      | Introduction . . . . .   | 36        |
| 104 | 3.2      | Data . . . . .   | 37        |
| 105 | 3.2.1    | Brain regions . . . . .  | 37        |
| 106 | 3.2.2    | Video recordings . . . . .   | 38        |
| 107 | 3.3      | Methods . . . . .  | 38        |
| 108 | 3.3.1    | Binning data . . . . .   | 38        |
| 109 | 3.3.2    | Correlation coefficients . . . . .   | 39        |
| 110 |          | Total correlations, $r_{SC}$ . . . . .   | 39        |
| 111 |          | Shuffled total correlations . . . . .  | 40        |
| 112 |          | Separating Correlations & Anti-correlations . . . . .  | 40        |
| 113 | 3.3.3    | Conditioning on behavioural data . . . . .   | 40        |
| 114 |          | Linear regression . . . . .  | 40        |
| 115 |          | Elastic net regularisation . . . . .   | 41        |
| 116 |          | Conditional covariance . . . . .   | 41        |
| 117 |          | Measures of conditional correlation . . . . .  | 42        |
| 118 | 3.3.4    | Information Theory . . . . .   | 43        |
| 119 |          | Entropy $H(X)$ . . . . .   | 43        |
| 120 |          | Maximum entropy limit . . . . .  | 43        |
| 121 |          | Mutual Information $I(X; Y)$ . . . . .   | 44        |
| 122 |          | Variation of Information $VI(X, Y)$ . . . . .  | 46        |
| 123 |          | Measuring entropies & mutual information . . . . .   | 46        |
| 124 | 3.3.5    | Network analysis . . . . .   | 46        |
| 125 |          | Correlation networks . . . . .   | 46        |

|     |  |           |
|-----|--|-----------|
| 127 | Rectified correlations . . . . .   | 47        |
| 128 | Sparsifying data networks . . . . .  | 47        |
| 129 | Communities . . . . .  | 47        |
| 130 | Weighted configuration model . . . . .   | 48        |
| 131 | Sparse weighted configuration model . . . . .  | 48        |
| 132 | Spectral rejection . . . . .   | 48        |
| 133 | Node rejection . . . . .   | 49        |
| 134 | Community detection . . . . .  | 50        |
| 135 | 3.3.6 Clustering Comparison . . . . .  | 50        |
| 136 | Adjusted Rand Index . . . . .  | 50        |
| 137 | Clusterings as random variables . . . . .  | 51        |
| 138 | Information based similarity measures . . . . .  | 52        |
| 139 | Information based metrics . . . . .  | 52        |
| 140 | Comparing detected communities and anatomical divisions . . . . .  | 53        |
| 141 | 3.4 Results . . . . .  | 53        |
| 142 | 3.4.1 Average correlation size increases with increasing time bin width . .  | 54        |
| 143 | 3.4.2 Goodness-of-fit for Poisson and Gaussian distributions across increasing time bin widths . . . . .                     | 56        |
| 144 | 3.4.3 Differences between and inter- and intra- regional correlations decrease with increasing bin width . . . . .           | 56        |
| 145 | 3.4.4 Connected and divided structure in correlation based networks reduces in dimension with increasing bin width . . . . . | 59        |
| 146 | 3.4.5 Detecting communities in correlation based networks . . . . .  | 60        |
| 147 | 3.4.6 Functional communities resemble anatomical division at short timescales  | 63        |
| 148 | 3.4.7 Conditional correlations & signal correlations . . . . .   | 63        |
| 149 | 3.4.8 Absolute correlations and negative rectified correlations . . . . .  | 68        |
| 150 | 3.5 Discussion . . . . .   | 69        |
| 151 | <b>4 A simple two parameter distribution for modelling neuronal activity and capturing neuronal association</b>              | <b>75</b> |
| 152 | 4.1 Introduction . . . . .   | 76        |
| 153 | 4.2 Data . . . . .   | 77        |
| 154 | 4.2.1 Experimental protocol . . . . .  | 77        |
| 155 | 4.3 Methods . . . . .  | 78        |

|     |                     |   |            |
|-----|---------------------|---|------------|
| 160 | 4.3.1               | Binning data . . . . .  | 78         |
| 161 | 4.3.2               | Number of <i>active</i> neurons . . . . .   | 78         |
| 162 | 4.3.3               | Moving windows for measurements . . . . .   | 78         |
| 163 | 4.3.4               | Fano factor . . . . .   | 80         |
| 164 | 4.3.5               | Probability Distributions suitable for modelling ensemble activity . . . . .  | 80         |
| 165 |                     | Association . . . . .   | 80         |
| 166 |                     | Binomial distribution . . . . .   | 81         |
| 167 |                     | Beta-binomial distribution . . . . .  | 81         |
| 168 |                     | Conway-Maxwell-binomial distribution . . . . .  | 82         |
| 169 | 4.3.6               | Fitting . . . . .   | 84         |
| 170 | 4.3.7               | Goodness-of-fit . . . . .   | 86         |
| 171 | 4.4                 | Results . . . . .   | 86         |
| 172 | 4.4.1               | Increases in mean number of active neurons and variance in number of active neurons at stimulus onset in some regions . . . . . | 86         |
| 173 |                     | Primary visual cortex . . . . .   | 87         |
| 174 |                     | Hippocampus . . . . .   | 87         |
| 175 |                     | Thalamus . . . . .  | 87         |
| 176 | 4.4.2               | Conway-Maxwell-binomial distribution is usually a better fit than binomial or beta-binomial . . . . .                           | 87         |
| 177 | 4.4.3               | Conway-Maxwell-binomial distribution captures changes in association at stimulus onset . . . . .                                | 92         |
| 178 | 4.4.4               | Replicating stimulus related quenching of neural variability . . . . .  | 92         |
| 179 | 4.5                 | Discussion . . . . .  | 94         |
| 183 | <b>5</b>            | <b>Studies with practical limitations &amp; negative results</b>  | <b>97</b>  |
| 184 | 5.1                 | Dynamic state space model of pairwise and higher order neuronal correlations  | 98         |
| 185 | 5.2                 | A multiscale model for hierarchical data applied to neuronal data . . . . .   | 98         |
| 187 | <b>6</b>            | <b>Discussion</b>   | <b>101</b> |
| 188 | <b>Bibliography</b> |   | <b>109</b> |

# <sup>189</sup> List of Figures

|     |  |    |
|-----|--|----|
| 190 | 2.1 A: Example spike train (blue) and the corresponding GCaMP6s fluorescence       |    |
| 191 | trace (green), data replotted from (Berens et al., 2018). Inset shows zoomed       |    |
| 192 | section of traces to highlight slow decay of GCaMP6s fluorescence relative         |    |
| 193 | to spike time intervals. B: Schematic diagram of the neuron calcium and            |    |
| 194 | GCaMP computational model. C: Good visual match of data fluorescence               |    |
| 195 | trace (green) and model simulated fluorescence (orange) in response to an          |    |
| 196 | identical spike train (blue). . . . .  | 11 |
| 197 | 2.2 A: Workflow to compare spike inference for real versus simulated fluores-      |    |
| 198 | cence data. B: True positive rates achieved by three different spike inference     |    |
| 199 | algorithms when applied to observed spike trains, and simulated spike trains.      |    |
| 200 | Data points overlaid as blue circles. The performance is similar from real         |    |
| 201 | and simulated data for each of the algorithms. . . . .                             | 24 |
| 202 | 2.3 <b>Calcium Buffering Dynamics</b> (A) The proportions of bound and free cal-   |    |
| 203 | cium concentrations within a cell, with the associated spike train. (B)-(F)        |    |
| 204 | The dynamics of the concentration of (B) excited indicator bound calcium,          |    |
| 205 | (C) indicator bound calcium, (D) immobile endogenous buffer bound cal-             |    |
| 206 | cium, (E) mobile endogenous buffer bound calcium, and (F) free calcium in          |    |
| 207 | response to an action potential at $\sim 23.2\text{s}$ . . . . .                   | 25 |
| 208 | 2.4 (A) An example trace for each of the five pairs of values used for the binding |    |
| 209 | and unbinding rates of the fluorescent calcium indicator. (B) The signal-to-       |    |
| 210 | noise ratio of the modelled fluorescence traces using each of the four per-        |    |
| 211 | turbed value pairs, and the experimental value. The SNRs for the value pairs       |    |
| 212 | perturbed downward are lower than that for the unperturbed value pair or           |    |
| 213 | the higher value pairs. (C) The true-positive rates of the deconvolution al-       |    |
| 214 | gorithm's predictions when inferring from the observed data, and inferring         |    |
| 215 | from modelled traces using the perturbed and experimental values. . . . .          | 27 |

|     |  |    |
|-----|--|----|
| 216 | 2.5 (A) An example trace for each of the five perturbed values for the concentration of fluorescent calcium indicator. The top two traces are produced by the lower perturbed values, the middle trace is produced by the experimental value, and the lowest two traces are produced when using the higher perturbed values. (B) The signal-to-noise ratio of the modelled fluorescence traces using each of the four perturbed values, and the experimental value. Extreme perturbations of the concentration either above or below the experimental level lowered the SNR. (C) The true-positive rates of the deconvolution algorithm's predictions when inferring from the observed data, and inferring from modelled traces using the perturbed and experimental values. We found that the algorithms performs equally badly on the two most extreme values, and performs equally well on the experimental value, and the next higher perturbed value. . . . . | 28 |
| 229 | 2.6 (A) An example trace for each of the five perturbed values for the concentration of immobile endogenous buffer. (B) The signal-to-noise ratio of the modelled fluorescence traces using each of the four perturbed values, and the experimental value. The lower values for the immobile buffer produce the same SNR as the experimental value. But the higher perturbed values produce fluorescence traces with a lower SNR. (C) The true-positive rates of the deconvolution algorithm's predictions when inferring from the observed data, and inferring from modelled traces using the perturbed and experimental values. . . . .  | 30 |
| 238 | 2.7 <b>Simulating fluorescence traces at different firing rates</b> Example modelled traces created using simulated spike trains with a mean firing rate of 1Hz (left column), 5Hz (middle column), and 10Hz (right column). Note the difference in amplitude with different mean firing rates. . . . .  | 32 |
| 242 | 2.8 <b>Inference quality and <math>\Delta F/F_0</math> vs Firing rate</b> (left) The spike inference accuracy when applied to 30 traces created using simulated spike trains with mean firing rates of 1, 5, and 10 Hz. (right) The mean $\Delta F/F_0$ across those 30 traces for each frequency. . . . .   | 32 |
| 246 | 3.1 <b>Probe Locations:</b> The locations of the probes in each of the three mouse brains (Stringer et al., 2019). . . . .   | 38 |

|     |  |    |
|-----|--|----|
| 248 | 3.2 <b>Entropy Limit:</b> The upper limit on entropy of binned spike count data as<br>249 a function of the maximum observed spike count. The orange line is the<br>250 analytical maximum. The blue line is the entropy of samples with $N = 1000$<br>251 data points taken from the discrete uniform distribution. . . . .   | 44 |
| 252 | 3.3 (A) An example of the correlation coefficients between two different pairs<br>253 of cells, one where both cells are in the same brain region (intra-regional<br>254 pair), and one where both cells are in different brain regions (inter-regional<br>255 pair). The correlation coefficients have been measured using different time<br>256 bin widths, ranging from 5ms to 3s. Note the increasing amplitude of the<br>257 correlations with increasing bin width. (B) A raster plot showing the spike<br>258 times of each pair of cells. . . . .  | 54 |
| 259 | 3.4 Mean correlation coefficients measured from pairs of 50 randomly chosen<br>260 neurons. (A) All possible pairs, (B) positively correlated pairs, and (C) neg-<br>261 atively correlated pairs. (D) Mean and standard error of $\chi^2$ test statistics for<br>262 Poisson and Gaussian distributions fitted to neuron spike counts. . . . .  | 55 |
| 263 | 3.5 (Left)The mean intra-region and inter-region correlations using all possible<br>264 pairs of $\sim 500$ neurons, spread across 9 different brain regions. (Right)<br>265 Courtesy of Stringer et al. (2019), mean inter-regional (out-of-area) corre-<br>266 lation coefficients vs mean intra-regional (within-area) correlation coefficients<br>267 for a bin width of 1.2s. Note that the intra-regional coefficients are higher in<br>268 each case. . . . .   | 57 |
| 269 | 3.6 The mean intra-regional correlations (coloured dots) and mean inter-regional<br>270 correlations (black dots) for a given region, indicated on the x-axis, for dif-<br>271 ferent time bin widths. Each black dot represents the mean inter-regional<br>272 correlations between the region indicated on the x-axis and one other region.<br>273 (A) shows these measurements when we used a time bin width of 5ms. (B)<br>274 shows these measurements when we used a time bin width of 1s. Note that<br>275 the difference between the mean inter-regional correlations and mean intra-<br>276 regional correlations is smaller for 1s bins. . . . . | 58 |
| 277 | 3.7 Mean inter-regional (main diagonal) and intra-regional (off diagonal) corre-<br>278 lation coefficients. (A) Shows these measurements when spike times were<br>279 binned using 5ms time bins. (B) Shows the same, using 1s time bins. Note<br>280 that the matrices are ordered according to the main diagonal values, therefore<br>281 the ordering is different in each subfigure. . . . .  | 59 |

|     |  |    |
|-----|--|----|
| 282 | 3.8 The number of dimensions in the $k$ -partite and connected structure in the cor-             |    |
| 283 | relation based networks beyond the structure captured by a sparse weighted                       |    |
| 284 | configuration null network model (see section 3.3.5), shown for different time                   |    |
| 285 | bin widths. Note that the $k$ -partite structure disappears for time bin width                   |    |
| 286 | greater than 200ms for all three subjects. The dimension of the connected                        |    |
| 287 | structure reduces with increasing bin width for 2 of the 3 subjects (top row). . . . .           | 61 |
| 288 | 3.9 (A-B) Correlation matrices with detected communities indicated by white                      |    |
| 289 | lines. Each off main diagonal entry in the matrix represents a pair of neu-                      |    |
| 290 | rons. Those entries within a white square indicate that both of those neurons                    |    |
| 291 | are in the same community as detected by our community detection proce-                          |    |
| 292 | dure. Matrices shown are for 5ms and 1s time bin widths respectively. Main                       |    |
| 293 | diagonal entries were set to 0. (C-D) Matrices showing the anatomical dis-                       |    |
| 294 | tribution of pairs along with their community membership. Entries where                          |    |
| 295 | both cells are in the same region are given a colour indicated by the colour                     |    |
| 296 | bar. Entries where cells are in different regions are given the grey colour also                 |    |
| 297 | indicated by the colour bar. . . . .   | 62 |
| 298 | 3.10 (A) The variation of information is a measure of distance between cluster-                  |    |
| 299 | ings. The distance between the anatomical ‘clustering’ and community de-                         |    |
| 300 | tection ‘clustering’ increases with increasing time bin width. (B) The ad-                       |    |
| 301 | justed Rand index is a normalised similarity measure between clusterings.                        |    |
| 302 | The anatomical and community detection clusterings become less similar as                        |    |
| 303 | the time bin width increases. . . . .  | 64 |
| 304 | 3.11 Comparing the components of the total covariance across different values for                |    |
| 305 | the time bin width. We observed a consistent increase in $E[\text{cov}(X, Y Z)]$ as              |    |
| 306 | the time bin width increased. But we saw different trends for $\text{cov}(E[X Z], E[Y Z])$       |    |
| 307 | for each mouse. . . . .  | 65 |
| 308 | 3.12 Comparing the components of the total covariance across different values for                |    |
| 309 | the time bin width. We saw a consistent increase in $\rho_{X,Y Z}$ as the time bin               |    |
| 310 | width increased in all three subjects. But we saw different trends in $\rho_{\text{signal}}$ for |    |
| 311 | each of the subjects. . . . .  | 66 |

|     |  |    |
|-----|--|----|
| 312 | 3.13 Matrices showing the regional membership of pairs by colour, and the com-                   |    |
| 313 | munities in which those pairs lie. (A-B) Detected communities and regional                       |    |
| 314 | membership matrix for network based on rectified spike count correlation                         |    |
| 315 | $\rho_{X,Y Z}$ , using time bin widths of 0.005s and 1s respectively. (C-D) Detected             |    |
| 316 | communities and regional membership matrix for network based on rectified                        |    |
| 317 | signal correlation $\rho_{\text{signal}}$ , using time bin widths of 0.005s and 1s respectively. | 67 |
| 318 | 3.14 Distance and similarity measures between the anatomical division of the neu-                |    |
| 319 | rons, and the communities detected in the network based on the spike count                       |    |
| 320 | correlations $\rho_{X,Y Z}$ . (A) The variation of information is a ‘distance’ mea-              |    |
| 321 | sure between clusterings. The distance between the anatomical ‘clustering’                       |    |
| 322 | and the community clustering increases as the time bin width increases. (B)                      |    |
| 323 | The adjusted Rand index is a similarity measure between clusterings. The                         |    |
| 324 | detected communities become less similar to the anatomical division of the                       |    |
| 325 | cells as the time bin width increases. . . . .   | 68 |
| 326 | 3.15 Distance and similarity measures between the anatomical division of the neu-                |    |
| 327 | rons, and the communities detected in the network based on the signal cor-                       |    |
| 328 | relations $\rho_{\text{signal}}$ . (A) The variation of information is a ‘distance’ measure be-  |    |
| 329 | tween clusterings. The distance between the anatomical ‘clustering’ and the                      |    |
| 330 | community clustering increases as the time bin width increases. (B) The ad-                      |    |
| 331 | justed Rand index is a similarity measure between clusterings. The detected                      |    |
| 332 | communities become less similar to the anatomical division of the cells as                       |    |
| 333 | the time bin width increases. . . . .  | 69 |
| 334 | 3.16 (A-B) Absolute correlation matrices with detected communities indicated by                  |    |
| 335 | white lines. These communities are based on the absolute value of the total                      |    |
| 336 | correlation between each pair of cells. Those entries within a white square in-                  |    |
| 337 | dicate that both of those neurons are in the same community. Matrices shown                      |    |
| 338 | are for 5ms and 1s time bin widths respectively. Main diagonal entries were                      |    |
| 339 | set to 0. (C-D) Matrices showing the anatomical distribution of pairs along                      |    |
| 340 | with their community membership. Regional membership is indicated by the                         |    |
| 341 | colour bar. (E) Variation of information between the anatomical division of                      |    |
| 342 | the cells, and the detected communities. (F) Adjusted Rand index between                         |    |
| 343 | the anatomical division, and the detected communities. . . . .                                   | 70 |

|     |   |    |
|-----|---|----|
| 344 | 3.17 (A-B) Sign reversed rectified correlation matrices with detected communities indicated by white lines. Those entries within a white square indicate that both of those neurons are in the same community. Matrices shown are for 5ms and 1s time bin widths respectively. Main diagonal entries were set to 0. (C-D) Matrices showing the anatomical distribution of pairs along with their community membership. Regional membership is indicated by the colour bar. (E) Variation of information between the anatomical division of the cells, and the detected communities. (F) Adjusted Rand index between the anatomical division, and the detected communities. . . . .                            | 71 |
| 353 | 4.1 Figures showing the over-dispersion possible for a beta-binomial distribution relative to a binomial distribution. Parameters are shown in the captions. . .  | 82 |
| 355 | 4.2 Figures showing (A) the under-dispersion and (B) over-dispersion permitted by the COMb distribution relative to a binomial distribution. (C) illustrates that the $p$ parameter of the COMb distribution does not correspond to the mean of the distribution, as it does for the binomial and beta-binomial distributions. (D) shows a heatmap for the value of the Kullback-Liebler divergence between the COMb distribution and the standard binomial distribution with same value for $n$ , as a function of $p$ and $\nu$ . Parameters are shown in the captions. . . . .   | 85 |
| 363 | 4.3 (A) Raster plot showing the spikes fired by 33 randomly chosen neurons in the primary visual cortex. (B-C) (B) average and (C) variance of the number of active neurons, measured using a sliding window 100ms wide, split into 100 bins. The midpoint of the time interval for each window is used as the timepoint (x-axis point) for the measurements using that window. The grey shaded area indicates the presence of a visual stimulus. The opaque line is an average across the 160 trials that included a visual stimulus of any kind. We can see a transient increase in the average number of active neurons and the variance of this number, followed by a fluctuation and another increase. . | 88 |

|     |   |    |
|-----|---|----|
| 372 | 4.4 (A) Raster plot showing the spikes fired by 33 randomly chosen neurons in   |    |
| 373 | the hippocampus. (B-C) (B) average and (C) variance of the number of active     |    |
| 374 | neurons, measured using a sliding window 100ms wide, split into 100 bins.       |    |
| 375 | The midpoint of the time interval for each window is used as the timepoint (x-  |    |
| 376 | axis point) for the measurements using that window. The grey shaded area        |    |
| 377 | indicates the presence of a visual stimulus. The opaque line is an average      |    |
| 378 | across the 160 trials that included a visual stimulus of any kind. We can see   |    |
| 379 | a transient increase in the average number of active neurons and the variance   |    |
| 380 | of this number at stimulus onset. . . . .                                       | 89 |
| 381 | 4.5 (A) Raster plot showing the spikes fired by 33 randomly chosen neurons in   |    |
| 382 | the thalamus. (B-C) (B) average and (C) variance of the number of active        |    |
| 383 | neurons, measured using a sliding window 100ms wide, split into 100 bins.       |    |
| 384 | The midpoint of the time interval for each window is used as the timepoint (x-  |    |
| 385 | axis point) for the measurements using that window. The grey shaded area        |    |
| 386 | indicates the presence of a visual stimulus. The opaque line is an average      |    |
| 387 | across the 160 trials that included a visual stimulus of any kind. We can       |    |
| 388 | see in immediate increase at stimulus onset, a subsequent fall, and another     |    |
| 389 | sustained increased until the stimulus presentation ends. . . . .               | 90 |
| 390 | 4.6 (A) An example of the binomial, beta-binomial, and Conway-Maxwell-binomial  |    |
| 391 | distributions fitted to a sample of neural activity. The Conway-Maxwell-        |    |
| 392 | binomial distribution is the best fit in this case. The histogram shows the     |    |
| 393 | empirical distribution of the sample. The probability mass function of each     |    |
| 394 | distribution is indicated by a different coloured line. (B) Across all samples  |    |
| 395 | in all trials, the proportion of samples for which each fitted distribution was |    |
| 396 | the the best fit. The Conway-Maxwell-binomial distribution was the best fit     |    |
| 397 | for 93% of the samples taken from V1 using a bin width of 1ms. . . . .          | 91 |

|     |   |    |
|-----|---|----|
| 398 | 4.7 (A) We fit a Conway-Maxwell-binomial distribution to the number of active       |    |
| 399 | neurons in 1ms time bins of a 100ms sliding window. We did this for all             |    |
| 400 | trials with a visual stimulus and took the average across those trials. We see      |    |
| 401 | a transient drop in value for the distribution's $\nu$ parameter at stimulus onset. |    |
| 402 | This shows an increase in positive association between the neurons. (B) We          |    |
| 403 | measured the correlation coefficient between the spike counts of all possible       |    |
| 404 | pairs of neurons in the same sliding window. The took the average of those          |    |
| 405 | coefficients. We also did this for every visually stimulated trial, and took the    |    |
| 406 | average across trials. The increase in positive association is not reflected with   |    |
| 407 | an increase in average correlation. . . . .   | 93 |
| 408 | 4.8 (A) The mean Fano factor of the spike counts of the cells in the primary visual |    |
| 409 | cortex. Means were taken across cells first, then across trials. There was a        |    |
| 410 | significant decrease in the Fano factors immediately after stimulus onset. (B)      |    |
| 411 | The mean Fano factor of the spike counts of the cells in the motor cortex. No       |    |
| 412 | significant change in measurements at any point. . . . .                            | 94 |

# <sup>413</sup> List of Tables

|     |   |    |
|-----|---|----|
| 414 | <b>2.1 Fixed parameters</b> A table of the parameters fixed before optimising the   |    |
| 415 | model. The values of these parameters could be changed to model differ-             |    |
| 416 | ent fluorescent calcium indicators. . . . .   | 17 |
| 417 | 4.1 Details of the different bin width and analysis window sizes used when bin-     |    |
| 418 | ning spike times, and analysing those data. . . . .                                 | 79 |
| 419 | 4.2 Relative dispersion of the COMb distribution, and association between Bernoulli |    |
| 420 | variables as represented by the value of the $\nu$ parameter. . . . .               | 84 |
| 421 | 4.3 Proportion of samples for which each distribution was the best fit, grouped     |    |
| 422 | by bin width. The COMb distribution is the best fit most of the time. . . . .       | 92 |



# List of Abbreviations

**COMb** Conway-Maxwell-binomial (distribution)

**OASIS** Online active set method to infer spikes

**SNR** Signal to noise ratio



# List of Symbols

|             |   |                   |
|-------------|---|-------------------|
| $[Ca^{2+}]$ | Free calcium concentration                  | mol               |
| $[BCa]$     | Fluorescent indicator bound calcium         | mol               |
| $[ECa]$     | Endogenous mobile buffer bound calcium      | mol               |
| $[ImCa]$    | Immobile mobile buffer bound calcium        | mol               |
| $[BCa^*]$   | excited fluorescent indicator bound calcium | mol               |
| $k_{X_f}$   | binding (affinity) rate                     | $mol^{-1} s^{-1}$ |
| $k_{X_b}$   | unbinding (dissociation) rate               | $s^{-1}$          |



425 **Chapter 1**

426 **Introduction**

427 **1.1 Overview**

428 Since Hodgkin and Huxley's squid experiments featuring a single axon (Hodgkin and Hux-  
429 ley, 1939), to more recent research with spike sorted data from  $\sim 24000$  neurons from 34  
430 brain regions from 21 mice (Allen et al., 2019), the number of neurons contributing to elec-  
431 trophysiological datasets has been growing. The number of simultaneously recorded neurons  
432 has doubled approximately every seven years since the use of multi-electrode recording in  
433 neuroscience began (Stevenson and Kording, 2011). Recording methods using two-photon  
434 calcium imaging have also been used to extract data from populations containing over 10000  
435 neurons (Peron et al., 2015). This dramatic growth in the number of neurons available for  
436 analysis requires a dramatic change in analysis methods.

437 There are multiple methods for reading activity from neuronal ensembles: electrophysiolog-  
438 ical, calcium imaging, and voltage imaging. Electrophysiology involves inserting electrodes  
439 into the brain of an animal. The electrodes read extra-cellular membrane potential, and using  
440 these readings we observe activity in the ensemble. Calcium imaging and voltage imaging  
441 use indicator dyes or fluorescent proteins that emit fluorescence traces that indicate either  
442 the concentration of calcium in a neuron's cytoplasm, or the neuron's membrane potential.  
443 In this project, we have attempted to address some of the difficulties in collecting data from  
444 these large ensembles using fluorescent calcium indicators, and some of the difficulties in  
445 analysing the collected data.

446 The rest of this introductory chapter will give some background about methods of record-  
447 ing from the brain, and some background for the rest of the document. Chapter two describes  
448 a biophysical model for the fluorescence trace induced by a given spike train in a cell con-  
449 taining a fluorescent calcium indicator. Our third chapter describes our investigations into

450 the correlated activity across different regions of a mouse behaving spontaneously. We ap-  
451 plied a novel community detection method (Humphries et al., 2019) from network science  
452 to correlation based networks of neurons, and observed differences in the structure of these  
453 correlations at different timescales. In our fourth chapter, we detail a new statistical model  
454 for the number of neurons spiking in a neuronal ensemble at any given moment. With this  
455 model, we attempted to capture correlated activity in a new way. The fifth chapter is a brief  
456 description of the work that yielded negative results or was abandoned. The final chapter is a  
457 discussion of our work and results from the previous chapters and their implications.

## 458 1.2 Modelling the fluorescence of calcium indicators

459 To focus on calcium imaging for a start, a neuron that contains a fluorescent calcium indicator  
460 in its cytoplasm will fluoresce when bombarded with photons. The amount that the cell  
461 will fluoresce is dependent on the concentration of fluorescent indicator within the cell, and  
462 the concentration of calcium within the cell. When a neuron fires an action potential, the  
463 influx of free calcium ions causes an increase in fluorescence when those ions bond with the  
464 fluorescent indicator and those bounded molecules are bombarded with photons. After the  
465 action potential, as calcium is extruded from the cell the fluorescence returns to a baseline  
466 level. This is the basic mechanism of fluorescent calcium indicator based imaging.

467 This method has some advantages over electrophysiology as measure of neuronal ensem-  
468 ble activity. Many of the problems with electrophysiology are within the processes used to  
469 isolate spikes in the extracellular voltage readings, and assign these spikes to individual cells.  
470 These processes are collectively called ‘spike sorting’. A comparison of many different spike  
471 sorting algorithms found that these algorithms only agreed on a fraction of cases (Buccino  
472 et al., 2019). Furthermore, because electrodes measure extracellular voltage, neurons that do  
473 not spike will not be detected. Isolating individual neurons is easier and more reliable when  
474 using calcium imaging data, because cells will emit a baseline level of fluorescence when not  
475 firing action potentials. Another advantage is that calcium imaging sites can be re-used for  
476 weeks for longitudinal studies (Chen et al., 2013). One of the methods of delivering the flu-  
477 orescent indicator is by adeno-associated viruses, consequently there can be problems with  
478 indicator gradients around the infection site, and expression levels will change in individual  
479 cells over weeks (Tian et al., 2009; Chen et al., 2013). This delivery method can also cause  
480 cell pathology, and nuclear filling (Zariwala et al., 2012), but these problems can be solved by  
481 using lines of transgenic mice (Dana et al., 2014). The fluorescence signal itself can serve a a

482 good indicator of cell activity, but similarly to electrophysiology, the aim of calcium imaging  
483 is often spike detection.

484 If the imaging data is collected at a high enough frequency, and the signal-to-noise ratio  
485 of the fluorescence trace is high enough, it should be possible to infer the spike times to some  
486 level of accuracy. For example, the calmodulin based indicator GCaMP6s has a sufficiently  
487 high signal-to-noise ratio that isolated action potentials can be detected and inferred (Chen  
488 et al., 2013). Many spike inference algorithms exist (Vogelstein et al., 2010; Pnevmatikakis  
489 et al., 2016; Friedrich and Paninski, 2016; Pnevmatikakis et al., 2013; Pnevmatikakis et al.,  
490 2014; Deneux et al., 2016; Greenberg et al., 2018), and some of these can perform both cell  
491 isolation and spike detection simultaneously (Vogelstein et al., 2010; Pnevmatikakis et al.,  
492 2016; Pnevmatikakis et al., 2014; Deneux et al., 2016). But the relationship between spik-  
493 ing and fluorescence change is not fully understood. For example, the fluorescent indicator  
494 will act like an additional calcium buffer within the cell cytoplasm and will compete with  
495 the other endogenous buffers to bind with free calcium ions. Therefore, the concentration  
496 of those endogenous buffers, and the binding dynamics of those buffers will have an effect  
497 on the change in fluorescence in response to an action potential. Furthermore, the binding  
498 dynamics of the fluorescent indicator itself will have an effect on the change in fluorescence.  
499 For example, the GCaMP series of fluorescence indicators are based on the calcium buffer  
500 protein calmodulin. This protein has four binding sites, whose affinities interact non-linearly.  
501 But most of the spike inference algorithms model the fluorescence as a linear function of  
502 a calcium trace, and they model this calcium trace as a first or second order autoregression  
503 with a pulse input to represent action potentials. Deneux et al. (2016) developed two dif-  
504 ferent calcium fluorescence models behind their spike inference algorithm (MLspike) with a  
505 more biological inspiration. For their simpler model, they take a physiological approach and  
506 account for baseline calcium indicator dynamics. They end up with a system of first order  
507 differential equations defining the dynamics of calcium concentration, baseline fluorescence,  
508 and fluorescence. For their more complicated model specifically for genetically encoded cal-  
509 cium indicators, they also took into account indicator binding and unbinding rates, which  
510 added another equation to their system of equations. The algorithms that use the autore-  
511 gression model and the MLspike algorithm are outperformed by the most recently published  
512 spike inference algorithm (Greenberg et al., 2018). This algorithm takes into account the  
513 binding dynamics of both the endogenous buffers and fluorescent calcium indicator, and the  
514 concentrations of free calcium, indicator, and endogenous buffer within the cell cytoplasm.  
515 The performance of this algorithm shows that there is value in more biologically inspired

516 models of fluorescent calcium indicators.

517 In light of the growing popularity of two-photon calcium imaging, and the lack of biolog-  
518 ically inspired spike inference algorithms (Greenberg et al. developed their spike inference  
519 algorithm in parallel to our work), we decided to develop a biologically inspired model for  
520 fluorescent calcium indicator fluorescence. The idea being that our model would take a spike  
521 train, or simply spike times, provided by the user, and return the fluorescence trace that would  
522 be induced by this spike train or spike times. The model contains parameters for concentra-  
523 tions of indicator and endogenous buffers, as well as affinity and unbinding rates for these  
524 buffers. There are also parameters for the baseline concentration of free calcium in the cell  
525 cytoplasm, and the cell radius (as a means for calculating the cell volume). With this model,  
526 we hoped that experimentalists would be able to test out different calcium indicators on the  
527 types of spike trains that they expect to encounter. This way they could decide ahead of time  
528 which indicator suited their situation best. Since the output of our model is a fluorescence  
529 trace, the spike inference models mentioned above can be applied to the modelled fluores-  
530 cence. This means that the model could also be used to benchmark the performance of these  
531 spike inference algorithms, and to investigate the impact of variations in the model on spike  
532 inference accuracy.

### 533 1.3 Functional networks

534 We have outlined some of the advantages that calcium imaging has over electrophysiology.  
535 But electrophysiology is more useful in some situations. One particular drawback for two-  
536 photon calcium imaging is that usually it can only be used for imaging near to the surface  
537 of the brain. This problem can be solved by removing the tissue around the area to be im-  
538 aged, and custom building a two-photon microscope Dombeck et al., 2010. Imaging with  
539 three (or presumably more) photons may solve this problem in the future (Ouzounov et al.,  
540 2017). A better option for reading activity from neurons beyond the surface of the brain is to  
541 use Neuropixels probes (Jun et al., 2017). These probes can be used to read from thousands  
542 of neurons simultaneously in many different areas of the brain (Allen et al., 2019; Stringer  
543 et al., 2019; Steinmetz, Carandini, and Harris, 2019; Steinmetz et al., 2019). This brings us  
544 to another problem for which we require new innovations in our analysis methods. Specif-  
545 ically, analysing correlated behaviour in neural ensembles consisting of neurons from many  
546 different brain regions.

547 Until the invention of new technologies such as the Neuropixels probes, most elec-  
548 trophysiology datasets read from neurons in only one or two regions. Therefore most of  
549 the research on interactions between neurons in different regions is limited to two regions  
550 (Wierzynski et al., 2009; Patterson et al., 2014; Girard, Hupé, and Bullier, 2001). In chapters  
551 3 and 4 we used datasets with neurons from 9 and 5 different brain regions respectively. In  
552 their review of the interaction between growing the number of neurons in datasets and the  
553 analysis methods applied to those dataset, Stevenson and Kording (2011) assert that an im-  
554 portant objective of computational neuroscience is to find order in these kinds multi-neuron  
555 of datasets. This was our main aim for the research described in chapter 3.

556 In light of recent findings based on correlated behaviour showing that spontaneous be-  
557 haviours explain activity in many different parts of the brain that would otherwise be regarded  
558 as noise (Stringer et al., 2019), that satiety is represented brain wide (Allen et al., 2019), and  
559 that exploratory and non-exploratory states are represented in the amygdala (Gründemann  
560 et al., 2019), it was clear that state representation or motor control had an influence on cor-  
561 related behaviour in areas of the brain not usually associated with these tasks. Also, given  
562 differences in timescales of fluctuations in different brain regions (Murray et al., 2014), and  
563 different timescales for event representation in different brain regions (Baldassano et al.,  
564 2017), we decided to investigate brain wide correlated behaviour at timescales ranging from  
565 5ms up to 3s.

566 We started off measuring the correlations in spike counts between individual neurons in  
567 our ensemble. These measurements induced a weighted undirected graph where each node  
568 represented a neuron, and the weight of each edge was the strength of the correlation be-  
569 tween the neurons represented by the nodes at either end of that edge. In order to put the  
570 neurons into groups with correlated behaviour, we applied a novel community detection al-  
571 gorithm (Humphries et al., 2019) to this graph. We repeated this analysis for timescales  
572 from milliseconds to seconds. Bear in mind that our correlation based graph was completely  
573 agnostic of the anatomical regions in which our cells resided. We then compared our corre-  
574 lated communities to their anatomy at each timescale. In this way, we used a novel method,  
575 never applied neuronal data before, to analyse the makeup of correlated communities across  
576 different regions at different timescales.

## 577 1.4 A new statistical model for capturing correlated behaviour

578 Many important findings have been made by measuring the correlations between binned  
 579 spike counts, but there are some problems with this method of analysis. Firstly, the width  
 580 of the bins used to bin spike times into spike counts has an effect on the magnitude of the  
 581 correlations measured. Using a short bin width can cause your measurements to be artificially  
 582 small (Cohen and Kohn, 2011). This may not be an issue if one is considering relative size of  
 583 correlations when using the same bin width, but it is still not ideal. Secondly, while pairwise  
 584 correlations can capture most of the information in a small network (up to 40 cells) of highly  
 585 correlated cells (Schneidman et al., 2006), a model based on pairwise correlations alone will  
 586 fail to capture the activity of larger ( $\sim 100$  cells) networks, higher order correlated activity  
 587 is required (Ganmor, Segev, and Schneidman, 2011). One problem with these higher order  
 588 correlations is that they may be defined in different ways (Staude, Grün, and Rotter, 2010).  
 589 Furthermore if we want to include them in a model this usually involves greatly increasing the  
 590 number of parameters to fit, which increases the dimension of the parameter space leading  
 591 to the ‘curse of dimensionality’. Some models attempt to sidestep these problems while  
 592 still capturing higher-order correlations. These models attempt to capture the relationship  
 593 between each individual neuron in the ensemble, and the ensemble as a whole. Okun et al  
 594 (2015) called the strength of this relationship the ‘population coupling’, and demonstrated  
 595 that this quantity can predict an individual neuron’s response to optogenetic stimulation of  
 596 the whole ensemble. They also showed that this quantity was an indicator of the neuron’s  
 597 synaptic connectivity (Okun et al., 2015). With the ‘population tracking model’, O’Donnell  
 598 et al. (2016) linked the probability of firing an action potential for each individual neuron  
 599 with the distribution of the number of active neurons. This allowed model fitting for a large  
 600 number of neurons, as well as calculation of full pattern probabilities, and population entropy  
 601 (O’Donnell et al., 2017).

602 In this work, we also aimed to capture correlated behaviour between the neurons in a  
 603 neuronal ensemble without measuring correlations directly. Correlation coefficients capture  
 604 the linear component of the relationship between two random variables, but will not mea-  
 605 sure any relationship beyond linearity. Also, measuring correlation coefficients using short  
 606 timebins can be difficult for neuronal data (Cohen and Kohn, 2011). We decided to abandon  
 607 correlation, and we aimed to quantify a more general concept of association by modelling  
 608 the number of active neurons in the ensemble using a Conway-Maxwell-binomial (COMb)  
 609 distribution (Kadane, 2016).

610        The COMb distribution is a probability distribution over the number of successes in a  
611        sequence of Bernoulli trials, where these trials can be associated in some way. The COMb  
612        distribution is an extension of the standard binomial distribution, with an additional parameter  
613        to model association between the Bernoulli variables. Using this additional parameter the  
614        distribution can capture positive association, where the Bernoulli variables tend to take the  
615        same value, negative association, where the Bernoulli variables tend to take opposite values,  
616        or no association i.e. the standard binomial distribution.

617        We fit a COMb distribution to spike sorted electrophysiological data taken from five  
618        different regions in the brain of an awake mouse exposed to visual stimuli (Steinmetz et al.,  
619        2019). We examined whether or not a model based on the COMb distribution was able to  
620        capture changes in the number of active neurons in these neuronal ensembles in response to  
621        the stimuli. We also investigated the relationship between the changes as captured by the  
622        COMb model and the change in neural variability as measured by Churchland et al. in their  
623        famous paper (Churchland et al., 2010).

624        Our overall aim was to investigate some of the challenges in analysing large ensembles  
625        of neurons present today. That included collecting the data to analyse (via calcium imaging),  
626        and subsequently analysing these data. We felt that this was a worthwhile project because  
627        the size of datasets, in terms of numbers of neurons and data collected, is growing rapidly.  
628        Consequently these challenges will only become greater unless they are addressed. This is  
629        our attempt at addressing them.



630 **Chapter 2**

631 **Sensitivity of the**  
632 **spikes-to-fluorescence transform to**  
633 **calcium indicator and neuron**  
634 **properties**

635 *Abstract*

636 Fluorescent calcium indicators such as GCaMP are widely used to monitor neuronal activity.  
637 However the relationship between the fluorescence signal and the underlying action potential  
638 firing is poorly understood. This lack of knowledge makes it difficult for experimenters  
639 to decide between different indicator variants for a given application. We addressed this  
640 problem by studying a basic biophysical model of calcium dynamics in neuronal soma. We  
641 fit the model parameters to publicly available data where GCaMP6s fluorescence and whole-  
642 cell electrophysiological recordings were made simultaneously in the same single neurons.  
643 We systematically varied the model's parameters to characterise the sensitivity of spike train  
644 inference algorithms to the calcium indicator's main biophysical properties: binding rate,  
645 dissociation rate, and molecular concentration. This model should have two potential uses:  
646 experimental researchers may use it to help them select the optimal indicator for their desired  
647 experiment; and computational researchers may use it to generate simulated data to aid design  
648 of spike inference algorithms.

649 **2.1 Introduction**

650 Although fluorescent calcium indicators such as GCaMP are widely used to monitor neuronal  
651 activity, the relationship between the fluorescence signal and the underlying action potential  
652 firing is imperfect. The fluorescence signal has a low signal-to-noise ratio, and most indica-  
653 tors' kinetics are slow relative to the millisecond-timescale dynamics of the membrane volt-  
654 age (example in figure 2.1A). This makes spike inference difficult. Furthermore, the effects  
655 of the indicator and cell properties on the fluorescence signal are unknown. For example,  
656 genetically encoded indicators can accumulate within neurons over weeks and months (Chen  
657 et al., 2013). Studies using calcium-sensitive fluorescent dyes have shown that indicator con-  
658 centration has substantial effects on the spike-to-fluorescence relationship (Maravall et al.,  
659 2000). Therefore spike rates inferred from GCaMP fluorescence signals may give mislead-  
660 ing results if comparing across imaging sessions. More generally, the poor understanding of  
661 the spike-to-fluorescence transform means experimenters may not know whether to trust the  
662 outputs of spike train inference methods in any given application.

663 Spike trains are usually inferred from the time series of intensity values of one pixel of the  
664 fluorescence image, where the pixel is located at the cell's soma. The problems of identifying  
665 these pixels, and inferring spikes from their time series can solved separately or together.  
666 When attempting to infer spikes, the fluorescence trace is modelled as a linear combination of  
667 calcium concentration dynamics, a baseline calcium concentration, and some Gaussian noise.  
668 The calcium concentration dynamics are modelled as an autoregressive process of degree 1  
669 or 2 with a pulse input corresponding to the spike train, or the number of spikes fired in a  
670 time step. The model includes no dynamics for the fluorescent indicator itself. Furthermore,  
671 in order to make this model into an easily solvable linear programming problem the number  
672 of spikes fired in a timestep is not restricted to non-negative integers but to arbitrary non-  
673 negative values (Vogelstein et al., 2010; Pnevmatikakis et al., 2016; Friedrich and Paninski,  
674 2016; Pnevmatikakis et al., 2013; Pnevmatikakis et al., 2014). More biologically inspired  
675 spike inference models do exist (Deneux et al., 2016), but their fundamentals are very similar.  
676 In this work, we investigated the effect of changing dynamics and buffer concentrations on  
677 the accuracy of the inference algorithms based on these models.

678 The aim of this project was to model the fluorescence traces produced by a fluorescent  
679 calcium indicator in a neuron soma resulting from a specific spike train, given calcium indi-  
680 cator parameters such as binding rate, dissociation rate, and molecular concentration. Such

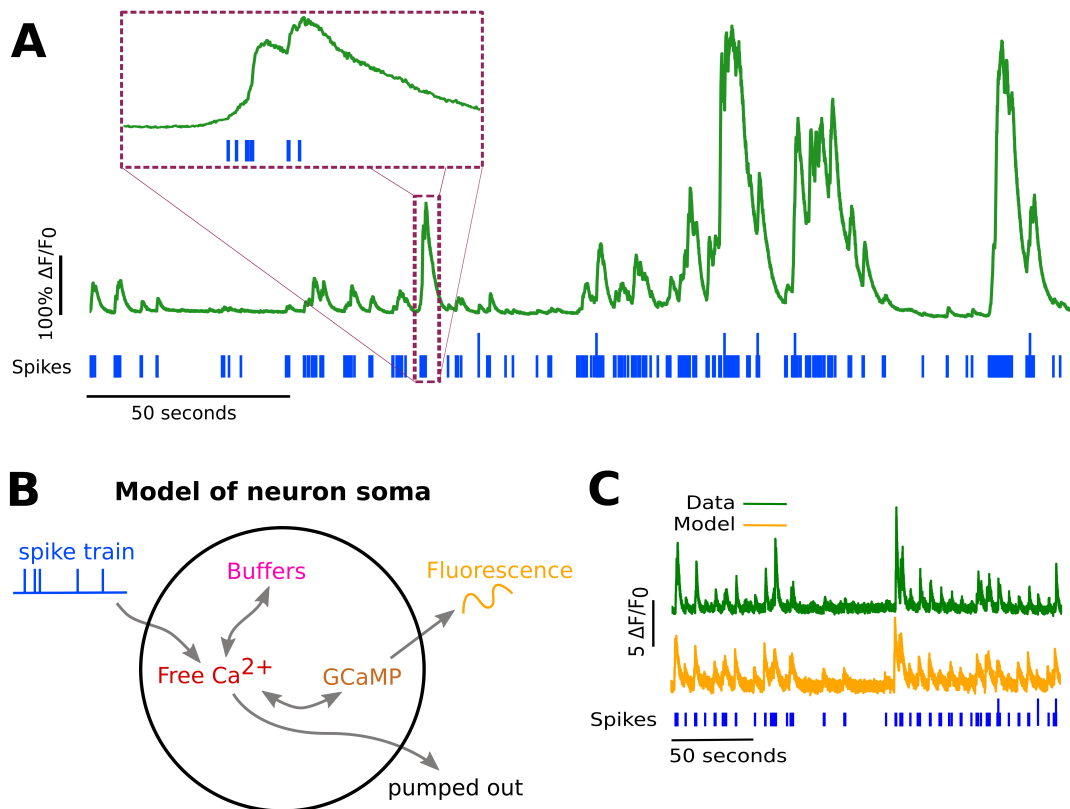


FIGURE 2.1:

A: Example spike train (blue) and the corresponding GCaMP6s fluorescence trace (green), data replotted from (Berens et al., 2018). Inset shows zoomed section of traces to highlight slow decay of GCaMP6s fluorescence relative to spike time intervals.

B: Schematic diagram of the neuron calcium and GCaMP computational model.

C: Good visual match of data fluorescence trace (green) and model simulated fluorescence (orange) in response to an identical spike train (blue).

681 a model would allow benchmarking of various spike inference algorithms, and enable under-  
682 standing of how indicator characteristics affect the quality of spike train inference.

683 The model we developed consisted of free calcium, fluorescent indicator molecules, and  
684 mobile and immobile endogenous calcium buffers. The indicator molecules which were  
685 bound to a calcium molecule could be either excited, i.e. able to release a photon, or relaxed.  
686 In order to reproduce the noise inherent in the data collection, we modelled the release of  
687 photons from the excited indicator bound calcium as a stochastic process.

688 The fluorescence traces produced by the simulation were calibrated to reproduce the  
689 signal-to-noise ratio observed in experimental data. Previously published spike inference  
690 algorithms were then used to infer spike trains from the experimental fluorescence traces and  
691 the modelled fluorescence traces. The parameters of the model were then varied in order to  
692 determine the effect on the system dynamics and the effects on spike inference.

## 693 2.2 Methods

### 694 2.2.1 Calcium dynamics model

695 We wrote a biophysical model of the calcium dynamics within a cell soma. When a neuron  
696 fires an action potential, voltage-dependent calcium ion-channels open up that allow a current  
697 of calcium ions ( $\text{Ca}^{2+}$ ) to flow into the neuron (Koch, 1999). The increase in the free calcium  
698 ion concentration inside of the cell, along with changes in the concentration of potassium  
699 and sodium, causes the change in cell membrane potential, which must be depolarised. The  
700 depolarising process consists of free calcium ions leaving the cell through open ion channels,  
701 or binding to molecules within the cell called buffers, or calcium storage by organelles such  
702 as the endoplasmic reticulum. A diagram illustrating the cell, its channels, and its buffers  
703 can be seen in figure 2.1A. There are several different types of calcium buffer, each with  
704 different dynamics and different concentrations within different types of excitable cell. The  
705 fluorescent calcium indicator is another calcium buffer, with the useful property that when it  
706 is bound to a calcium ion, the bound molecule may become excited by a photon and release  
707 a photon in return. This is what creates the fluorescence. After the action potential has taken  
708 place, the free calcium concentration within the cell will return to a baseline level (Maravall  
709 et al., 2000).

710 We modelled the the dynamics of five molecular concentrations,

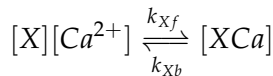
- 711 • Free calcium ion concentration,  $[\text{Ca}^{2+}]$

## 2.2. Methods

---

- 712     • Fluorescent indicator bound calcium,  $[BCa]$   
713     • Endogenous mobile buffer bound calcium,  $[ECa]$   
714     • Endogenous immobile buffer bound calcium,  $[ImCa]$   
715     • Excited buffered calcium,  $[BCa^*]$

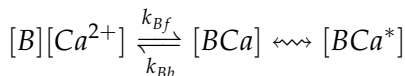
The term ‘buffering’ refers to free calcium ions coming into contact with buffer molecules followed by the binding of those molecules. Diagrammatically:



716 where  $[X]$  represents any buffer molecule, and  $k_{X_f}$  and  $k_{X_b}$  represent the binding (affinity)  
717 and unbinding (dissociation) rates in units of per molar concentration per second ( $M^{-1} s^{-1}$ )  
718 and per second ( $s^{-1}$ ) respectively. The speed of this chemical reaction is determined by the  
719 binding and unbinding rates.

720 There are a number different endogenous buffers in any neuron. Which buffers are  
721 present, and the buffers’ concentrations vary from cell to cell. In order to capture the ef-  
722 fects of mobile and immobile endogenous buffers without introducing several parameters,  
723 they were modelled as two buffers. One representing mobile buffers and the other represent-  
724 ing immobile buffers. Each with their own binding and unbinding rates.

The fluorescent calcium indicator behaves similarly to the other calcium buffers. The calcium is buffered by the indicator in the same way. But an indicator bound calcium molecule can become excited by absorbing the energy from a photon. An excited indicator bound calcium molecule can then release a photon to go back to its ‘relaxed’ state.



725 The released photons are captured by a photon collector. This gives us the fluorescence trace.  
726 Ignoring the baseline level of free calcium in a neuron, the system of equations we used  
727 to model all of these interactions is as follows:

$$\begin{aligned} \frac{d[Ca^{2+}]}{dt} = & k_{Bb}[BCa] + k_{Eb}[ECa] + k_{Imb}[ImCa] \\ & - k_{Bf}[B][Ca^{2+}] - k_{Ef}[E][Ca^{2+}] - k_{Imf}[Im][Ca^{2+}] \\ & + \beta([Ca_0^{2+}] - [Ca^{2+}]) \end{aligned} \quad (2.1)$$

$$\frac{d[BCa]}{dt} = k_{Bf}[B][Ca^{2+}] - k_{Bb}[BCa] + r[BCa^*] - \eta[BCa] \quad (2.2)$$

$$\frac{d[ECa]}{dt} = k_{Ef}[E][Ca^{2+}] - k_{Eb}[ECa] \quad (2.3)$$

$$\frac{d[ImCa]}{dt} = k_{Imf}[Im][Ca^{2+}] - k_{Imb}[ImCa] \quad (2.4)$$

$$\frac{d[BCa^*]}{dt} = \eta[BCa] - r[BCa^*] \quad (2.5)$$

728 where  $[Ca_0^{2+}]$  is the baseline calcium concentration within the cell soma,  $\beta$  is a rate defining  
729 how quickly free calcium enters or leaves the cell in the absence of an action potential,  $\eta$   
730 is the excitation rate for indicator bound calcium,  $r$  is the photon release rate for the excited  
731 indicator bound calcium, and  $f$  and  $b$  are used to indicate the forward and backward rates  
732 for chemical reactions respectively. The excitation rate defines the proportion of indicator  
733 bound calcium that becomes excited at each time step. The photon release rate defines the  
734 proportion of excited indicator bound calcium that releases a photon and returns to its relaxed  
735 state at each time step. An action potential is modelled as a discontinuous increase in the free  
736 calcium concentration to an appropriate value (Maravall et al., 2000).

737 Note that each of the three pairs of binding and unbinding terms in the first equation has a  
738 corresponding pair in one of the subsequent three equations. Binding removes a free calcium  
739 molecule and adds a bound calcium molecule, and unbinding does the opposite.

740 When using this model to simulate a fluorescence trace, the system of equations above are  
741 first solved over a period of 25s without action potentials. This lets each of the five tracked  
742 chemical concentrations reach their steady state. Then we use the given spike train and the  
743 parameters to model the fluorescence trace.

744 Note that since the model has no spatial component, the mobile and immobile buffers  
745 only differ in their binding and unbinding rates.

#### 746 Photon release & capture

747 We used a simple model for the photon release. The number of photons released at each time  
748 step was controlled by the number of excited indicator bound calcium molecules in the cell  
749 and a parameter called the ‘release rate’. The release rate is an optimised free parameter of  
750 the model.

751 As for the photon capture, in two-photon excitation microscopy the photons scattered  
752 by the fluorescent indicator get scattered in all directions. Therefore the number of photons  
753 detected is stochastic. This made the process for capturing photons the natural source of  
754 noise in the system. The number of photons captured, and therefore the intensity of the

## 2.2. Methods

---

755 fluorescence, is modelled using a binomial distribution. The number of photons released was  
756 used as the number of trials. The probability of success, or ‘capture rate’ was a free parameter  
757 of the model that we optimised.

### 758 2.2.2 Parameter optimisation

759 The free parameters of the model are as follows:

760 **Calcium rate,  $\beta$**  Controls how quickly the concentration of free calcium will be driven to  
761 the baseline concentration.

762 **Capture rate,  $p$**  The average proportion of photons captured by the photon detector.

763 **Excitation rate,  $\eta$**  The number of indicator bound calcium molecules that become excited  
764 by photon bombardment at each time step.

765 **Release rate,  $r$**  The number of excited indicator bound calcium molecules that release a  
766 photon at each time step.

767 To optimise the free parameters given a fluorescence trace, we applied the following proce-  
768 dure:

- 769 1. The frequency power spectrum of the trace was measured.
- 770 2. The power spectrum was smoothed using a boxcar smoother (aka. sliding average, box  
771 smoother).
- 772 3. The log of the smoothed power spectrum was measured.
- 773 4. Use the model to create a modelled fluorescence trace.
- 774 5. Apply steps 1, 2, and 3 to the modelled fluorescence trace.
- 775 6. Calculate the root mean squared difference between the log power of the actual fluo-  
776 rescence trace, and the log power of the modelled fluorescence trace.
- 777 7. Calculate the root mean squared difference between the actual fluorescence trace and  
778 the modelled fluorescence trace.
- 779 8. Use an optimisation algorithm to reapply this process, attempting to minimize the sum  
780 of the two root mean squared differences at each iteration.

781 Using the root mean squared difference of the log power spectra as part of the objective  
782 function forces the model to match the noise frequency of the actual fluorescence. Using  
783 the root mean squared difference of the traces themselves forces the model to match the  
784 amplitude of the fluorescence trace more accurately.

785 In order to minimise the objective function, a suite of meta-heuristic optimisation (aka.  
786 black-box optimisation) algorithms were implemented on each of the traces in the dataset.  
787 These methods were chosen because they don't require a gradient for the objective function  
788 (gradient-free) and they are particularly useful for minimising stochastic objective functions  
789 like the one we used here. The free parameters were optimised for each individual fluores-  
790 cence trace. The most successful method for each trace was recorded. The method that was  
791 most often successful was probabilistic descent, and the second most successful method was  
792 generating set search. Both of these methods are examples of pattern search. These two  
793 methods were the best optimisers on about 75% of the traces in the dataset.

794 Although this optimisation procedure minimises the value of the optimisation function,  
795 the value never reaches zero for a number of reasons. Firstly, the fluorescence traces carry  
796 low frequency fluctuations that cannot be captured by the model. Secondly, the model as-  
797 sumes that the process of calcium binding to the fluorescent indicator is linear in time (see  
798 equation 1), but there are more complicated dynamics involved here. Fluorescent calcium  
799 indicators, the GCaMP series for example, are often built upon the calcium binding protein  
800 called 'calmodulin'. This protein has four calcium binding sites. These sites are locally split  
801 into two pairs. Each pair has a different affinity for calcium, and the affinity of the binding  
802 sites is affected by the occupancy of the other binding sites (Kilhoffer et al., 1992). So the  
803 calcium to calcium indicator binding process is non-linear, but the model does not take this  
804 into account.

### 805 **Fixed parameters**

806 As well as the optimised parameters mentioned in section 2.2.2, the model also has thirteen  
807 fixed parameters. Please see table 2.1 for details of these parameters and their values. In  
808 an application of the model, these parameters can be changed in order to model any given  
809 fluorescent calcium indicator, or even prospective indicators that only exist in theory.

## 2.2. Methods

---

| Parameter   | Description   | Value                            | Source                   |
|-------------|---|----------------------------------|--------------------------|
| baseline    | The baseline concentration of free calcium within the cell soma                           | $4.5 \times 10^{-8} M$           | (Maravall et al., 2000)  |
| cell radius | The radius of the soma (assumed to be spherical)  | $10^{-5} M$                      | (Fiala and Harris, 1999) |
| endogenous  | The concentration of endogenous mobile buffer within the cell soma                        | $10^{-4} M$                      | (Faas et al., 2011)      |
| frequency   | The frequency at which the spike trains are sampled.                                      | 100Hz                            |                          |
| immobile    | The concentration of endogenous immobile buffer within the cell soma                      | $7.87 \times 10^{-5} M$          | (Bartol et al., 2015)    |
| indicator   | The concentration of fluorescent indicator within the cell soma                           | $10^{-4} M$                      | (Maravall et al., 2000)  |
| $k_{Bb}$    | The unbinding rate of the fluorescent calcium indicator                                   | $160 s^{-1}$                     | (Bartol et al., 2015)    |
| $k_{Bf}$    | The binding rate of the fluorescent calcium indicator                                     | $7.77 \times 10^8 s^{-1} M^{-1}$ | (Bartol et al., 2015)    |
| $k_{Eb}$    | The unbinding rate of the endogenous mobile buffer  | $10^4 s^{-1}$                    | (Bartol et al., 2015)    |
| $k_{ef}$    | The binding rate of the endogenous mobile buffer  | $10^8 s^{-1} M^{-1}$             | (Bartol et al., 2015)    |
| $k_{Imb}$   | The unbinding rate of the endogenous immobile buffer                                      | $524 s^{-1}$                     | (Bartol et al., 2015)    |
| $k_{Imf}$   | The binding rate of the endogenous immobile buffer  | $2.47 \times 10^8 s^{-1} M^{-1}$ | (Bartol et al., 2015)    |
| peak        | The increase in free calcium concentration within the cell induced by an action potential | $2.9 \times 10^{-7} M$           | (Maravall et al., 2000)  |

TABLE 2.1: **Fixed parameters** A table of the parameters fixed before optimising the model. The values of these parameters could be changed to model different fluorescent calcium indicators.

810 **2.2.3 Julia**

811 The programming language used to write and execute the model was ‘Julia’. Julia is a dy-  
812 namic programming language designed for technical computing. Julia was designed specif-  
813 ically to provide a convenient high-level dynamic language similar to MATLAB, or Python,  
814 with improved performance. Julia’s type system and Julia’s direct interfaces with C and  
815 Fortran allow this aim to be achieved (Bezanson et al., 2012). The Julia version of the  
816 ‘Sundials’ package for ODE solving was used to solve the system of equations above. The  
817 BlackBoxOptim.jl package for Julia was used to perform the optimisation.

818 **2.2.4 Spike inference**

819 We used spike inference algorithms to compare the quality of spike inference using the mod-  
820 eled traces to the quality of spike inference using the observed traces. We also used the  
821 spike inference algorithms to assess the effect of parameter perturbation on the spike infer-  
822 ence. Three algorithms were used:

823 **Constrained non-negative matrix deconvolution algorithm (aka CNMD algorithm)** The  
824 underlying model models the fluorescence as a linear function of a calcium trace with  
825 additional noise. This calcium trace is a first order autoregression with a pulse input to  
826 represent action potentials. This algorithm uses a constrained version of non-negative  
827 Weiner deconvolution to infer a calcium signal and a ‘spiking activity signal’ from the  
828 fluorescence trace (Vogelstein et al., 2010; Pnevmatikakis et al., 2016). The spiking ac-  
829 tivity signal is a non-negative vector of real numbers reflecting the cell’s activity rather  
830 than an actual spike train. We inferred a spike train by choosing an optimised thresh-  
831 old for the spiking activity signal. Whenever the spiking activity signal exceeded that  
832 threshold, an action potential was inferred. The threshold was optimised by minimis-  
833 ing the difference between the number of spikes observed and the number of spikes  
834 predicted.

835 **MLSpike algorithm** Deneux et al. (2016) developed two different calcium fluorescence  
836 models behind their spike inference algorithm (MLspike) with a more biological in-  
837 spiration. For their simpler model, they take a physiological approach and account for  
838 baseline calcium indicator dynamics. They end up with a system of first order differen-  
839 tial equations defining the dynamics of calcium concentration, baseline fluorescence,  
840 and fluorescence. For their more complicated model specifically for genetically en-  
841 coded calcium indicators, they also took into account indicator binding and unbinding

## 2.2. Methods

---

842 rates, which added another equation to their system of equations. This algorithm uses a  
843 generalised version of the Viterbi algorithm to return the spike train that maximises the  
844 likelihood of producing the given fluorescence trace. The Viterbi algorithm is an algo-  
845 rithm for estimating the most likely sequence of hidden states resulting in a sequence  
846 of observed states in a discrete-time finite-state Markov process (Forney, 1973). In this  
847 case, each hidden state is defined by the presence or absence of an action potential, and  
848 each observed state is the value of the fluorescence trace at each time step. (Deneux  
849 et al., 2016).

850 **Online Active Set method to Infer Spikes (OASIS)** This algorithm is once again based on  
851 an auto-regressive model of the fluorescence trace, but can be generalised to any or-  
852 der. Both the first and second order versions can be fit to a spike train in a reasonable  
853 time. The algorithm itself is a generalisation of the pool adjacent violators algorithm  
854 (PAVA) that is used in isotonic regression. The OASIS algorithm works through the  
855 fluorescence trace from beginning to end, this combined with the speed of the algo-  
856 rithm means that it could be used for real-time online spike inference (Friedrich and  
857 Paninski, 2016). Given a fluorescence trace, the algorithm will return the most likely  
858 spike train and an inferred denoised fluorescence signal.

859 In order to quantify the quality of spike inference for a given algorithm, we ran that algorithm  
860 on all of the fluorescence traces in dataset number eight of the spike finder datasets. Then we  
861 measured some binary classification measures on the results. These measures included

- 862     ● Accuracy
- 863     ● True positive rate (aka recall, sensitivity, hit rate)
- 864     ● True negative rate (aka specificity)
- 865     ● Precision
- 866     ● Negative predicted value
- 867     ● False negative rate (aka miss rate)
- 868     ● False positive rate (aka fall-out)
- 869     ● False discovery rate
- 870     ● False omission rate

871 In making these measurements, we allowed a tolerance of two subsequent time bins for spike  
872 prediction. For example, the spike train data is a vector of 0s and 1s, with one element for  
873 each time bin. A ‘0’ denotes inactivity, a ‘1’ denotes the presence of at least one action  
874 potential. The inferred spike trains produced by the spike inference algorithms take the same  
875 form. In our analysis, if a spike appeared in the inferred spike train up to two time frames  
876 after a spike in the observed spike train, that spike was considered correctly inferred i.e. a  
877 true positive. However, once a spike in the inferred spike train was matched to a spike from  
878 the observed spike train, the inferred spike could not be matched to another observed spike.  
879 To illustrate, if two spikes were inferred in the two time bins following an isolated observed  
880 spike, the first inferred spike was considered correctly inferred, but the second inferred spike  
881 was considered incorrectly inferred, i.e. a false positive.

882 The most useful measure was the true positive rate. This is because the spiking is sparse  
883 and this measurement is sensitive to the number of spikes observed and inferred, but is not  
884 affected by the true negative or false negative rates. After optimising the parameters for each  
885 fluorescence trace we measured the spike inference quality for the observed fluorescence  
886 traces, and compared this to the spike inference quality for the modelled traces.

887 When measuring the spike inference quality for higher frequency spike train (1 – 10Hz),  
888 we used the accuracy as our binary classification measure. At these frequencies the variance  
889 of the fluorescence trace was much higher than for sparser spiking regimes, therefore we  
890 wanted to take into account the number of false negatives inferred by the algorithm.

891 **Comparing spike inference quality**

892 In order to compare spike inference quality we had to use methods for comparing samples.  
893 When comparing the true positive rate distributions arising from two different datasets, or  
894 two different algorithms on the same dataset, we compared the distributions using a paired  
895 t-test.

896 **2.2.5 Perturbation analysis**

897 In order to measure the sensitivity of spike inference to changes in a given model parameter,  
898 we perturbed the parameter and compared the quality of spike inference with the perturbed  
899 parameters to the quality of spike inference with the experimental or optimised parameters.  
900 In order to maximise the possibility of observing a difference due to the perturbation, we  
901 perturbed the chosen parameter by a relatively large amount. For example, the experimen-  
902 tal value for the molar concentration of the fluorescent indicator within the cell was  $10^{-4}M$

### 2.3. Results

---

903 (Maravall et al., 2000). The perturbed values used for this parameter were  $10^{-2}M$ ,  $10^{-3}M$ ,  
904  $10^{-5}M$ , and  $10^{-6}M$ . The quality of the inference was compared by measuring the true posi-  
905 tive rate for each perturbed value and using a t-test to compare the distributions of the results.

906 This analysis was performed firstly without any optimisation of the free parameters for  
907 use with the perturbed parameters. Then the analysis was performed after the optimised  
908 parameters for each perturbed value were calculated.

#### 909 2.2.6 Signal-to-noise ratio

910 To assess the effect of perturbation on the modelled traces, we measured and compared the  
911 signal to noise ratio (SNR) on each of the modelled traces. We calculated the SNR as the  
912 peak change in fluorescence divided by the standard deviation of the baseline fluctuation of  
913 the fluorescence trace (Tada et al., 2014). We measured these values by running the model  
914 on a spike train consisting a long period of inactivity followed by one action potential. We  
915 ran the model on this spike train one hundred times. We then measured the mean change  
916 in fluorescence and standard deviation of baseline activity across the one hundred modelled  
917 fluorescence traces, and calculated the SNR.

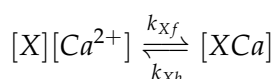
#### 918 2.2.7 Data sources

919 All of the data used in this project was sourced from the ‘Spike Finder’ project ([spikefinder.codeneuro.org](http://spikefinder.codeneuro.org)).  
920 The data consisted of a collection of datasets with simultaneously measured fluorescence  
921 traces and action potentials (Berens et al., 2018).

## 922 2.3 Results

### 923 2.3.1 A biophysical computational model can generate accurate fluorescence 924 traces from spike trains

To study the relationship between action potential firing and calcium fluorescence, we built a computational model of calcium dynamics in a neuronal soma. The model consisted of four dynamic variables: the concentration of free calcium, two types of endogenous buffer, and the calcium-sensitive fluorescent indicator. Each of the buffers and the indicator could independently bind and unbind with calcium. These reactions were modelled as



925 where  $X$  is the buffer concentration and  $Ca^{2+}$  is the calcium concentration. Each species  
926 could therefore exist in two states: either bound with calcium or unbound. To model the  
927 imaging process, we also added a third, excited state to the indicator. When in the calcium-  
928 bound state, the indicator could be converted to an excited state, corresponding to the absorp-  
929 tion of a photon. The rate of this excitation process could be interpreted as the intensity of  
930 the light illuminating the sample. Once excited, the species decayed back to the unexcited  
931 state at a fixed rate, corresponding to the spontaneous emission of photons. The total emitted  
932 fluorescence signal was interpreted as proportional to this de-excitation flux. To represent  
933 experimental noise in the photon capture process, we drew a random number of captured  
934 photons at each time step from a binomial distribution, parameterised by a number  $p$  that  
935 corresponds to the mean fraction of released photons that are captured.

936 The model had 17 parameters in total describing the molecules' concentrations and re-  
937 action rates (Methods). We set 13 of these parameters to values from the literature. The  
938 remaining 4 parameter values we fit to publicly-available data (Berens et al., 2018), briefly  
939 explained as follows (see Methods for full details). Single neurons from acute rat cortical  
940 slices expressing GCaMP6f were imaged with two-photon microscopy while the membrane  
941 potentials of the somata of the same neurons were simultaneously recorded via whole-cell  
942 patch clamp electrophysiology. In this dataset, the electrical recordings give unambiguous  
943 information about neurons' spike times. To do the parameter fitting, we feed these spike  
944 trains as inputs to the computational model. After running, the model returns a simulated  
945 fluorescence trace. We aimed to find the model parameter values that give the best match  
946 between this simulated fluorescence trace and the real fluorescence time series recorded in  
947 the corresponding neuron. To do this we used a suite of optimisation procedures to jointly  
948 fit both the real neuron's fluorescence time series and power spectrum, which capture com-  
949 plementary information about the spikes-to-fluorescence mapping (Methods). We performed  
950 the fitting procedure independently for each of the 20 neurons in the spikefinder dataset  
951 (<http://spikefinder.org>). After fitting, the model produced realistic-looking fluorescence time  
952 series (Figure 2.1).

953 **2.3.2 Spike inference algorithms perform similarly on real data compared with  
954 time series simulated from the model**

955 Researchers often pass the fluorescence time series through a spike inference tool before per-  
956 forming further statistical analyses. These spike inference algorithms take the fluorescence  
957 trace as input and attempt to estimate the neuronal spike train that triggered them (Vogelstein

## 2.3. Results

---

et al., 2010; Pnevmatikakis et al., 2016; Friedrich and Paninski, 2016; Pnevmatikakis et al., 2013; Pnevmatikakis et al., 2014; Deneux et al., 2016). Part of our motivation for building this model was to allow us to ask the question on non-linearities properties of the cell and the calcium indicator affect the quality of spike inference? In order to trust the conclusions from our model, we should first be confident that spike inference from our simulated fluorescence traces is similar to that from the real data. To test this we passed each of the simulated fluorescence traces through three previously published spike inference algorithms, quantified their performance against the ground-truth electrophysiology data, repeated the procedure for the real calcium fluorescence time series, and compared the accuracy of the inference processes in all cases. The *true positive rate*, also known as the *recall*, the *sensitivity*, or the *probability of detection* of spike inference varied across the three inference algorithms we tried ( $p$  value and statistical test here). The constrained non-negative matrix deconvolution algorithm (Pnevmatikakis et al., 2016) (CNMD algorithm) correctly detected approximately 45% of the true spikes, the OASIS algorithm (Friedrich and Paninski, 2016) correctly detected approximately 35% of the true spikes, and the ML spike algorithm (Deneux et al., 2016) correctly detected approximately 15% of the true spikes (see figure 2.2). Notably, for two of the three inference algorithms, the quality of inference was also fairly consistent for individual spike trains, not just the group means ( $p > 0.05$ , paired t-test). This demonstrates that the models were generating fluorescence time series that were similarly difficult to decode as the real data, in ways that were not specific to any one inference algorithm. This is evidence that the models captured real aspects of the spikes-to-fluorescence transform.

### 2.3.3 Relative effects of various buffers to the fluorescence signal

One of the benefits of computational models over laboratory experiments is that we can observe all the variables in the simulation to gain insight into the system's dynamics, which can be difficult to do in the lab. We plotted the concentrations of the various species over time for a version of the model fit to one data set, in response to the same train of spikes used for fitting (figure 2.3). Figure 2.3a shows the absolute values of the species concentrations, summed. Consistent with experimental estimates (Maravall et al., 2000), only a small fraction ( $\sim 0.1\%$ ) of calcium is free and unbound to any buffer. Of the bound calcium, the vast majority, ( $\sim 96\%$ ) is bound to the GCaMP indicator. The two types of endogenous buffer are bound to the remaining calcium ( $\sim 4\%$ ). An influx of calcium from a single spike adds very little to the total calcium, in relative terms (red line in Figure 3a).

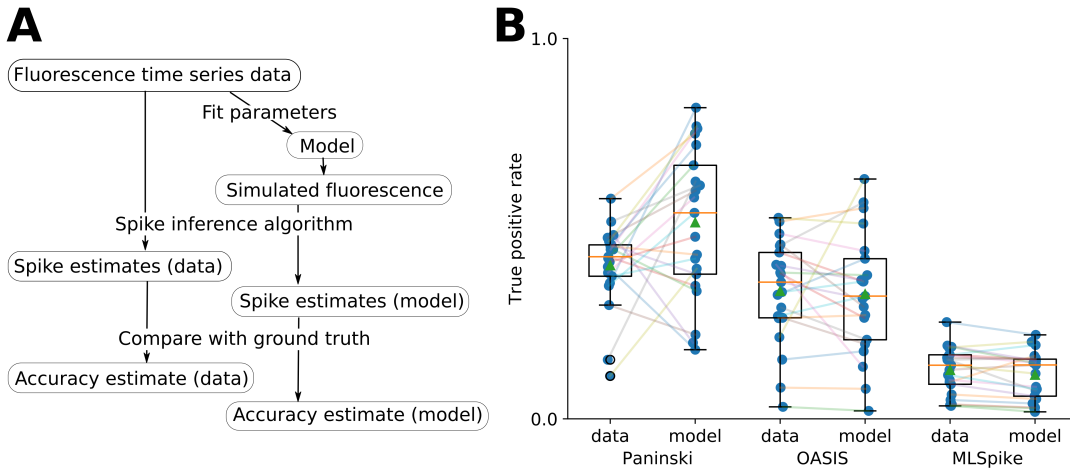


FIGURE 2.2:  
A: Workflow to compare spike inference for real versus simulated fluorescence data.  
B: True positive rates achieved by three different spike inference algorithms when applied to observed spike trains, and simulated spike trains. Data points overlaid as blue circles. The performance is similar from real and simulated data for each of the algorithms.  
quantities

When calcium entered the model neuron it was rapidly buffered (Bartol et al., 2015). However the relative fractions of which buffer molecules bound to the influxed calcium was dynamic, and changed over time . Figure 2.3 (b-f) shows the time course of the various species over time in response to a calcium influx event from a single action potential. Crucially, the indicator  $[BCa]$  competed with the endogenous buffers  $[ImCa]$  and  $[ECa]$  – all three bind calcium on similar timescales. This implies that the timecourse and amplitude of the  $[BCa]$  variable will also depend on the binding rates and availabilities of the endogenous buffers. For example if we decreased the concentration of an endogenous buffer, we might expect both a faster rise time and greater peak amplitude of the  $[BCa]$  signal in response to a calcium influx event. The slowest component of the decay had a similar time constant for  $[BCa]$ ,  $[ImCa]$  and  $[ECa]$ , which in turn matched the  $[Ca]$  extrusion time constant in our model ( $\sim 6.29 \times 10^{-22} \text{Ms}^{-1}$ ). This implies that the buffers and the indicator had reached a dynamic equilibrium and were jointly tracking the free calcium concentration as calcium was slowly extruded from the cell.

Interestingly the excited bound calcium species ( $[BCa^*]$ ) showed a qualitatively different timecourse in response to a calcium influx event. This concentration is subject to the added ‘excitation and release’ dynamic, where a certain proportion of the concentration absorbs the energy from an incoming photon and goes into an ‘excited state’ at each time step. A certain proportion of the concentration releases a photon and reverts to a ‘relaxed state’ at each

### 2.3. Results

---

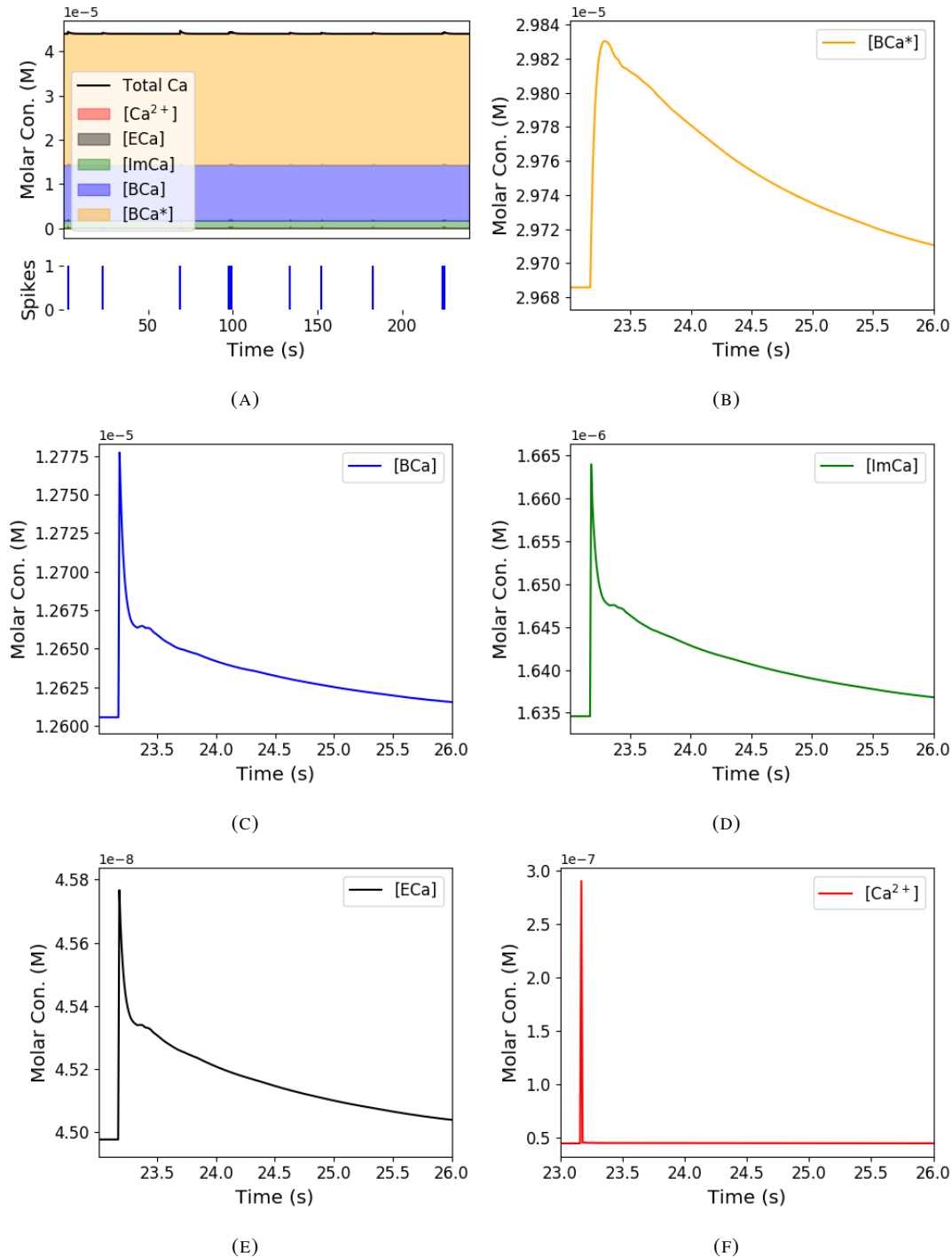


**FIGURE 2.3: Calcium Buffering Dynamics** (A) The proportions of bound and free calcium concentrations within a cell, with the associated spike train. (B)-(F) The dynamics of the concentration of (B) excited indicator bound calcium, (C) indicator bound calcium, (D) immobile endogenous buffer bound calcium, (E) mobile endogenous buffer bound calcium, and (F) free calcium in response to an action potential at  $\sim 23.2$ s.

1009 timestep also. This means that the excited bound calcium lags behind the bound calcium  
1010 trace. We could think of the excited bound calcium trace as a low pass filtered version of the  
1011 bound calcium trace.

1012 **2.3.4 Spike inference accuracy is sensitive to indicator properties, and likely  
1013 varies within and between cells**

1014 The above results imply that the fluorescence signal depends on the relative properties of  
1015 both GCaMP and the endogenous buffers. We next used the model to directly ask how  
1016 sensitive spike inference was to these components. We focused on three key parameters that  
1017 likely vary from cell to cell and experiment to experiment: GCaMP binding kinetics, GCaMP  
1018 concentration, and endogenous buffer concentration.

1019 Several variants of GCaMP itself have been made that differ in calcium binding kinetics,  
1020 baseline fluorescence, fluorescence efficiency, and other factors. For example, GCaMP6f has  
1021 a decay time constant of  $\sim 1\text{s}$ , while GCaMP6s has a decay time constant of  $\sim 2\text{s}$  (Chen  
1022 et al., 2013). Here we asked how these differences in binding kinetics affect spike inference.  
1023 We jointly varied the calcium binding and unbinding rates of the indicator by the same factor  
1024 over a range from 100-fold slower to 100-fold faster from the fitted values, and simulated the  
1025 fluorescence response for each of the parameter settings in response to the same spike trains  
1026 as before (figure 2.4). Notably this manipulation does not affect the indicators affinity, and  
1027 therefore would not affect steady-state responses to prolonged changes in calcium. Instead  
1028 it is likely to affect its sensitivity to the spike train dynamics. We computed two summary  
1029 measures from the simulated fluorescence traces: the signal-to-noise ratio for a single spike  
1030 (Methods, section 2.2.6), and the accuracy of spike inference for each of the spike trains. We  
1031 observed a reduction in the signal-to-noise ratio and the spike inference quality when we set  
1032 the binding and unbinding rates were set to one hundredth of their fitted values, and to one  
1033 tenth of their fitted values. When we increased the value of both binding rates, we observed  
1034 no change in these measurements. The reduction in both rates lead to smaller increases in  
1035 fluorescence in response to an action potential and a longer decay time (figure 2.4a), this  
1036 caused the reduction in signal-to-noise ratio. As both rates were increased, the change in  
1037  $\Delta F/F_0$  in response to an action potential increased and the decay time decreased slightly,  
1038 but the fluorescence trace created by these values was very similar to the trace created by the  
1039 fitted values.

1040 Second, the overall concentrations of GCaMP often varies from cell to cell. For exam-  
1041 ple different cells, even of the same type in the same tissue, can express different levels of

### 2.3. Results

---

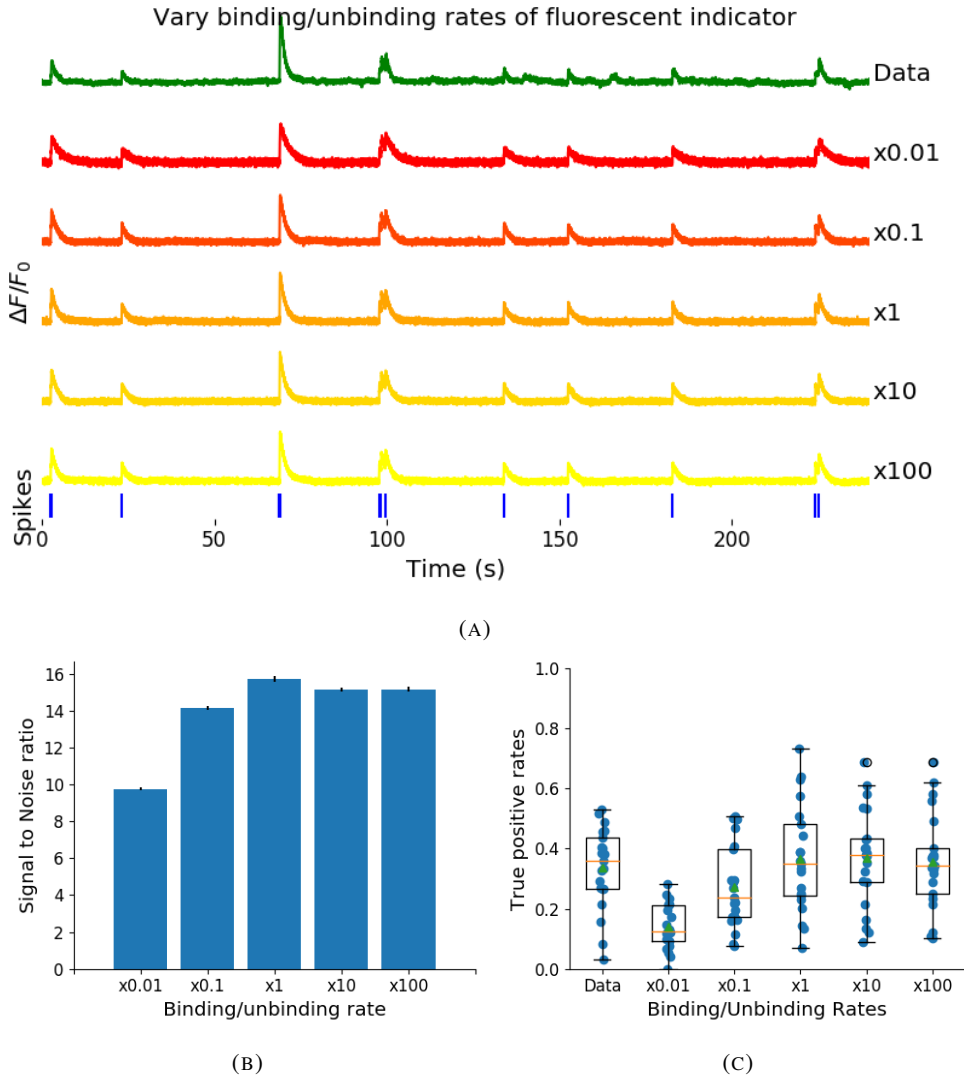


FIGURE 2.4: (A) An example trace for each of the five pairs of values used for the binding and unbinding rates of the fluorescent calcium indicator. (B) The signal-to-noise ratio of the modelled fluorescence traces using each of the four perturbed value pairs, and the experimental value. The SNRs for the value pairs perturbed downward are lower than that for the unperturbed value pair or the higher value pairs. (C) The true-positive rates of the deconvolution algorithm's predictions when inferring from the observed data, and inferring from modelled traces using the perturbed and experimental values.

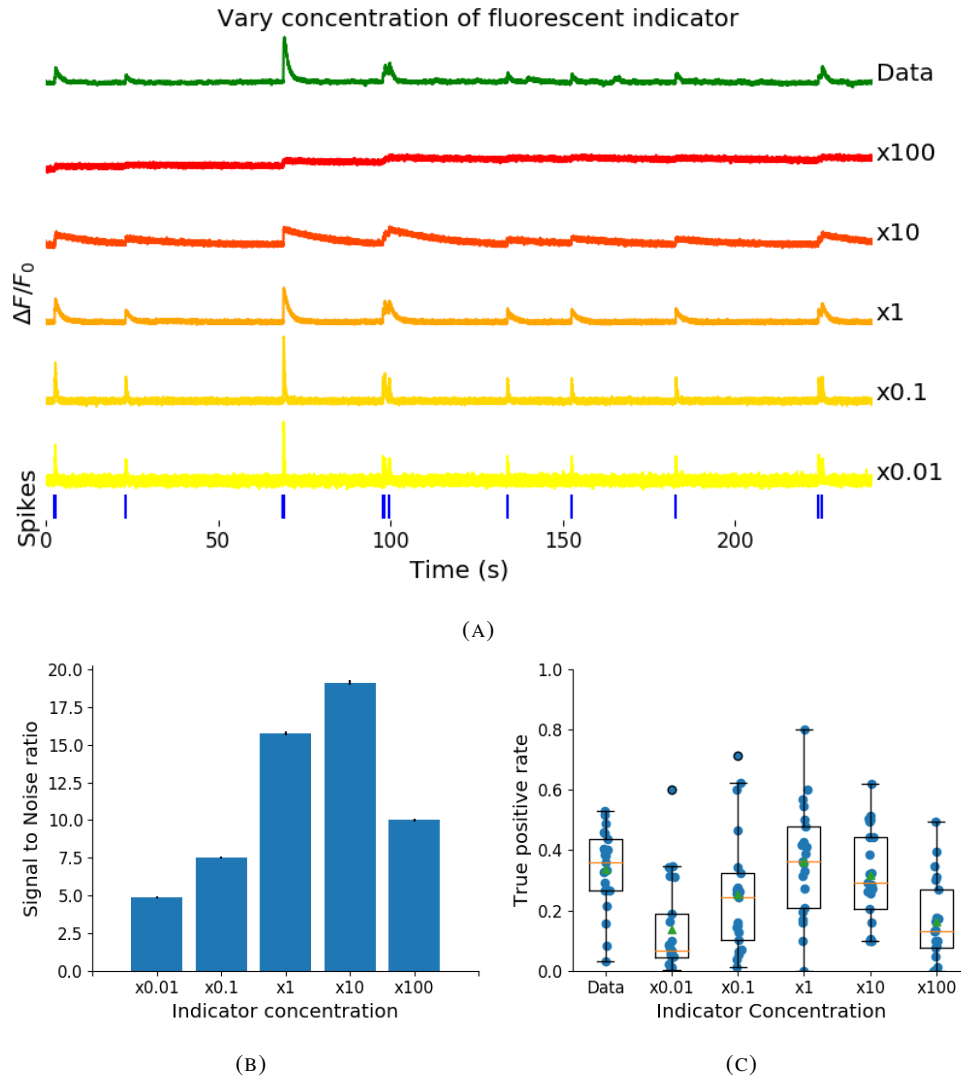


FIGURE 2.5: (A) An example trace for each of the five perturbed values for the concentration of fluorescent calcium indicator. The top two traces are produced by the lower perturbed values, the middle trace is produced by the experimental value, and the lowest two traces are produced when using the higher perturbed values. (B) The signal-to-noise ratio of the modelled fluorescence traces using each of the four perturbed values, and the experimental value. Extreme perturbations of the concentration either above or below the experimental level lowered the SNR. (C) The true-positive rates of the deconvolution algorithm's predictions when inferring from the observed data, and inferring from modelled traces using the perturbed and experimental values. We found that the algorithms performs equally badly on the two most extreme values, and performs equally well on the experimental value, and the next higher perturbed value.

### 2.3. Results

---

1042 GCaMP, due to proximity to the infection site, or the cell becoming ‘nuclear-filled’ (Tian et  
1043 al., 2009; Chen et al., 2013). Also, GCaMP is often used for longitudinal experiments where  
1044 the same cells are re-imaged across multiple days or weeks. However since GCaMP expres-  
1045 sion typically ramps up over time (Chen et al., 2013), the accuracy of spike inference may  
1046 differ across multiple longitudinal recordings in the same cell. We addressed this by varying  
1047 the concentration of calcium indicator in the model, simulating spike trains and measuring  
1048 signal-to-noise ratio and spike inference accuracy on the resulting fluorescence traces. Both  
1049 increasing and decreasing the concentration of the indicator had effects on the fluorescence  
1050 trace, signal-to-noise ratio, and spike inference. The signal-to-noise ratio and spike inference  
1051 quality decreased with decreased indicator concentration, and both showed a decrease when  
1052 the indicator concentration was increased to 100 times its fitted value (figure 2.5). The signal-  
1053 to-noise ratio showed an increase when the indicator concentration was increased to 10 times  
1054 its fitted value, but there was no corresponding change in the spike inference quality. The  
1055 decrease in indicator concentration caused a reduction in the increase in  $\Delta F/F_0$  in response  
1056 to an action potential, and an increase in the decay time of this increase (figure 2.5a). The  
1057 increase in indicator concentration had the opposite effect, it caused an increase in the change  
1058 in  $\Delta F/F_0$  in response to an action potential, and a decrease in the decay time.

1059 Third, the concentration and types of endogenous calcium buffers also vary from neuron  
1060 to neuron, both within and between cell types (Bartol et al., 2015; Maravall et al., 2000;  
1061 Neher and Augustine, 1992). Since the calcium buffer capacity of neurons is high, around  
1062 50-70 (Lee et al., 2000) in excitatory hippocampal pyramidal cells, around 100-250 (Lee et  
1063 al., 2000) in inhibitory hippocampal pyramidal cells, and 900-200 in Purkinje cells (depend-  
1064 ing on the age of the subject), these endogenous buffers compete with GCaMP for binding  
1065 to calcium, and variations in endogenous buffer concentration may affect GCaMP signal and  
1066 therefore spike inference. To address this we varied the concentration of the endogenous  
1067 buffer in the model neuron over five orders of magnitude from 0.8 to 8000  $\mu\text{M}$ , simulated  
1068 calcium fluorescence traces in response to the same set of spike trains, and performed spike  
1069 inference on the resulting fluorescence time series. Increasing the endogenous buffer con-  
1070 centration had a substantial effect on the GCaMP fluorescence signal, both decreasing its  
1071 amplitude and slowing its kinetics (figure 2.6(a)). This corresponded with a decrease in both  
1072 single-spike signal-to-noise ratio (figure 2.6(b)) and spike inference accuracy (figure 2.6(c)).  
1073 In contrast, decreasing endogenous buffer capacity from the fitted value had little effect on  
1074 either the GCaMP signal or spike inference (figure 2.6).

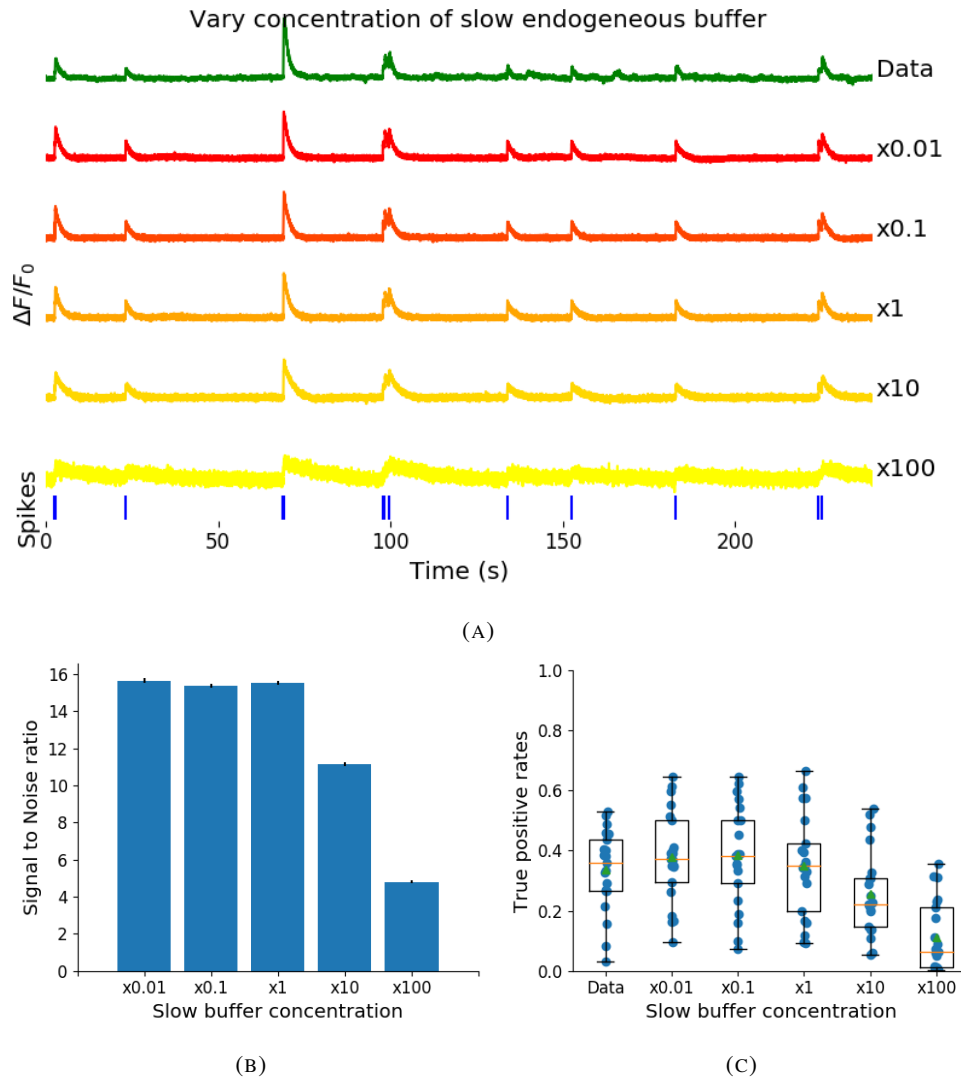


FIGURE 2.6: (A) An example trace for each of the five perturbed values for the concentration of immobile endogenous buffer. (B) The signal-to-noise ratio of the modelled fluorescence traces using each of the four perturbed values, and the experimental value. The lower values for the immobile buffer produce the same SNR as the experimental value. But the higher perturbed values produce fluorescence traces with a lower SNR. (C) The true-positive rates of the deconvolution algorithm's predictions when inferring from the observed data, and inferring from modelled traces using the perturbed and experimental values.

1075 **2.3.5 Single spike inference accuracy drops for high firing rates, but firing rate**  
1076 **itself can be estimated from mean fluorescence amplitude**

1077 The fluorescence signal recorded from neurons using calcium indicators is typically much  
1078 slower than changes in membrane potential for two reasons: first, because the calcium and  
1079 the indicator have slow binding and unbinding kinetics, the signal is a low-pass filtered ver-  
1080 sion of the membrane potential. Second, neuronal two-photon imaging experiments are often  
1081 performed in scanning mode, which limits their frame rate to  $\sim 10\text{Hz}$  or slower. This im-  
1082 plies that multiple spike events that occur close in time might be difficult to resolve from a  
1083 calcium indicator time series. Many cells, especially several types of inhibitory interneurons,  
1084 fire tonically at rates higher than 10Hz. We used the model to test whether spike inference  
1085 accuracy depended on the neuron's firing frequency by driving the cell with spike trains sam-  
1086 pled from a Poisson processes of varying frequency. We simulated a variable firing rate using  
1087 an Ornstein-Uhlenbeck process, and simulated the spike trains using a Poisson distribution  
1088 with its rate taken from this process. Because of the high frequency firing rate of these spike  
1089 trains, we used the accuracy as the measure of spike inference quality. We simulated 30  
1090 spike trains at average firing rate of 1, 5, and 10Hz, and measured the spike inference quality  
1091 of all these traces. Spike inference accuracy decreased with increasing firing rate, for up to  
1092 10Hz Poisson spike trains (figure 2.8(left)). Although the accuracy remained above 90% for  
1093 each of the three frequencies. We also plotted the average  $\Delta F / F_0$  as a function of stimula-  
1094 tion firing rate. We found that it increased monotonically as a function of firing rate (figure  
1095 2.8(right)).

1096 We expected lower spike inference quality as the average spiking frequency increased.  
1097 Since the fluorescence trace, in some sense, is a low pass filtered version of the spike train, a  
1098 tightly packed groups of spikes will be more difficult to infer than isolated spikes. However,  
1099 the increasing amplitude of the fluorescence trace with increasing frequency suggests that  
1100 some spike inference algorithm could be developed based on this amplitude.

1101 **2.4 Discussion**

1102 We designed a biophysical model for the changes in free calcium and bound calcium con-  
1103 centrations within a cell soma with a fluorescent calcium indicator. We used this model to  
1104 model the fluorescence trace resulting from a spike train in this cell. We fit the free parame-  
1105 ters of the model by matching the power spectrum and amplitude of fluorescence traces with  
1106 simultaneously measured spike trains. We inferred spikes from real fluorescence traces and

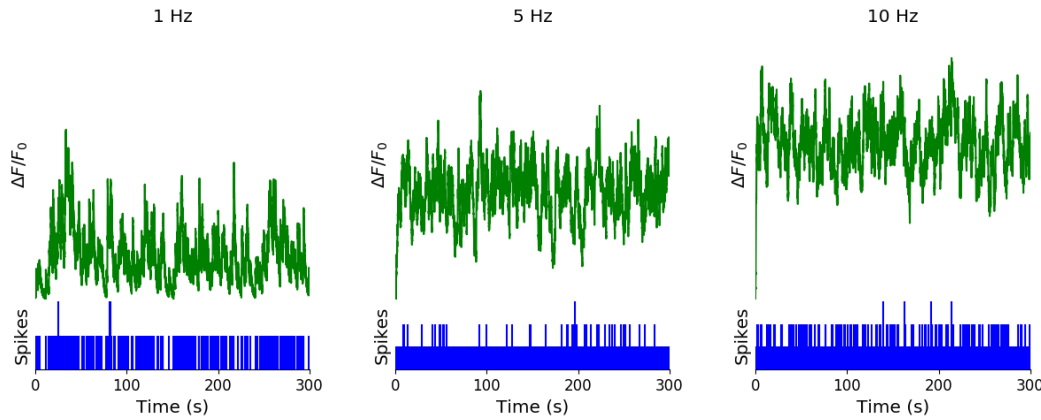


**FIGURE 2.7: Simulating fluorescence traces at different firing rates** Example modelled traces created using simulated spike trains with a mean firing rate of 1Hz (left column), 5Hz (middle column), and 10Hz (right column). Note the difference in amplitude with different mean firing rates.

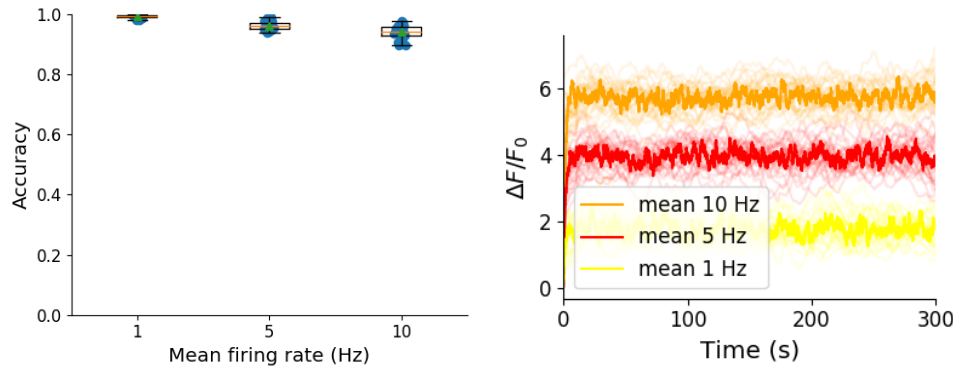


**FIGURE 2.8: Inference quality and  $\Delta F/F_0$  vs Firing rate** (left) The spike inference accuracy when applied to 30 traces created using simulated spike trains with mean firing rates of 1, 5, and 10 Hz. (right) The mean  $\Delta F/F_0$  across those 30 traces for each frequency.

1107 modelled fluorescence traces, and measured the quality of the spike inference in both cases.  
 1108 We found that the spike inference quality was similar in both cases. We perturbed the concen-  
 1109 tration of the calcium buffers in the model, and the binding/unbinding rates of those buffers  
 1110 in the model, and measured the effect on the signal-to-noise ratio (SNR) of the modelled  
 1111 fluorescence traces and the spike inference quality.

1112 For the fluorescent calcium indicator, we found that any large perturbation away from  
 1113 the taken from the literature led to a reduction in SNR, and spike inference quality. For the  
 1114 binding/unbinding rates, we kept the ratio of these rates constant, but altered their values in  
 1115 parallel. The lower values caused a reduction in SNR, and a reduction in spike inference  
 1116 quality. For the endogenous buffer concentration, an increase above the experimental value  
 1117 caused a reduction in SNR and spike inference quality.

## 2.4. Discussion

---

1118     Although the model produced visually similar time series to the real data, there were a  
1119     few aspects it did not capture. First, the real data featured some low-frequency components  
1120     that did not appear related to the spike events. These were not captured by the models we  
1121     used in this study, but could be added in future by adding a suitable low-frequency term to the  
1122     resulting time series. Second, the real data seemed to have some non-linearities not captured  
1123     in the model, for example the response to two nearby spikes was greater than expected from  
1124     the linear sum of two single spikes. This may be due to the co-operative binding of calmod-  
1125     ulin to calcium, which gives calmodulin a supra-linear sensitivity to calcium concentration  
1126     (Faas et al., 2011). The non-linear dynamics of this binding have been included in a recently  
1127     developed spike inference model (Greenberg et al., 2018). Our model, in contrast, behaved  
1128     much more linearly but could be extended in future to include such non-linearities. Third,  
1129     in the real data the fluorescence peak amplitude seemed to vary from spike to spike, even  
1130     for well-isolated spike events. Recent research has shown that calcium influx due to a single  
1131     action potential was quite variable in pyramidal cells, and that this variability had a effect on  
1132     spike inference (Éltes et al., 2019). However in our model we assumed each spike lead to the  
1133     same fixed-amplitude injection of calcium to the cell, leading to much greater regularity in  
1134     fluorescence peak amplitudes. This variability could be added in future versions of the model  
1135     by making the injected calcium peak a random variable. Fourth, we modelled the soma as  
1136     a single compartment, but in reality there is likely a non-uniform spatial profile of calcium  
1137     concentration. This may matter because some endogenous buffers might access calcium right  
1138     as it influxes from the extracellular space, whereas the majority of the fluorescence signal is  
1139     more likely coming from the bulk of the cytoplasm. Future models could attempt to model  
1140     these spatial dependencies to assess whether they affect the overall spike inference procedure.

1141     As well as the optimised parameters, the model has 14 fixed parameters than can be  
1142     changed to simulate different types of calcium indicators. This model could be used to test  
1143     the theoretical performance of proposed new types of calcium indicator. The model could  
1144     also be used by developers of spike inference algorithms to test the effects of changing cal-  
1145     cium indicator parameters on spike inference, or to test the affects of changing spiking char-  
1146     acteristics on spike inference. For example, high firing rate vs low firing rate, or bursting vs  
1147     no bursting. Given the increasing amplitude of the fluorescence trace with increasing mean  
1148     firing rate, it would be possible to build a spike inference algorithm on this principle at least  
1149     in part.

1150     Our model has already been used as a tool by our colleagues, for simulating fluorescence  
1151     traces in response to cells that can fire with a continuous rate between 10 and 20Hz, but do

1152 not always do so. Our colleagues found that a combination of the amplitude and the variance  
1153 of the simulated fluorescence trace was the best indicator of firing rate. For example, when  
1154 a cell was not firing, the amplitude and variance of the fluorescence trace was relatively low.  
1155 When the cell fired with a low firing rate  $\sim 1\text{Hz}$ , the mean amplitude was still low but  
1156 the variance of the fluorescence trace was high, and for high firing rate  $\sim 10 - 20\text{Hz}$ , the  
1157 fluorescence amplitude was high, and the variance was low. In this way, our model may be  
1158 useful for investigating firing rates underlying real fluorescence traces in response to cells  
1159 which can fire in these rage ranges.

1160 A recent paper by Greenberg et al (2018) described a biophysical model for spike train  
1161 inference called the ‘Sequential binding model’. Their model for spike inference was sim-  
1162 ilar to our model for fluorescence traces in that their model included parameters for two  
1163 types of endogenous buffer. But this model also included dynamics for calcium binding to  
1164 and unbinding from these endogenous buffers. Furthermore, this model included dynamics  
1165 for calcium binding to and unbinding from the four binding sites present on a GCaMPs6  
1166 molecule. In the accuracy measurements specified in that paper, this model performed better  
1167 than the MLspike algorithm, which is also partially a biophysically model, and it performed  
1168 better than the constrained non-negative deconvolution algorithm. The sequential binding  
1169 model also has biophysically interpretable parameters, and its fitted parameters for quantities  
1170 such as buffering capacity and calcium influx upon action potential firing fall in line with  
1171 experimental values (Greenberg et al., 2018). Biophysical models like this appear to be the  
1172 way forward for spike inference algorithms, and would make a good complimentary tool to  
1173 our fluorescence model.

1174 **Chapter 3**

1175 **Functional networks expand across  
1176 anatomical boundaries as correlation  
1177 time-scale increases**

1178 *Abstract*

1179 Decades of research has established that correlated spiking plays a crucial role in represent-  
1180 ing sensory information. One drawback associated with the recent improvement in recording  
1181 technology and consequent large datasets is the difficulty in analysing higher order correla-  
1182 tions in large neuronal ensembles. One benefit of these datasets that has not yet been explored  
1183 is the opportunity to compare correlations within anatomical regions to correlations across  
1184 anatomical regions. In this work, we measured correlations between neurons residing in  
1185 nine different brains regions in three awake and behaving mice. Using the these correlation  
1186 measurements, we created weighted undirected graph networks and applied network science  
1187 methods to detect functional communities in our neural ensembles. We compared these func-  
1188 tional communities to their anatomical distribution. We repeated the analysis, using different  
1189 timescales for our correlation measurements, and found that functional communities were  
1190 more likely to be dominated by neurons from a single brain region at shorter timescales  
1191 (< 100ms).

### 1192 3.1 Introduction

1193 Decades of research has established that correlations play a crucial role in representing sen-  
1194 sory information. For example, the onset of visual attention has been shown to have a greater  
1195 affect on the correlations in the macaque V4 region than on the firing rates in that region  
1196 (Cohen and Maunsell, 2009). Recent findings show that spontaneous behaviours explain cor-  
1197 relations in parts of the brain not associated with motor control (Stringer et al., 2019), that  
1198 satiety state appears to have a brain wide representation (Allen et al., 2019), and that subject  
1199 exploratory and non-exploratory states are represented in the amygdala (Gründemann et al.,  
1200 2019). So, behavioural states are likely represented across many regions of the brain, not just  
1201 motor related areas. In order to understand the brain, we must understand the interactions  
1202 between neurons and regions.

1203 Because of limitations in recording technology almost all research has explored corre-  
1204 lations between neurons within a given brain region, or within only two regions at most  
1205 (Wierzynski et al., 2009; Patterson et al., 2014; Girard, Hupé, and Bullier, 2001). Rela-  
1206 tively little is known about correlations between neurons in many different brain regions.  
1207 However, the recent development of ‘Neuropixels’ probes (Jun et al., 2017) has allowed  
1208 extracellular voltage measurements to be collected from multiple brain regions simultane-  
1209 ously routinely, and in much larger numbers than traditional methods. In this project we  
1210 used a publicly-available Neuropixels dataset to analyse correlations between different brain  
1211 regions (Stringer et al., 2019).

1212 A drawback associated with the improvement in recording technology is an increase in  
1213 the difficulty in analysing these data. For example, analysing the  $i$ th order interactions of  
1214  $N$  neurons generally requires estimation of  $N^i$  parameters. A number that becomes astro-  
1215 nomical for large  $N$ . New methods are required for analysing these new large datasets. We  
1216 attempted to address this requirement in this piece of research by applying a cutting-edge  
1217 network science community detection method to neural data.

1218 Another unexplored area of research is the changes in cell interactions at different timescales.  
1219 Studies have shown different timescales for fluctuations in spiking activity (Murray et al.,  
1220 2014), and different time scales for event representation (Baldassano et al., 2017) across dif-  
1221 ferent brain regions. Still most studies focus on quantifying interactions at a given timescale.  
1222 But neurons may interact differently, or may interact with different neurons at different  
1223 timescales. Here we explore correlated communities of neurons at different timescales.

1224 In this work, we measured correlations between binned spike counts from neurons from

### 3.2. Data

---

1225 nine different regions of the mouse brain. These measurements induced a weighted undi-  
1226 rected graph or network where each neuron is represented by a node, and the strength of  
1227 the connection between these nodes/neurons is the strength of the correlation between their  
1228 spike counts. We then applied newly invented network methods (Humphries et al., 2019)  
1229 to this network to find any community structure, and place the neurons in these correlation  
1230 based communities. Finally, we compared these functional communities to the anatomical  
1231 membership of the neurons.

1232 To investigate the functional communities and their relationship with anatomy at different  
1233 time scales, we repeated these analyses using different length bin widths when binning spike  
1234 times.

1235 To find and analyse functional networks while controlling for the subject’s behaviour, we  
1236 conditioned the binned spike counts on data from a video of the subject’s face, and repeated  
1237 our analysis for spike count correlations (or noise correlations) and signal correlations.

## 1238 3.2 Data

1239 The data that we used in this project were collected by Nick Steinmetz and his lab members  
1240 (Stringer et al., 2019; Steinmetz et al., 2019).

### 1241 3.2.1 Brain regions

1242 Neuropixels probes were used to collect extracellular recordings (Jun et al., 2017) from three  
1243 different mice. The mice were awake, headfixed, and engaging in spontaneous behaviour.  
1244 The mice were of different sexes and different ages. One mouse was ‘wild-type’, the others  
1245 were mutants. Details as follows:

- 1246 1. male, wild type, P73.
- 1247 2. female, TetO-GCaMP6s, Camk2a-tTa, P113
- 1248 3. male, Ai32, Pvalb-Cre, P99

1249 Eight probes were used to collect readings from 2296, 2668, and 1462 cells respectively.  
1250 Data were collected from nine brain regions in each mouse:

- 1251 • Caudate Putamen (CP)
- 1252 • Frontal Motor Cortex (Frmocxt)
- 1253 • Hippocampal formation (Hpf)

- 1254     ● Lateral Septum (Ls)
  - 1255     ● Midbrain (Mb)
  - 1256     ● Superior Colliculus (Sc)
  - 1257     ● Somatomotor cortex (Sommotcx)
  - 1258     ● Thalamus (Th)
  - 1259     ● Primary visual cortex (V1)
- 1260   Readings were continuous and lasted for about 1 hour (Stringer et al., 2019; Steinmetz et al.,  
1261 2019). Locations of each of the probes can be seen in figure 3.1.

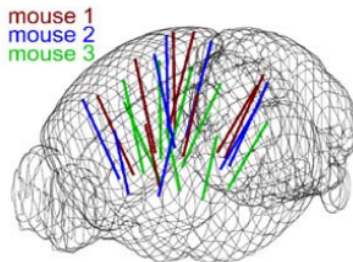


FIGURE 3.1: **Probe Locations:** The locations of the probes in each of the three mouse brains (Stringer et al., 2019).

### 1262 3.2.2 Video recordings

1263 Video recordings of the mouse's face were taken during the spontaneous behaviour. We  
1264 had access to the top 500 principle components and top 500 eigenvectors of the processed  
1265 videos. The frequency of recording was slightly less than 40Hz. Each frame contained  
1266  $327 \times 561$  pixels (Stringer et al., 2019; Steinmetz, Carandini, and Harris, 2019). These  
1267 principal components were used as behavioural data. We controlled for these components  
1268 when taking measurements conditioned on behaviour.

## 1269 3.3 Methods

### 1270 3.3.1 Binning data

1271 We transformed the spike timing data into binned spike count data by dividing the experi-  
1272 mental period into time bins and counting the spikes fired by each cell within the time period  
1273 covered by each of those bins. The data were divided into time bins of various widths ranging  
1274 from 0.005s to 4s.

### 3.3. Methods

---

If the total length of the recording period was not an integer multiple of the time bin width, we cut off the remaining time at the end of the recording period. This period was at most 3.99s. This is far less than the total recording time of around 1 hour. So, this detail would not affect our results.

#### 3.3.2 Correlation coefficients

We calculated Pearson's correlation coefficient for pairs of spike counts from pairs of neurons. For jointly distributed random variables  $X$  and  $Y$ , Pearson's correlation coefficient is defined as:

$$\rho_{XY} = \frac{\text{cov}(X, Y)}{\sigma_X \sigma_Y} \quad (3.1)$$

$$= \frac{E[(X - \mu_X)(Y - \mu_Y)]}{\sigma_X \sigma_Y} \quad (3.2)$$

where  $E$  denotes the expected value,  $\mu$  denotes the mean, and  $\sigma$  denotes the standard deviation. The correlation coefficient is a normalised measure of the covariance. It can take values between 1 (completely correlated) and  $-1$  (completely anti-correlated). Two independent variables will have a correlation coefficient of 0. But, having 0 correlation does not imply independence.

If we do not know the means and standard deviations required for equation 3.1, but we have samples from  $X$  and  $Y$ , Pearson's sample correlation coefficient is defined as:

$$r_{XY} = \frac{\sum_{i=1}^n (x_i - \bar{x})(y_i - \bar{y})}{\sqrt{\sum_{i=1}^n (x_i - \bar{x})^2} \sqrt{\sum_{i=1}^n (y_i - \bar{y})^2}} \quad (3.3)$$

where  $\{(x_i, y_i)\}$  for  $i \in \{1, \dots, n\}$  are the paired samples from  $X$  and  $Y$ , and  $\bar{x} = \frac{1}{n} \sum_{i=1}^n x_i$ , and  $\bar{y} = \frac{1}{n} \sum_{i=1}^n y_i$  are the sample means.

In practice we used the python function `scipy.stats.pearsonr` to calculate the correlation coefficients.

#### 1289 Total correlations, $r_{SC}$

In this context, we defined the total correlation ( $r_{SC}$ ) of two cells to be the correlation between the spike counts of those cells across the entire period of spontaneous behaviour.

1292 **Shuffled total correlations**

1293 We measured the shuffled total correlations between two neurons by randomly permuting one  
 1294 of the neuron's spike counts and measuring the total correlations. These shuffled correlations  
 1295 were useful when measuring the effect of time bin width on correlations, and when decid-  
 1296 ing which correlations should be preserved when creating correlation networks (see section  
 1297 3.3.5).

1298 **Separating Correlations & Anti-correlations**

1299 In order to compare the effect of bin width on measures of negative  $r_{SC}$  (anti-correlation) and  
 1300 positive  $r_{SC}$  separately, we had to separate correlated and anti-correlated pairs. To do this, we  
 1301 simply measured the mean  $r_{SC}$ , taking the mean across all the bin widths. If this quantity was  
 1302 positive or zero we regarded the pair as positively correlated. If this quantity was negative  
 1303 we regarded the pair as anti-correlated.

1304 **3.3.3 Conditioning on behavioural data**

Our behavioural data consisted of the top 500 principal components (PCs) of a processed video recording of the mouse's face (see section 3.2.2). Denoting the spike count of a given cell by  $X$ , and the PCs by  $Z_1, \dots, Z_{500}$ , we wanted to model  $X$  as a function of  $Z_1, \dots, Z_{500}$  in order to estimate

$$E[X|Z_1, \dots, Z_{500}] = \int_{x \in X} x P(X = x|Z_1, \dots, Z_{500}) dx \quad (3.4)$$

$$= \int_{x \in X} x \frac{P(X = x, Z_1, \dots, Z_{500})}{P(Z_1, \dots, Z_{500})} dx \quad (3.5)$$

1305 Given the 500 components, a naïve estimation of  $P(Z_1, \dots, Z_{500})$  or  $P(X, Z_1, \dots, Z_{500})$  by  
 1306 histogramming was impossible. Therefore we modelled  $X$  as a linear combination of the  
 1307 PCs.

1308 **Linear regression**

1309 We modelled the spike count of a given cell,  $X$ , as a linear combination of the PCs of the  
 1310 video of the mouse's face,  $\mathbf{Z} = Z_1, \dots, Z_{500}$ . We tried three different types of regularization

1311 • L1 or 'Lasso'

1312 • L2 or 'Ridge regression'

### 3.3. Methods

---

- 1313     • ‘Elastic net’ regularisation (a linear combination of both  $L1$  and  $L2$  regularisation  
1314       penalties)

1315     The elastic net regularisation performed the best, so we stuck with that.

#### 1316     **Elastic net regularisation**

Suppose we wish to model  $n$  observations of a random variable  $X$ ,  $\mathbf{x} = (x_1, \dots, x_n)$  using  $n$  instances of  $m$  predictors  $\mathbf{Z} = (Z_1, \dots, Z_m)$ . The naïve elastic net criterion is

$$L(\lambda_1, \lambda_2, \boldsymbol{\beta}) = |\mathbf{x} - \mathbf{Z}\boldsymbol{\beta}|^2 + \lambda_2|\boldsymbol{\beta}|_2 + \lambda_1|\boldsymbol{\beta}|_1 \quad (3.6)$$

where

$$|\boldsymbol{\beta}|_2 = \sum_{j=1}^m \beta_j^2 \quad (3.7)$$

$$|\boldsymbol{\beta}|_1 = \sum_{j=1}^m |\beta_j| \quad (3.8)$$

The naïve elastic net estimator  $\hat{\boldsymbol{\beta}}$  is the minimiser of the system of equations 3.6 (Zou and Hastie, 2005)

$$\hat{\boldsymbol{\beta}} = \arg \min_{\boldsymbol{\beta}} L(\lambda_1, \lambda_2, \boldsymbol{\beta}) \quad (3.9)$$

1317     We implemented the model using the `ElasticNetCV` method of Python’s  
1318       `sklearn.linear_models` package.

1319       As well as using the PCs, we also tried fitting the models using the raw video data recon-  
1320       structed from the PCs and eigenvectors. These models performed worse than those using the  
1321       PCs. We expected this because each representation contains the same amount of information,  
1322       but the raw video representation spreads this information across many more components.  
1323       This requires more parameter fitting, but given the same information.

#### 1324     **Conditional covariance**

We calculated the expected value of the conditional covariance using the law of total covariance.

$$\text{cov}(X, Y) = E[\text{cov}(X, Y|Z)] + \text{cov}(E[X|Z], E[Y|Z]) \quad (3.10)$$

1325 where these expected values are calculated with respect to the distribution of  $Z$  as a random  
 1326 variable.

1327 The law of total covariance breaks the covariance into two components. The first com-  
 1328 ponent  $E[\text{cov}(X, Y|Z)]$  is the expected value, under the distribution of  $Z$ , of the conditional  
 1329 covariance  $\text{cov}(X, Y|Z)$ . This covariance could be interpreted as the unnormalised version  
 1330 of what Cohen et al. (2011) call the spike count correlation (Cohen and Kohn, 2011), aka.  
 1331 the noise correlation. In particular, this is the covariance of the spike counts in response to  
 1332 repeated presentation of identical stimuli.

1333 The second component is analogous to what Cohn et al. (2011) call the *signal correlation*  
 1334 (Cohen and Kohn, 2011). In particular,  $\text{cov}(E[X|Z], E[Y|Z])$  is the covariance between  
 1335 spike counts in response to different stimuli.

Using our linear model, we calculated  $E[X|Z_1, \dots, Z_{500}]$  for each cell  $X$ . Then we pro-  
 ceeded to calculate

$$E[\text{cov}(X, Y|Z_1, \dots, Z_{500})] = \text{cov}(X, Y) - \quad (3.11)$$

$$\text{cov}(E[X|Z_1, \dots, Z_{500}], E[Y|Z_1, \dots, Z_{500}]) \quad (3.12)$$

1336 **Measures of conditional correlation**

As a measure of expected correlation, we measured the ‘event conditional correlation’ (Maugis,  
 2014)

$$\rho_{XY|Z} = \frac{E[\text{cov}(X, Y|Z)]}{\sqrt{E[\text{var}(X|Z)]E[\text{var}(Y|Z)]}} \quad (3.13)$$

1337 Although this is not an actual correlation, it is an intuitive analogue to the correlation as a  
 1338 normalised version of the covariance.

For comparison, we also measured the ‘signal correlation’

$$\rho_{\text{signal}} = \frac{\text{cov}(E[X|Z], E[Y|Z])}{\sqrt{\text{var}(E[X|Z])\text{var}(E[Y|Z])}} \quad (3.14)$$

1339 this is an actual correlation.

1340 **3.3.4 Information Theory**

1341 **Entropy  $H(X)$**

The entropy of a random variable  $X$ , with outcomes  $x_1, \dots, x_N$ , and corresponding probabilities  $p_1, \dots, p_N$  is defined as

$$H(X) = - \sum_{n=1}^N p_n \log_2 p_n \quad (3.15)$$

1342 This quantity is also known as the information entropy or the ‘surprise’. It measures the  
 1343 amount of uncertainty in a random variable. For example, a variable with a probability of 1  
 1344 for one outcome, and 0 for all other outcomes will have 0 bits entropy, because it contains no  
 1345 uncertainty. But a variable with a uniform distribution will have maximal entropy as it is the  
 1346 least predictable. This quantity is analogous to the entropy of a physical system (Shannon,  
 1347 1948). Note that any base may be used for the logarithm in equation 3.15, but using base 2  
 1348 means that the quantity will be measured in ‘bits’.

The joint entropy of two jointly distributed random variables  $X$  and  $Y$ , where  $Y$  has outcomes  $y_1, \dots, y_M$ , is defined as

$$H(X, Y) = - \sum_{n=1}^N \sum_{m=1}^M P(X = x_n, Y = y_m) \log_2 P(X = x_n, Y = y_m) \quad (3.16)$$

1349 If  $X$  and  $Y$  are independent then  $H(X, Y) = H(X) + H(Y)$ . Otherwise  $H(X, Y) <$   
 1350  $H(X) + H(Y)$ . When  $X$  and  $Y$  are completely dependent  $H(X, Y) = H(X) = H(Y)$ .

The conditional entropy of  $Y$  conditioned on  $X$  is defined as

$$H(Y|X) = - \sum_{n=1}^N \sum_{m=1}^M P(X = x_n, Y = y_m) \log_2 \frac{P(X = x_n, Y = y_m)}{P(X = x_n)} \quad (3.17)$$

1351 When  $X$  and  $Y$  are independent  $H(Y|X) = H(Y)$ . Intuitively, we learn nothing of  $Y$  by  
 1352 knowing  $X$ , so  $Y$  is equally uncertain whether we know  $X$  or not. If  $Y$  is totally dependent  
 1353 on  $X$ , then the fraction in the logarithm is 1, which gives  $H(Y|X) = 0$ .

1354 These entropy measures are the basis of the mutual information measure.

1355 **Maximum entropy limit**

When spiking data is binned into spike counts there is an upper limit on the entropy of these data. The maximum entropy discrete distribution is the discrete uniform distribution. A

random variable with this distribution will take values from some finite set with equal probabilities. Binned spike count data will take values between 0 and some maximum observed spike count  $n_{\max}$ . A neuron with responses that maximises entropy will take these values with equal probability, i.e. if  $i \in \{0, \dots, n_{\max}\}$  then  $P(X = i) = \frac{1}{n_{\max} + 1}$ . The entropy of this neuron will be

$$\begin{aligned} H(X) &= - \sum_{i=0}^{n_{\max}} P(X = i) \log_2 P(X = i) \\ &= - \sum_{i=0}^{n_{\max}} \frac{1}{n_{\max} + 1} \log_2 \left( \frac{1}{n_{\max} + 1} \right) \\ &= - \log_2 \left( \frac{1}{n_{\max} + 1} \right) \\ &= \log_2 (n_{\max} + 1) \end{aligned}$$

1356 Therefore, the maximum entropy of the binned spike counts of a neuron is  $\log_2 (n_{\max} + 1)$ .  
 1357 Of course, it would be very unusual for a neuron to fire in accordance with the discrete  
 1358 uniform distribution. Most measurements of entropy taken on binned spiking data will be  
 1359 much lower than the maximum. See figure 3.2 to see the maximum entropy as a function of  
 1360 the maximum observed spike count.

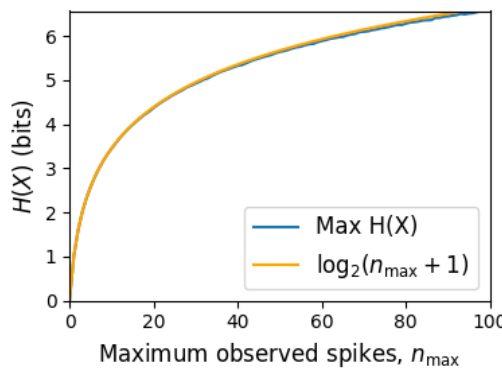


FIGURE 3.2: **Entropy Limit:** The upper limit on entropy of binned spike count data as a function of the maximum observed spike count. The orange line is the analytical maximum. The blue line is the entropy of samples with  $N = 1000$  data points taken from the discrete uniform distribution.

1361 **Mutual Information**  $I(X; Y)$

1362 The mutual information can be defined mathematically in a number of ways, all of which are  
 1363 equivalent. These definitions illustrate the different ways of interpreting the mutual informa-  
 1364 tion.

### 3.3. Methods

---

For two jointly distributed random variables  $X$  and  $Y$ , the mutual information  $I(X;Y)$  is defined as

$$I(X;Y) = H(Y) - H(Y|X) \quad (3.18)$$

$$= H(X) - H(X|Y) \quad (3.19)$$

1365 Equation 3.18 fits with the following intuition: The mutual information between  $X$  and  $Y$  is  
1366 the reduction in uncertainty about  $X$  gained by knowing  $Y$ , or vice versa. We could also say  
1367 the mutual information is the amount of information gained about  $X$  by knowing  $Y$ , or vice  
1368 versa.

Another useful entropy based definition for the mutual information is

$$I(X;Y) = H(X) + H(Y) - H(X,Y) \quad (3.20)$$

1369 This definition is useful because it does not require the calculation of conditional probabili-  
1370 ties.

The mutual information can also be defined in terms of marginal, joint, and conditional distributions. For example,

$$I(X;Y) = - \sum_{n=1}^N \sum_{m=1}^M P(X = x_n, Y = y_m) \log_2 \frac{P(X = x_n, Y = y_m)}{P(X = x_n)P(Y = y_m)} \quad (3.21)$$

Notice that this can be rewritten as a Kullback–Leibler divergence.

$$I(X;Y) = D_{KL}(P(X,Y) || P(X)P(Y)) \quad (3.22)$$

1371 So, we can also think of the mutual information as a measure of the difference between  
1372 the joint distribution of  $X$  and  $Y$ , and the product of their marginal distributions. Since the  
1373 product of the marginal distributions is the joint distribution for independent variables, we  
1374 can think of the mutual information as a measure of the variables’ dependence on one another.

1375 The minimum value that  $I(X;Y)$  can take is 0. This occurs when the random variables  
1376  $X$  and  $Y$  are independent. Then we have  $H(X|Y) = H(X)$ , and  $H(Y|X) = H(Y)$ , which  
1377 according to equation 3.18, gives  $I(X;Y) = 0$ . We also have that  $H(X,Y) = H(X) +$   
1378  $H(Y)$  in this case, which according equation 3.20, gives  $I(X;Y) = 0$ . Finally, we also have  
1379  $P(X,Y) = P(X)P(Y)$ , which leaves us with 1 in the argument for the logarithm in equation  
1380 3.21, which again gives  $I(X;Y) = 0$ .

1381 The mutual information reaches its maximum value when one of the variables  $X$  and  
1382  $Y$  is completely determined by knowing the value of the other. In that case  $I(X; Y) =$   
1383  $\min\{H(X), H(Y)\}$ .

1384 **Variation of Information**  $VI(X, Y)$

The variation of information is another information theoretical quantity based on the mutual information. It is defined as

$$VI(X; Y) = H(X) + H(Y) - 2I(X; Y) \quad (3.23)$$

We can rewrite this as the summation of two positive quantities

$$VI(X; Y) = [H(X) - I(X; Y)] + [H(Y) - I(X; Y)] \quad (3.24)$$

1385 In English, the variation of information is the summation of the uncertainty in the random  
1386 variables  $X$  and  $Y$  excluding the uncertainty shared by those variables.

1387 This measure will become more relevant when we go on to talk about clusterings because  
1388  $VI(X; Y)$  forms a metric on the space of clusterings.

1389 **Measuring entropies & mutual information**

1390 In practice, we measured the mutual information between spike counts using Python and the  
1391 python package `pyitlib`. We used the PT-bias correction technique to estimate the bias of  
1392 our measurements when measuring the mutual information between the spike counts of two  
1393 cells (Treves and Panzeri, 1995).

1394 When measuring the mutual information between clusterings we used Python, but we  
1395 used the `mutual_info_score`, `adjusted_mutual_info_score`, and  
1396 `normalized_mutual_info_score` functions from the `sklearn.metrics` part of  
1397 the `sklearn` package.

1398 **3.3.5 Network analysis**

1399 **Correlation networks**

1400 In order to analyse functional networks created by the neurons in our ensemble, we mea-  
1401 sured the total correlation between each pair of neurons. These measurements induced an

### 3.3. Methods

---

1402 undirected weighted graph/network between the neurons. The weight of each connection  
1403 was equal to the total correlation between each pair of neurons.

1404 We followed the same procedure for total correlations 3.3.2, spike count correlations, and  
1405 signal correlations 3.3.3.

#### 1406 **Rectified correlations**

1407 At the time of writing, the community detection method outlined in (Humphries et al., 2019)  
1408 could only be applied to networks with positively weighted connections. But many neuron  
1409 pairs were negatively correlated. To apply the community detection method, we *rectified* the  
1410 network, by setting all the negative weights to zero.

1411 We also looked for structure in the network created by negative correlations by reversing  
1412 the signs of the correlations, and rectifying these correlations before applying our network  
1413 analysis.

1414 Finally, we used the absolute value of the correlations as the weights for the graph/network.  
1415 By doing this, we hoped to identify both correlated and anti-correlated functional communi-  
1416 ties of neurons.

#### 1417 **Sparsifying data networks**

1418 When creating our correlation networks, we wanted to exclude any correlations that could  
1419 be judged to exist ‘by chance’. To do this, we measured the 5th and 95th percentile of  
1420 the shuffled correlations (see section 3.3.2) for the given mouse and time bin width. We  
1421 then set all the data correlations between these two values to 0. This excluded any ‘chance’  
1422 correlations from our network, and created a sparser network. This allowed us to make use  
1423 of the ‘sparse weighted configuration model’ as described in section 3.3.5.

#### 1424 **Communities**

1425 Given some network represented by an adjacency matrix  $\mathbf{A}$ , a community within that net-  
1426 work is defined as a collection of nodes where the number of connections within these nodes  
1427 is higher than the expected number of connections between these nodes. In order to quan-  
1428 tify the ‘expected’ number of connections, we need a model of expected networks. This is  
1429 analogous to a ‘null model’ in traditional hypothesis testing. We test the hypothesis that our  
1430 data network departs from the null network model to a statistically significant degree. For  
1431 undirected unweighted networks, the canonical model of a null network is the configuration

1432 model (Fosdick et al., 2016). Since we are working with weighted sparse networks, we used  
1433 more suitable null models, described below.

1434 **Weighted configuration model**

1435 The *weighted configuration model* is a canonical null network model for weighted networks.  
1436 Given some data network, the weighted configuration model null network will preserve the  
1437 degree sequence and weight sequence of each node in the data network. But the edges will  
1438 be distributed randomly (Fosdick et al., 2016). Any structure in the data network beyond  
1439 its degree sequence and weight sequence will not be captured in the weighted configuration  
1440 model. So, this model can be used in testing the hypothesis that this extra structure exists.

1441 **Sparse weighted configuration model**

1442 The *sparse weighted configuration model* is another null network model. Similar in nature to  
1443 the weighted configuration model (see section 3.3.5), but the sparsity of the data network is  
1444 preserved in the null network. This is achieved by sampling from a probability distribution  
1445 for the creation or non-creation of each possible connection, then distributing the weight of  
1446 the data network randomly in this sparse network (Humphries et al., 2019). This is the null  
1447 network that we used when searching for additional structure in our data networks.

1448 **Spectral rejection**

1449 We made use of the spectral rejection algorithm as outlined in (Humphries et al., 2019). The  
1450 spectral rejection algorithm is a method for finding structure in a network not captured by a  
1451 supposed null model, if such structure exists.

To describe the method, we denote our data network matrix  $\mathbf{W}$ , we denote the expected network of our null network model as  $\langle \mathbf{P} \rangle$ . Then the departure of our data network from the null network can be described by the matrix

$$\mathbf{B} = \mathbf{W} - \langle \mathbf{P} \rangle \quad (3.25)$$

1452 a common choice for  $\langle \mathbf{P} \rangle$  in community detection is the ‘configuration model’ (Fosdick et  
1453 al., 2016; Humphries, 2011). The matrix  $\mathbf{B}$  is often called the configuration matrix, in this  
1454 context we will use the term ‘deviation matrix’ as it captures the deviation of  $\mathbf{W}$  from the  
1455 null model.

### 3.3. Methods

---

1456 To test for structure in the network represented by  $\mathbf{W}$ , we examine the eigenspectrum of  $\mathbf{B}$   
1457 and compare it to the eigenspectrum of our null model. Firstly, note that since our data model  
1458 doesn't allow self loops, and is not directed, the matrix representing the network will be  
1459 symmetric and positive semi-definite, and will therefore be invertible with real eigenvalues.  
1460 We selected a null model with the same characteristics.

1461 To find the eigenspectrum of the null model, we generated  $N$  samples from our null  
1462 model  $P_1, \dots, P_N$ , and we measured their deviation matrices  $B_1, \dots, B_N$ . We then calculated  
1463 the eigenspectrum of each of those samples. We calculated the upper bound of the null model  
1464 eigenspectrum by taking the mean of the largest eigenvalues of  $B_1, \dots, B_N$ . We calculated a  
1465 lower bound on the null model eigenspectrum by taking the mean of the smallest eigenvalues  
1466 of  $B_1, \dots, B_N$ .

1467 We then calculated the eigenspectrum of  $\mathbf{B}$ , our data network deviation matrix. If any of  
1468 those eigenvalues lay outside of the upper or lower bounds of the null model eigenspectrum,  
1469 this is evidence of additional structure not captured by the null model. If we chose the sparse  
1470 weighted configuration model (see section 3.3.5) as our null network model, then eigenvalues  
1471 lying below the lower bound indicate  $k$ -partite structure in the network. For example, if one  
1472 eigenvalue lay below the lower bound, this would indicate some bipartite structure in the data  
1473 network. If any eigenvalues lay above the upper bound of the null model eigenspectrum, this  
1474 is evidence of community structure in the data network. For example, one eigenvalue of  $\mathbf{B}$   
1475 lying above the upper bound of the null model eigenspectrum indicates the presence of two  
1476 communities in the network (Humphries, 2011).

#### 1477 Node rejection

1478 If there are  $d$  data eigenvalues lying outside of the null network eigenspectrum, the  $d$  eigen-  
1479 vectors corresponding to these eigenvalues will form a vector space. If we project the nodes  
1480 of our network into this vector space, by projecting either rows or columns of the data ma-  
1481 trix, we can see how strongly each node contributes to the vector space. Nodes that contribute  
1482 strongly to the additional structure will project far away from the origin, nodes that do not  
1483 contribute to the additional structure will project close to the origin. We want to use this  
1484 information to discard those nodes that do not contribute.

1485 We can test whether a node projects *far* away from the origin or *close* to the origin  
1486 using the eigenvalues and eigenvectors of  $B_1, \dots, B_N$ . The  $j$ th eigenvector and eigenvalue  
1487 of  $B_i$  gives a value for a null network's projection into the  $j$ th dimension of the additional  
1488 structure vector space. The matrices  $B_1, \dots, B_N$  give  $N$  projections into that dimension.

1489 These projections are a distribution of the null networks' projections. If the data node's  
 1490 projection exceeds that of the null network projections this node is judged to project *far* from  
 1491 the origin, and therefore contribute to the additional structure. Otherwise, the node is judged  
 1492 to project *close* to the origin, and is therefore rejected (Humphries et al., 2019).

1493 **Community detection**

1494 Another application for this  $d$  dimensional space is community detection. We first project  
 1495 all of the nodes into this  $d$ -dimensional space, then perform the clustering in this space. The  
 1496 clustering and community detection procedure is described in (Humphries, 2011).

1497 In practice, the procedure is carried out  $n$  times (we chose  $n = 100$  times), this returns  $n$   
 1498 clusterings. We resolve these  $n$  clusterings to one final clustering using *consensus clustering*.  
 1499 We used the consensus clustering method that uses an explicit null model for the consensus  
 1500 matrix, as outlined in (Humphries et al., 2019).

1501 **3.3.6 Clustering Comparison**

A clustering  $\mathcal{C}$  is a partition of a set  $D$  into sets  $C_1, C_2, \dots, C_K$ , called clusters, that satisfy the following for all  $k, l \in \{1, \dots, K\}$ :

$$C_k \cap C_l = \emptyset \quad (3.26)$$

$$\bigcup_{k=1}^K C_k = D \quad (3.27)$$

1502 If we consider two clusterings,  $\mathcal{C}$  with clusters  $C_1, C_2, \dots, C_K$  and  $\mathcal{C}'$  with clusters  
 1503  $C'_1, C'_2, \dots, C'_K$ . There are a number of measurements we can use to compare  $\mathcal{C}$  and  $\mathcal{C}'$ . In  
 1504 the following, the number of elements in  $D$  is denoted by  $n$ , and the number of elements in  
 1505 cluster  $C_k$  is  $n_k$ .

1506 **Adjusted Rand Index**

1507 The *adjusted Rand Index* is a normalised similarity measure for clusterings based on pair  
 1508 counting.

1509 If we consider the clusterings  $\mathcal{C}$  and  $\mathcal{C}'$ , and denote

1510 • the number of pairs in the same cluster in  $\mathcal{C}$  and  $\mathcal{C}'$  by  $N_{11}$

1511 • the number of pairs in different clusters in  $\mathcal{C}$  and  $\mathcal{C}'$  by  $N_{00}$

### 3.3. Methods

---

1512 • the number of pairs in the same cluster in  $\mathcal{C}$  and different clusters in  $\mathcal{C}'$  by  $N_{10}$

1513 • the number of pairs in different clusters in  $\mathcal{C}$  and the same cluster in  $\mathcal{C}'$  by  $N_{01}$

then the *Rand Index* is defined as

$$RI = \frac{N_{11} + N_{00}}{N_{11} + N_{00} + N_{10} + N_{01}} = \frac{N_{11} + N_{00}}{\binom{n}{2}} \quad (3.28)$$

1514 The Rand Index is 1 when the clusterings are identical, and 0 when the clusterings are com-

1515 pletely different.

The *adjusted Rand Index* intends on correcting the Rand Index for chance matching pairs.

This is defined as

$$ARI = \frac{2(N_{00}N_{11} - N_{01}N_{10})}{(N_{00} + N_{01})(N_{01} + N_{11}) + (N_{00} + N_{10})(N_{10} + N_{11})} \quad (3.29)$$

1516 The adjusted Rand Index is 1 when the clusterings are identical, and 0 when the Rand Index

1517 is equal to its expected value.

#### 1518 Clustering as random variables

If we take any random element of  $D$ , the probability that this element is in cluster  $C_k$  of clustering  $\mathcal{C}$  is

$$P(K = k) = \frac{n_k}{n} \quad (3.30)$$

1519 this defines a probability distribution, which makes the clustering a random variable. Any  
1520 clustering can be considered as a random variable this way.

This means that we can measure any of the information theoretic quantities defined in section 3.3.4 with respect to clusterings. For example, the entropy of a clustering is

$$H(\mathcal{C}) = - \sum_{k=1}^K \frac{n_k}{n} \log \frac{n_k}{n} \quad (3.31)$$

If we have two clusterings, the joint probability distribution of these clusterings is defined as

$$P(K = k, K' = k') = \frac{|C_k \cap C'_{k'}|}{n} \quad (3.32)$$

1521 The joint distribution allows us to define the mutual information between two clusterings,

1522  $I(\mathcal{C}; \mathcal{C}')$  (Meilă, 2007).

1523 **Information based similarity measures**

The mutual information between two clusterings is a similarity measure, with  $I(\mathcal{C}; \mathcal{C}') = 0$  if  $\mathcal{C}$  and  $\mathcal{C}'$  are completely different, and  $I(\mathcal{C}; \mathcal{C}') = H(\mathcal{C}) = H(\mathcal{C}')$  if  $\mathcal{C}$  and  $\mathcal{C}'$  are identical. This can be normalised in a number of different ways to make more similarity measures (Vinh, Epps, and Bailey, 2010)

$$NMI_{joint} = \frac{I(\mathcal{C}; \mathcal{C}')}{H(\mathcal{C}, \mathcal{C}')} \quad (3.33)$$

$$NMI_{max} = \frac{I(\mathcal{C}; \mathcal{C}')}{\max\{H(\mathcal{C}), H(\mathcal{C}')\}} \quad (3.34)$$

$$NMI_{sum} = \frac{2I(\mathcal{C}; \mathcal{C}')}{H(\mathcal{C}) + H(\mathcal{C}')} \quad (3.35)$$

$$NMI_{sqrt} = \frac{I(\mathcal{C}; \mathcal{C}')}{\sqrt{H(\mathcal{C})H(\mathcal{C}')}} \quad (3.36)$$

$$NMI_{min} = \frac{I(\mathcal{C}; \mathcal{C}')}{\min\{H(\mathcal{C}), H(\mathcal{C}')\}} \quad (3.37)$$

We can control for chance similarities between the two clusterings by measuring the *adjusted mutual information* between the clusterings. This is defined as

$$AMI_{sum} = \frac{I(\mathcal{C}; \mathcal{C}') - E\{I(\mathcal{C}; \mathcal{C}')\}}{\frac{1}{2}[H(\mathcal{C}) + H(\mathcal{C}')] - E\{I(\mathcal{C}; \mathcal{C}')\}} \quad (3.38)$$

1524 The first term in the denominator, taking the average of the marginal entropies, can be re-  
1525 placed by taking the maximum, minimum, or the geometric mean (Vinh, Epps, and Bailey,  
1526 2010).

1527 **Information based metrics**

The variation of information between two clusterings  $VI(\mathcal{C}; \mathcal{C}')$  (see section 3.3.4) is a metric on the space of clusterings (Meilă, 2007). That is,

$$VI(\mathcal{C}; \mathcal{C}') \geq 0 \quad (3.39)$$

$$VI(\mathcal{C}; \mathcal{C}') = 0 \iff \mathcal{C} = \mathcal{C}' \quad (3.40)$$

$$VI(\mathcal{C}; \mathcal{C}') = VI(\mathcal{C}'; \mathcal{C}) \quad (3.41)$$

$$VI(\mathcal{C}; \mathcal{C}'') \leq VI(\mathcal{C}; \mathcal{C}') + VI(\mathcal{C}'; \mathcal{C}'') \quad (3.42)$$

### 3.4. Results

---

Another metric is the *information distance* (Vinh, Epps, and Bailey, 2010)

$$D_{max} = \max\{H(\mathcal{C}), H(\mathcal{C}')\} - I(\mathcal{C}; \mathcal{C}') \quad (3.43)$$

Both of these can be normalised

$$NVI(\mathcal{C}; \mathcal{C}') = 1 - \frac{I(\mathcal{C}; \mathcal{C}')}{H(\mathcal{C}, \mathcal{C}')} \quad (3.44)$$

$$d_{max} = 1 - \frac{I(\mathcal{C}; \mathcal{C}')}{\max\{H(\mathcal{C}), H(\mathcal{C}')\}} \quad (3.45)$$

#### 1528 Comparing detected communities and anatomical divisions

1529 In order to quantify the difference or similarity between the communities detected in our  
1530 correlation network and the anatomical classification of the cells in that network, we considered  
1531 the communities and the anatomical regions as clusters in two different clusterings,  $\mathcal{C}_{comm}$   
1532 and  $\mathcal{C}_{anat}$ , respectively. We then measured the similarity between the clusterings using the  
1533 mutual information, the adjusted mutual information, and the normalised mutual informa-  
1534 tion. We measured the difference between, or the distance between, the clusterings using the  
1535 variation of information, the normalised variation of information, and the normalised infor-  
1536 mation distance. We also measured the difference between the clusterings using the adjusted  
1537 Rand Index, just to use a non-information based measure.

1538 We took all of these measures for communities detected using different time bin widths.  
1539 This gave us an idea of the effect of time bin width on correlation networks in neural ensem-  
1540 bles relative to anatomical regions within those ensembles.

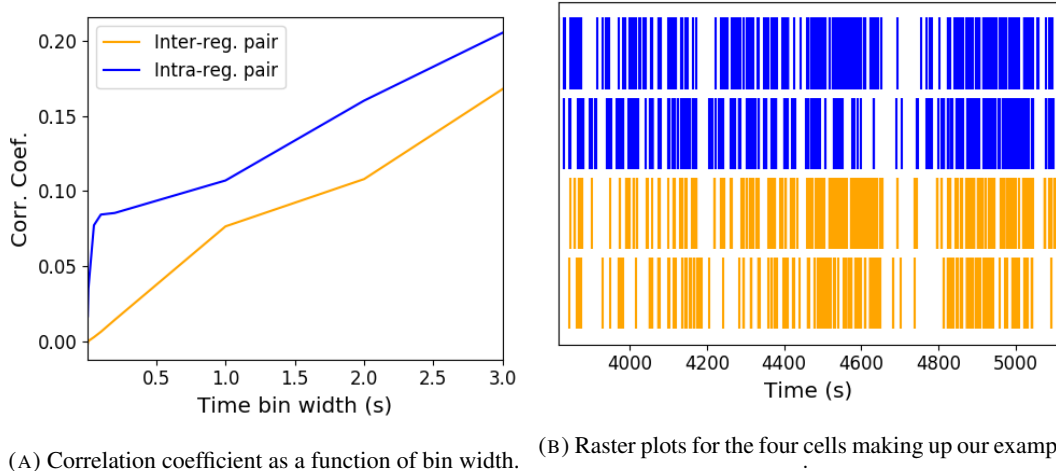
## 1541 3.4 Results

1542 Note that in the following text, we refer to the correlation coefficient between two sequences  
1543 of spike counts from two different cells as the *total correlation*. We refer to the correlation  
1544 between spike counts in response to a certain stimulus as the *spike count correlation* aka  
1545 *noise correlation*, and we refer to the correlation between mean or expected responses to  
1546 different stimuli as the *signal correlation* (Cohen and Kohn, 2011).

1547 The nine different brain regions from which we had data were the caudate putamen (CP),  
1548 frontal motor cortex (FrMoCtx), hippocampus (HPF), lateral septum (LS), midbrain (MB),  
1549 primary visual cortex (V1), superior colliculus (SC), somatomotor cortex (SomMoCtx), and  
1550 thalamus (TH).

1551 **3.4.1 Average correlation size increases with increasing time bin width**

1552 First we inspected the affect of time bin width on total correlations. We know that using short  
 1553 time bins results in artificially small correlation measurements (Cohen and Kohn, 2011), so  
 1554 we expected to see an increase in correlation amplitude with increasing time bin width. That  
 1555 is exactly what we observed. Taking 50 cells at random, we calculated the total correla-  
 1556 tion between every possible pair of these cells, using different time bin widths ranging from  
 1557 0.005s to 3s. We found that the longer the time bin width, the greater the correlations (see  
 1558 figure 3.4a).



(A) Correlation coefficient as a function of bin width. (B) Raster plots for the four cells making up our example pairs.

FIGURE 3.3: (A) An example of the correlation coefficients between two different pairs of cells, one where both cells are in the same brain region (intra-regional pair), and one where both cells are in different brain regions (inter-regional pair). The correlation coefficients have been measured using different time bin widths, ranging from 5ms to 3s. Note the increasing amplitude of the correlations with increasing bin width. (B) A raster plot showing the spike times of each pair of cells.

1559 We also separated the positively correlated pairs from the negatively correlated pairs  
 1560 using the mean correlation of each pair across all bin widths (see section 3.3.2). We found  
 1561 that the positively correlated pairs become more positively correlated with increasing time bin  
 1562 width, and the negatively correlated pairs become more negatively correlated with increasing  
 1563 time bin width (see figures 3.4b and 3.4c).

1564 In figure 3.3a we plot correlations from two example pairs, one pair from within a region,  
 1565 and one pair between regions. It can be seen that the correlation coefficient increases with  
 1566 bin width. The correlations can be observed by eye in the raster plot for these cells in figure  
 1567 3.3b.

1568 When taking the mean across all pairs, the positively correlated pairs dominate in terms  
 1569 of both number of pairs, and amplitude of correlations. Therefore the mean across all pairs

### 3.4. Results

---

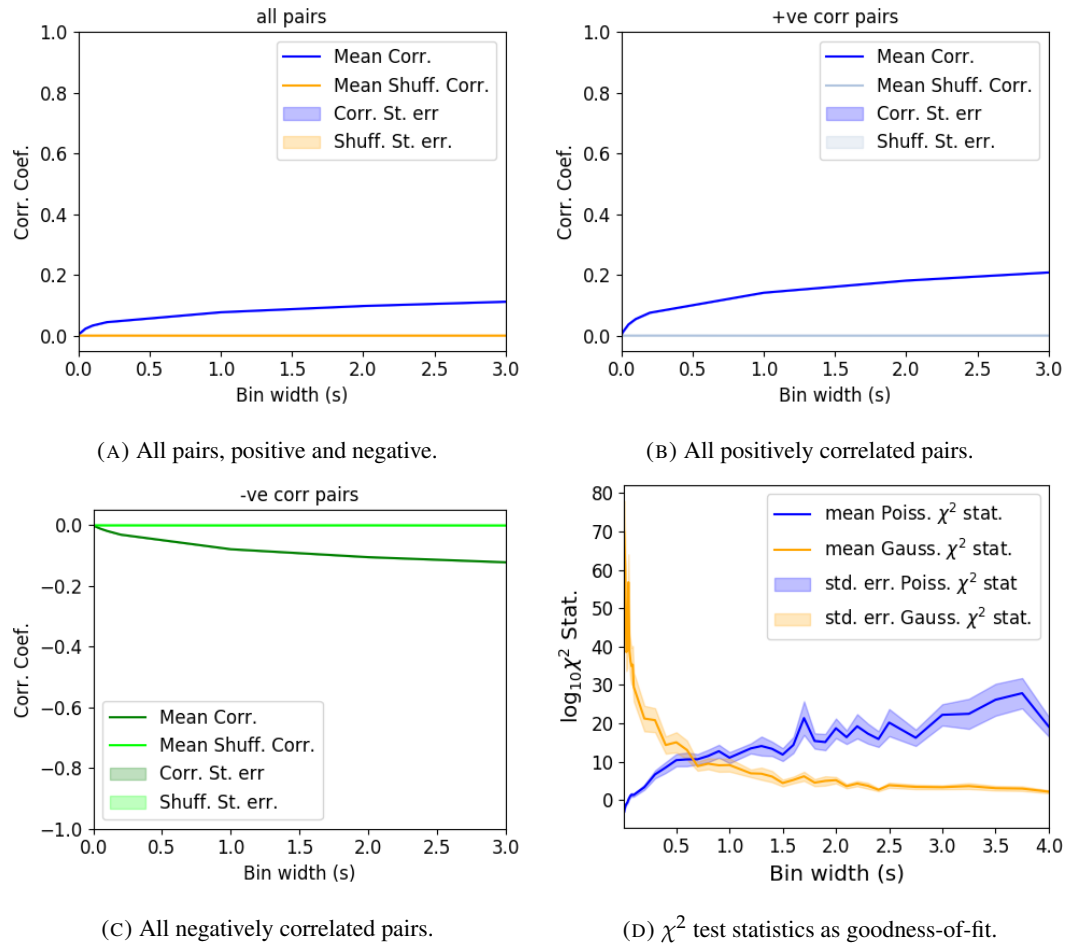


FIGURE 3.4: Mean correlation coefficients measured from pairs of 50 randomly chosen neurons. (A) All possible pairs, (B) positively correlated pairs, and (C) negatively correlated pairs. (D) Mean and standard error of  $\chi^2$  test statistics for Poisson and Gaussian distributions fitted to neuron spike counts.

1570 is positive.

1571 These results were observed in each of the three mouse subjects from which we had data.

### 1572 3.4.2 Goodness-of-fit for Poisson and Gaussian distributions across increasing 1573 time bin widths

1574 We wanted to investigate if the width of the time bin used to bin spike times into spike counts  
1575 had an effect on the distribution of spike counts. We used the  $\chi^2$  statistic as a goodness-of-fit  
1576 measure for Poisson and Gaussian (normal) distributions to the spike count of 100 randomly  
1577 chosen neurons for a number of bin widths ranging from 0.01s to 4s. For the  $\chi^2$  statistic, the  
1578 higher the value, the worse the fit.

1579 We expected a Poisson distribution to be a better fit for shorter time bin widths because  
1580 spike counts must be non-negative, therefore any distribution of spike counts with mass dis-  
1581 tributed at or close to 0 will be skewed. The distribution of spike counts is more likely to be  
1582 distributed close to 0 when the time bin widths used to bin spike times into spike counts are  
1583 small relative to the amount of time it takes for a neuron to fire an action potential ( $\sim 1\text{ms}$  in  
1584 the case of non-burst firing neurons).

1585 We expected a Gaussian distribution to be a better fit for longer time bin widths, because  
1586 a Poisson distribution with a large rate is well approximated by a Gaussian distribution with  
1587 mean and variance equal to the Poisson rate. Therefore, a Gaussian distribution would ap-  
1588 proximate the mean of a collection of large spike counts, and have more flexibility than a  
1589 Poisson distribution to fit the variance.

1590 We found that that a Poisson distribution is the best fit for shorter time bins less than 0.7s  
1591 in length. Then a Gaussian distribution is a better fit for time bins greater than 0.7s in length  
1592 (see figure 3.4d).

### 1593 3.4.3 Differences between and inter- and intra- regional correlations decrease 1594 with increasing bin width

1595 We investigated the differences in distribution between inter-regional correlations, i.e. corre-  
1596 lations between neurons in different brain regions, and intra-regional correlations, i.e. corre-  
1597 lations between neurons in the same brain region.

1598 Firstly, we investigated these quantities for all possible pairs of  $\sim 500$  neurons taken  
1599 from across all the 9 brain regions from which we had data. We distributed these neurons as  
1600 evenly as possible across all of the regions, so that cells from one region would not dominate  
1601 our data. We observed that the mean intra-regional correlations were always higher than the

### 3.4. Results

---

mean inter-regional correlations for every value of time bin width used. We also observed that as the time bin width increased these mean correlations increased and the difference between the mean inter-regional and intra-regional correlations grew (see figure 3.5 (Left)).

Stringer et al. (2019) had a similar finding using the same data. They used only one value for the time bin width, 1.2s. Using this time bin width to bin spike times and measure total correlations, they found that the mean ‘within-region’ correlations were always greater than the ‘out-of-region’ correlations (Stringer et al., 2019). The figure from their paper showing this result can be seen in figure 3.5 (Right).

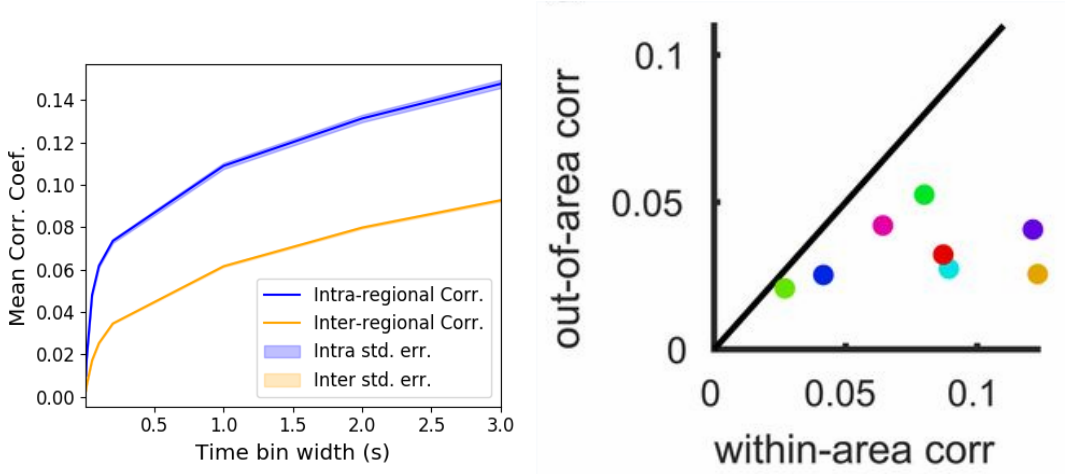
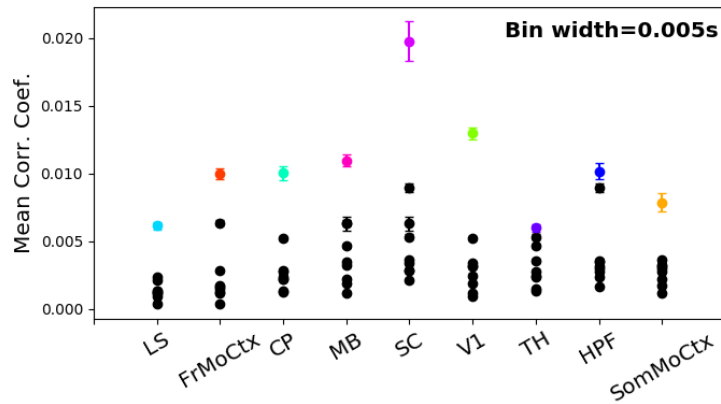


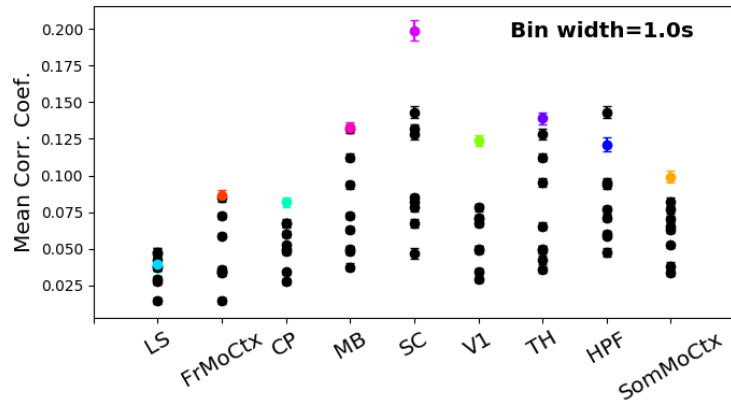
FIGURE 3.5: (Left)The mean intra-region and inter-region correlations using all possible pairs of  $\sim 500$  neurons, spread across 9 different brain regions. (Right) Courtesy of Stringer et al. (2019), mean inter-regional (out-of-area) correlation coefficients vs mean intra-regional (within-area) correlation coefficients for a bin width of 1.2s. Note that the intra-regional coefficients are higher in each case.

Examples of the correlations of one intra-regional pair and one inter-regional pair can be seen in figure 3.3.

Secondly, we separated those pairs into intra-regional and inter-regional groups. We noted that the mean intra-regional correlations (coloured dots in figures 3.6a and 3.6b) for a given region tended to be higher than the mean inter-regional correlations (black dots in figures 3.6a and 3.6b) involving cells from that region. However, in contrast with our previous result, we noted that the difference between the mean intra-regional correlations and most highly correlated inter-regional correlations reduced as we increased the time bin width (see figures 3.6a and 3.6b). This shows that the mean correlations shown in figure 3.5 are not distributed evenly across all region pair combinations.



(A) Mean inter-regional and intra-regional correlations using a time bin width of 5ms.



(B) Mean inter-regional and intra-regional correlations using a time bin width of 1s.

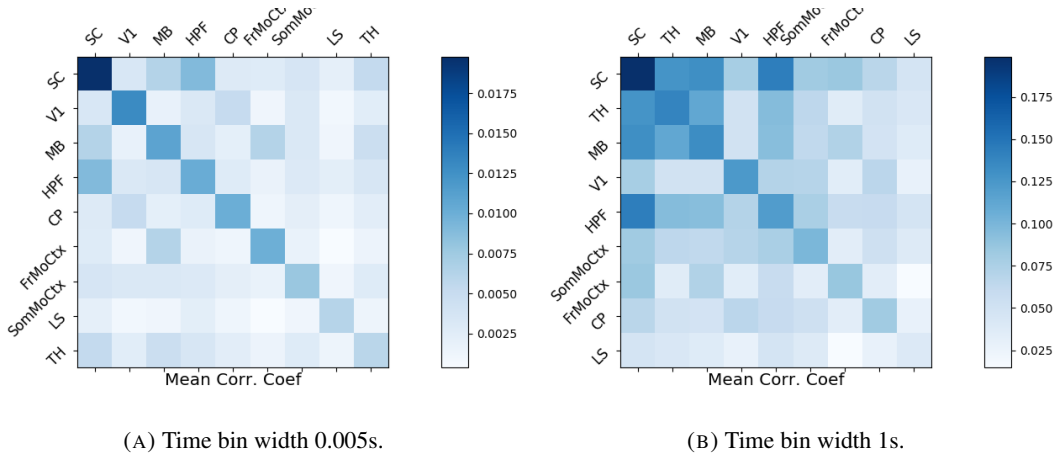
FIGURE 3.6: The mean intra-regional correlations (coloured dots) and mean inter-regional correlations (black dots) for a given region, indicated on the x-axis, for different time bin widths. Each black dot represents the mean inter-regional correlations between the region indicated on the x-axis and one other region. (A) shows these measurements when we used a time bin width of 5ms. (B) shows these measurements when we used a time bin width of 1s. Note that the difference between the mean inter-regional correlations and mean intra-regional correlations is smaller for 1s bins.

### 3.4. Results

---

Finally, to see these regional mean correlations in a bit more detail, to examine the individual pair combinations in particular, we displayed these data in a matrix of mean correlations (see figure 3.7), showing the mean intra-regional correlations on the main diagonal, and the mean inter-regional correlations off diagonal. Comparing a version of this figure created using a short time bin width of 5ms (figure 3.7a) and a version using a longer time bin width of 1s (figure 3.7b) we observed that the mean intra-regional correlations are always relatively high in comparison to the mean inter-regional correlations, but the mean correlations in some inter-regional pairs are relatively much higher when using the longer time bin width.

This could indicate information being processed quickly at a local or within-region level, and the local representations of this information spreading between regions at longer timescales.



(A) Time bin width 0.005s.

(B) Time bin width 1s.

FIGURE 3.7: Mean inter-regional (main diagonal) and intra-regional (off diagonal) correlation coefficients. (A) Shows these measurements when spike times were binned using 5ms time bins. (B) Shows the same, using 1s time bins. Note that the matrices are ordered according to the main diagonal values, therefore the ordering is different in each subfigure.

These results were consistent across the three mouse subjects. But, the relative magnitudes of the mean intra-regional and inter-regional correlations were not consistent. For example, the region with the highest mean intra-regional correlations when using 1s bin widths for subject one is the superior colliculus (SC), but for subject two it is the midbrain (MB).

#### 3.4.4 Connected and divided structure in correlation based networks reduces in dimension with increasing bin width

We used the correlation measurements to create weighted undirected graphs/networks where each node represents a neuron, and the weight of each edge is the pairwise correlation between those neurons represented by the nodes at either end of that edge. We aimed to find

1639 communities of neurons within these networks, and compare the structure of these commu-  
1640 nities to the anatomical division of those neurons. The first step of this process involved  
1641 applying the ‘spectral rejection’ technique developed by Humphries et al (2019) (Humphries  
1642 et al., 2019). This technique compares our data network to a chosen null network model, and  
1643 finds any additional structure in the data network beyond that which is captured in the null  
1644 network model (if there is any such structure).

1645 By comparing the eigenspectrum of the data network to the eigenspectrum of many sam-  
1646 ples from the null network model, this technique allows us to estimate the dimensionality of  
1647 the additional structure in the data network, and gives us a basis for that vector space. It also  
1648 divides the additional structure into connected structure, and  $k$ -partite (or divided) structure.  
1649 For example, if our algorithm found two dimensions of additional connected structure, and  
1650 one dimension of additional divided structure. We might expect to find three communities,  
1651 that is groups more strongly connected within group than without, and we might expect to  
1652 find bi-partite structure, that is two sets that are more strongly connected between groups  
1653 than within groups.

1654 The technique also finds which nodes contribute to this additional structure, and divides  
1655 our data network into signal and noise networks. The details of spectral rejection and node  
1656 rejection can be found in sections 3.3.5 and 3.3.5 respectively, and a full overview can be  
1657 found in (Humphries et al., 2019).

1658 We chose the sparse weighted configuration model (see section 3.3.5) as our null network  
1659 model. This model matches the sparsity and the total weight of the original network but  
1660 distributes the weight at random across the sparse network.

1661 We applied the spectral rejection method to our networks based on total correlations using  
1662 different values for the time bin width. We observed that for smaller time bin widths, our data  
1663 networks had both  $k$ -partite structure, and community structure. As the width of the time bin  
1664 increased, we found that the  $k$ -partite structure disappeared from our data networks, and the  
1665 dimension of the community structure reduced in two of the three mice from which we had  
1666 data (see figure 3.8).

### 1667 3.4.5 Detecting communities in correlation based networks

1668 We applied the community detection procedure described in section 3.3.5 to our signal net-  
1669 works for our various time bin widths. We detected a greater number of smaller communities  
1670 at shorter time bin widths, and a smaller number of larger communities for longer time bin  
1671 widths (see figure 3.9). This was expected after the results found in section 3.4.4. We found

### 3.4. Results

---

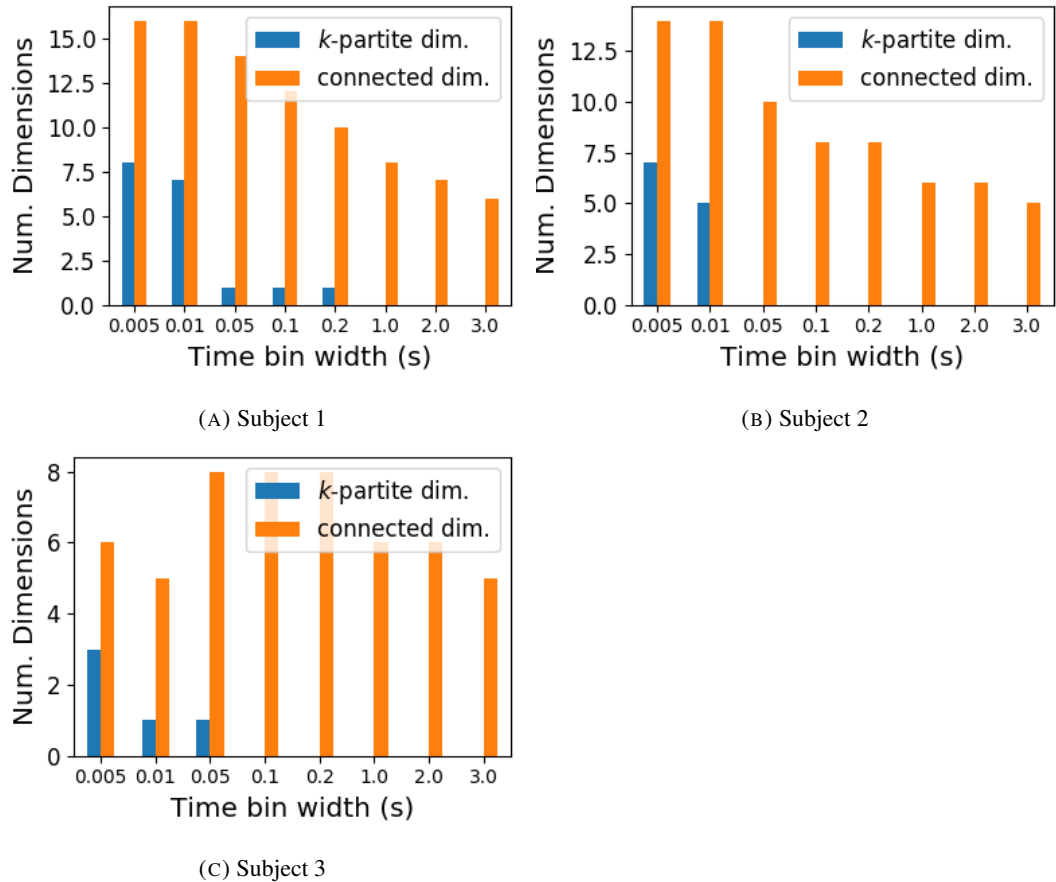


FIGURE 3.8: The number of dimensions in the *k*-partite and connected structure in the correlation based networks beyond the structure captured by a sparse weighted configuration null network model (see section 3.3.5), shown for different time bin widths. Note that the *k*-partite structure disappears for time bin width greater than 200ms for all three subjects. The dimension of the connected structure reduces with increasing bin width for 2 of the 3 subjects (top row).

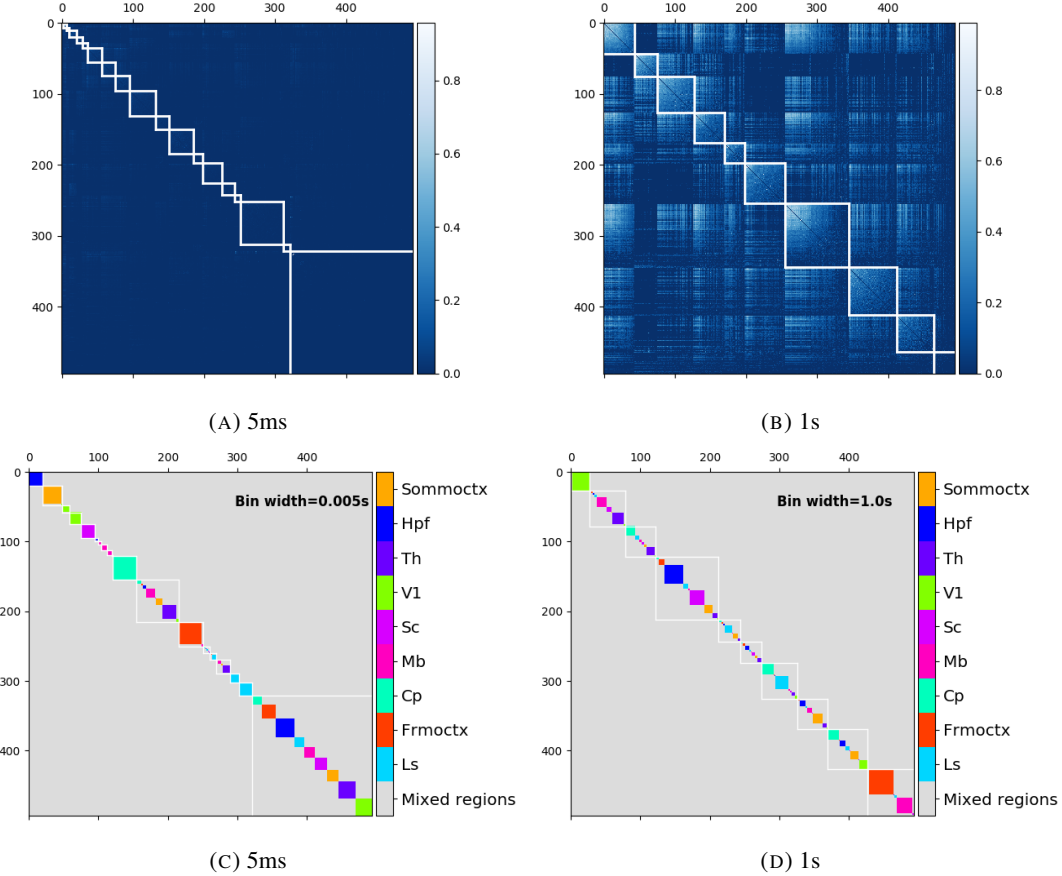


FIGURE 3.9: (A-B) Correlation matrices with detected communities indicated by white lines. Each off main diagonal entry in the matrix represents a pair of neurons. Those entries within a white square indicate that both of those neurons are in the same community as detected by our community detection procedure. Matrices shown are for 5ms and 1s time bin widths respectively. Main diagonal entries were set to 0. (C-D) Matrices showing the anatomical distribution of pairs along with their community membership. Entries where both cells are in the same region are given a colour indicated by the colour bar. Entries where cells are in different regions are given the grey colour also indicated by the colour bar.

### 3.4. Results

---

more dimensions of additional structure at shorter time bin widths, therefore we found more communities at shorter time bin widths.

We also noticed that at short time bin widths the communities detected tended to be dominated by cells from one region. Whereas communities existing in networks created using wider time bin widths tended to contain cells from many different brain regions. More on this in the next section.

#### 3.4.6 Functional communities resemble anatomical division at short timescales

In order to quantify the similarity of the communities detected to the anatomical division of the cells. We treated both the anatomical division and the communities as clusterings of these cells. We then used measures for quantifying the difference or similarity between clusterings to quantify the difference or similarity between the detected communities and the anatomical division. Details of these measures can be found in section 3.3.6 or in (Vinh, Epps, and Bailey, 2010).

We used two different types of measures for clustering comparison; information based measures (see section 3.3.6) and pair counting based measures (see section 3.3.6). We include one example of each in figure 3.10.

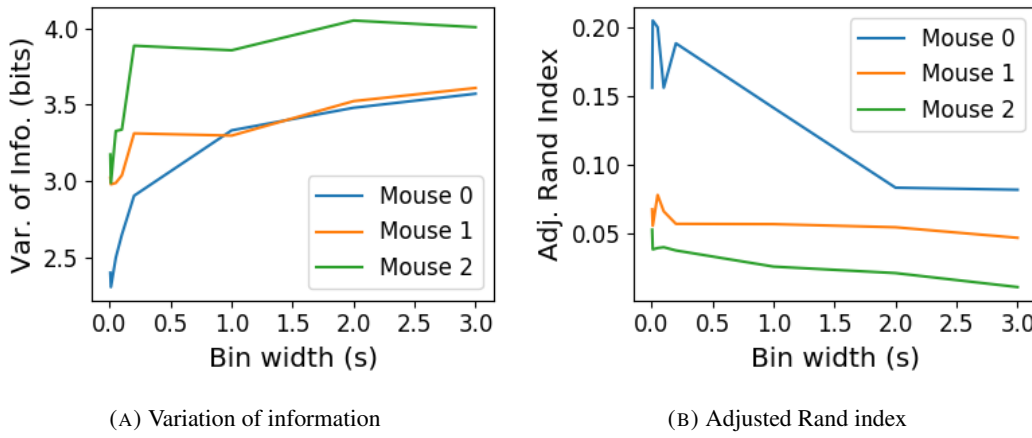
The variation of information is the information based measure included in figure 3.10a. This measure forms a metric on the space of clusterings. The larger the value for the variation of information, the more different the clusterings.

The adjusted Rand index is the pair counting based measure included in figure 3.10b. In contrast with the variation of information, the adjusted Rand index is a normalised similarity measure. The adjusted Rand index takes value 1 when the clusterings are identical, and takes value 0 when the clusterings are no more similar than chance.

Both measures indicated that the detected communities and the anatomical division of the cells were more similar when we used shorter time bins widths (see figure 3.10). This indicates that correlated behaviour in neuronal ensembles is more restricted to individual brain regions at short timescales (< 250ms), and the correlated activity spreads out across brain regions over longer time scales.

#### 3.4.7 Conditional correlations & signal correlations

In light of the excellent research of Stringer et al (2019) showing that spontaneous behaviours can drive activity in neuronal ensembles across the visual cortex and midbrain (Stringer et al., 2019), we decided to control for the mouse's behaviour when performing our analyses.



(A) Variation of information

(B) Adjusted Rand index

FIGURE 3.10: (A) The variation of information is a measure of distance between clusterings. The distance between the anatomical ‘clustering’ and community detection ‘clustering’ increases with increasing time bin width. (B) The adjusted Rand index is a normalised similarity measure between clusterings. The anatomical and community detection clusterings become less similar as the time bin width increases.

1704 It is possible that our community detection process may be detecting communities across  
 1705 multiple brain regions at longer time scales due to aggregating neuronal activity driven by  
 1706 several spontaneous behaviours occurring during the time interval covered by a given time  
 1707 bin. A time bin of 1s, for example, could contain a spike count where those spikes were driven  
 1708 by different spontaneous behaviours. We aimed to investigate this possibility by applying our  
 1709 community detection analysis to conditional correlation measures.

1710 We used the top 500 principal components of a video of the mouse’s face as a measure of  
 1711 the mouse’s behaviour (see section 3.2.2). We modelled the spike counts as a linear combi-  
 1712 nation of the principal components using linear regression with ElasticNet regularisation (see  
 1713 section 3.3.3). Using this model, we quantified the expected spike count given the mouse’s  
 1714 behaviour  $E[X|Z_1, \dots, Z_{500}]$ .

1715 We used these expected values to measure  $\text{cov}(E[X|Z], E[Y|Z])$ , and we used that value,  
 1716 the covariance  $\text{cov}(X, Y)$ , and the *law of total covariance* (see section 3.3.3) to measure  
 1717  $E[\text{cov}(X, Y|Z)]$ . Here  $X$  and  $Y$  represent spike counts from individual cells, and  $Z$  is short-  
 1718 hand for the 500 principal components mentioned above. The two components of the co-  
 1719 variance,  $\text{cov}(E[X|Z], E[Y|Z])$  and  $E[\text{cov}(X, Y|Z)]$ , represent a ‘signal covariance’ and ex-  
 1720 pected value of a ‘spike count covariance’ respectively, analogous to the signal correlation  
 1721 and spike count correlation (Cohen and Kohn, 2011).

1722 We examined the means of these components for different values of the time bin width  
 1723 (see figure 3.11). We observed a consistent increase in  $E[\text{cov}(X, Y|Z)]$  as the time bin width  
 1724 increased. But we saw different trends for  $\text{cov}(E[X|Z], E[Y|Z])$  for each mouse.

### 3.4. Results

---

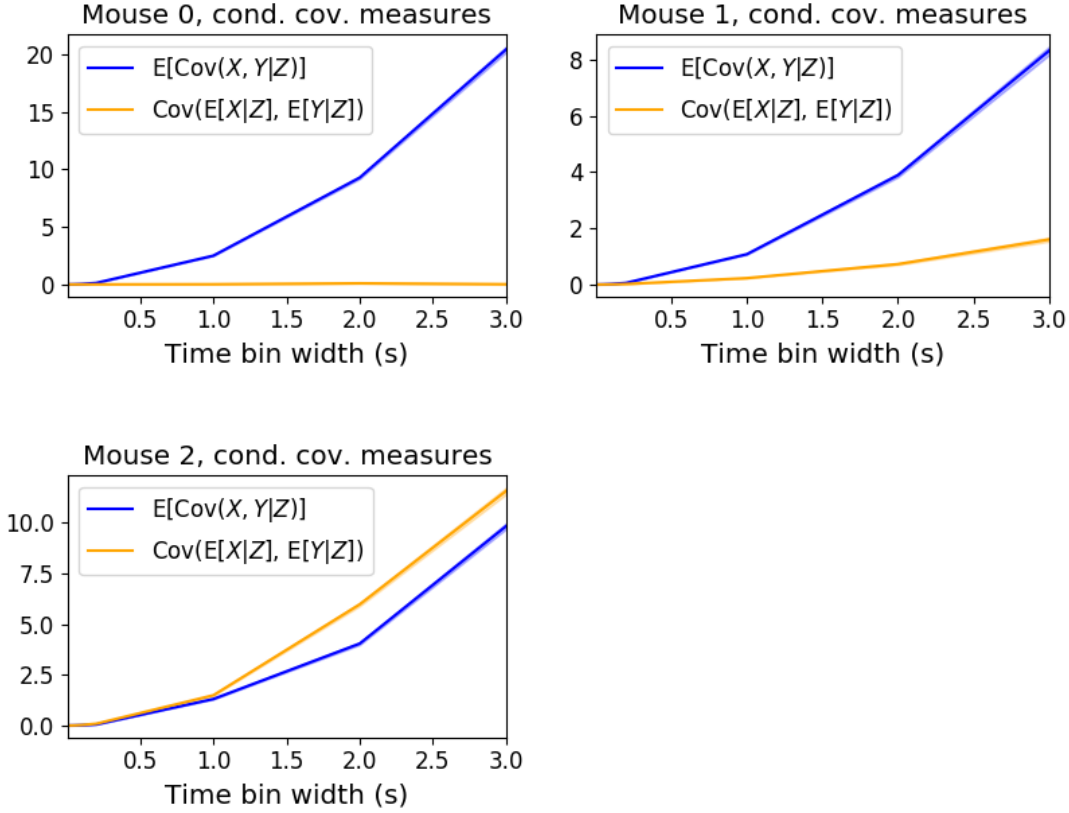


FIGURE 3.11: Comparing the components of the total covariance across different values for the time bin width. We observed a consistent increase in  $E[\text{cov}(X, Y|Z)]$  as the time bin width increased. But we saw different trends for  $\text{cov}(E[X|Z], E[Y|Z])$  for each mouse.

1725 Using  $\text{cov}(E[X|Z], E[Y|Z])$  we measured the signal correlation,  $\rho_{\text{signal}}$ , and using  $E[\text{cov}(X, Y|Z)]$   
 1726 we measured the event conditional correlation,  $\rho_{X,Y|Z}$  (see section 3.3.3 for more details).  
 1727 We saw a consistent increase in  $\rho_{X,Y|Z}$  as the time bin width increased, this corresponds to  
 1728 the result for  $E[\text{cov}(X, Y|Z)]$ . We observed different trends for  $\rho_{\text{signal}}$  for each mouse, this  
 1729 corresponds to the result for  $\text{cov}(E[X|Z], E[Y|Z])$ .

1730 We applied our network noise rejection and community detection process to networks  
 1731 based on the spike count correlations  $\rho_{X,Y|Z}$  and the signal correlations  $\rho_{\text{signal}}$ . We noted that  
 1732 the community detection on  $\rho_{X,Y|Z}$  behaved similarly to the community detection on the total  
 1733 correlation. We can see this in figures 3.13a and 3.13b. At very short time bin widths, we  
 1734 detect more communities, and those communities often contain cells from one brain region  
 1735 only. At longer time bin widths, we detect fewer communities, and those communities tend  
 1736 to contain cells from multiple brain regions. When we examine the distance between (or  
 1737 similarity between) the anatomical division of the cells, and the detected communities we  
 1738 notice that the two clusterings are more similar at shorter time bin widths (see figure 3.14).

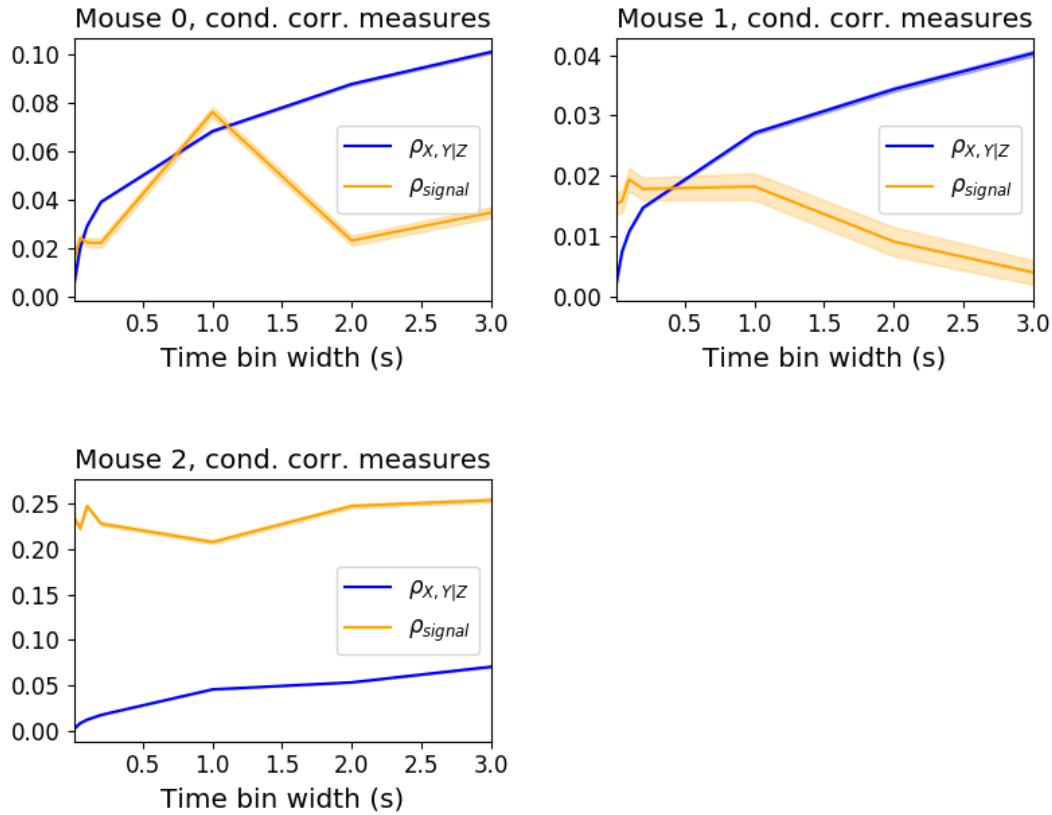


FIGURE 3.12: Comparing the components of the total covariance across different values for the time bin width. We saw a consistent increase in  $\rho_{X,Y|Z}$  as the time bin width increased in all three subjects. But we saw different trends in  $\rho_{signal}$  for each of the subjects.

When we applied the network noise rejection and community detection process to the networks based on the signal correlations  $\rho_{signal}$  we found the number of communities we detected reduced with increasing time bin width. But the number of communities detected was less than that for the total correlations or the spike count correlations. The communities detected always tended to contain cells from multiple regions at both short and long timescales (see figures 3.13c and 3.13d). The communities detected bore very little relation to the anatomical division of the cells. The adjusted Rand index between the community clustering and the anatomical ‘clustering’ is close to zero for every time bin width (see figure 3.15b). This indicates that the similarity between the clusterings is close to chance. We did observe a slight downward trend in the variation of information with increasing bin width (see figure 3.15a), but this is more likely due to a decrease in the number of communities detected rather than any relationship with anatomy.

We also observed that the network noise rejection process rejected some of the cells when applied to the network based on the signal correlations. This means that those cells

### 3.4. Results

---

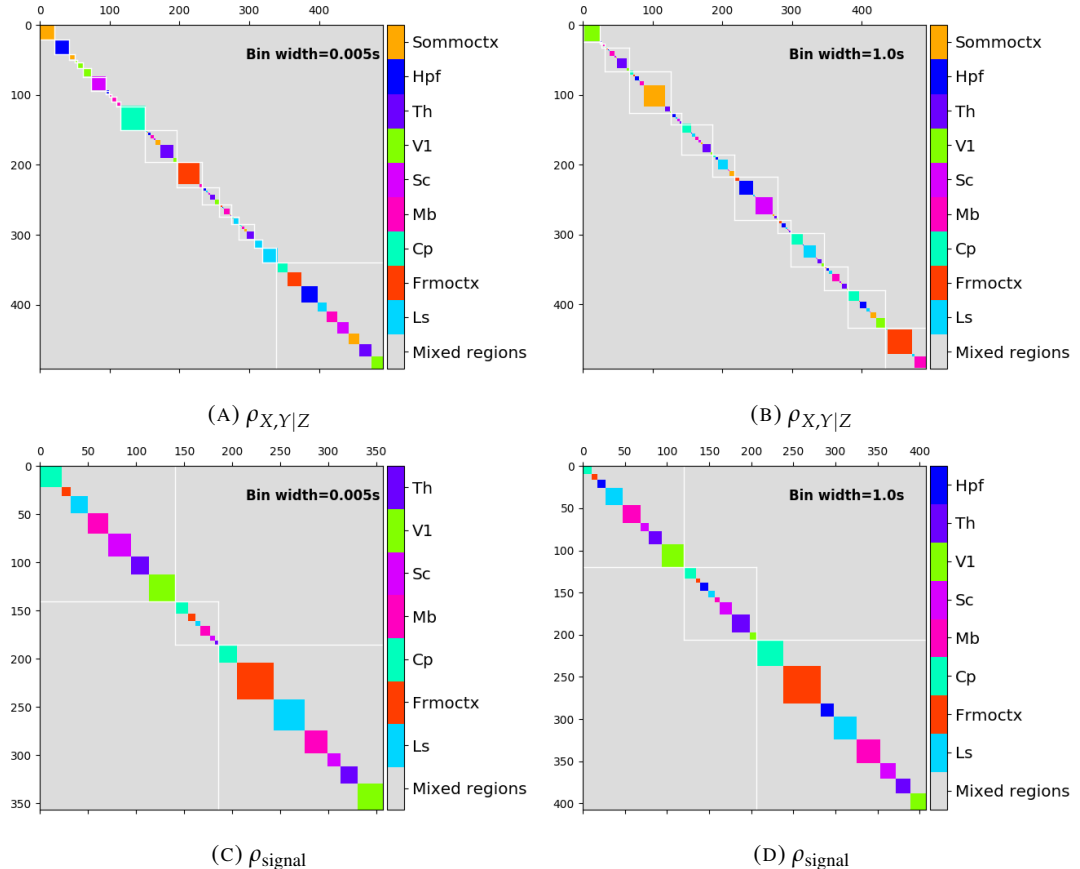


FIGURE 3.13: Matrices showing the regional membership of pairs by colour, and the communities in which those pairs lie. (A-B) Detected communities and regional membership matrix for network based on rectified spike count correlation  $\rho_{X,Y|Z}$ , using time bin widths of 0.005s and 1s respectively. (C-D) Detected communities and regional membership matrix for network based on rectified signal correlation  $\rho_{\text{signal}}$ , using time bin widths of 0.005s and 1s respectively.

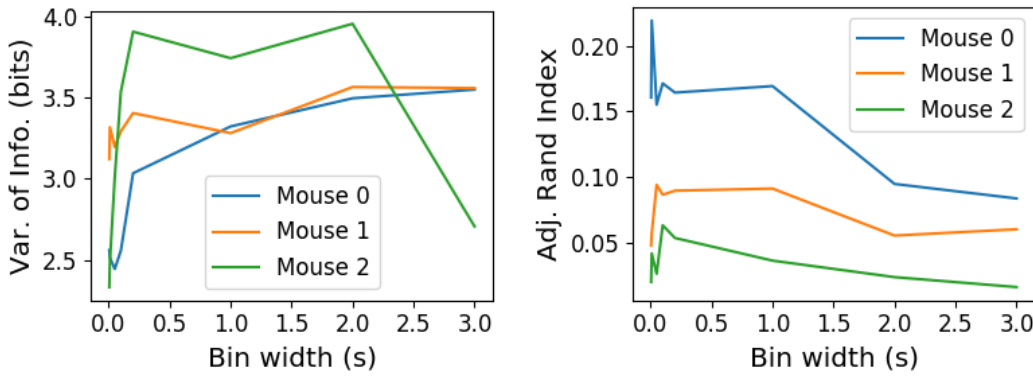
(A)  $\rho_{X,Y|Z}$  Variation of information.(B)  $\rho_{X,Y|Z}$  Adjusted Rand Index.

FIGURE 3.14: Distance and similarity measures between the anatomical division of the neurons, and the communities detected in the network based on the spike count correlations  $\rho_{X,Y|Z}$ . (A) The variation of information is a ‘distance’ measure between clusterings. The distance between the anatomical ‘clustering’ and the community clustering increases as the time bin width increases. (B) The adjusted Rand index is a similarity measure between clusterings. The detected communities become less similar to the anatomical division of the cells as the time bin width increases.

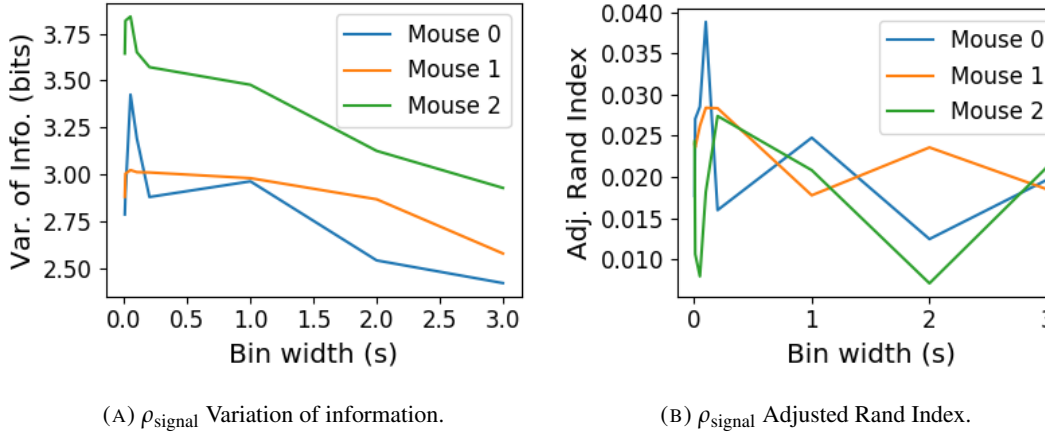
1753 did not contribute to the additional structure of the network beyond that captured by the  
 1754 sparse weighted configuration model. This is why the matrices in figures 3.13c and 3.13d are  
 1755 smaller than their analogues in figures 3.13a and 3.13b.

### 1756 3.4.8 Absolute correlations and negative rectified correlations

1757 At the moment, the network noise rejection protocol can only be applied to weighted undi-  
 1758 rected graphs with non-negative weights. This meant that we had to rectify our correlated  
 1759 networks before applying the network noise rejection and community detection process. We  
 1760 wanted to investigate what would happen if instead of rectifying the correlations, we used the  
 1761 absolute value, or reversed the signs of the correlations and then rectified.

1762 When we used the absolute value of the correlations, we found very similar results to  
 1763 those shown above for the rectified total correlations and the rectified spike count corre-  
 1764 lations. We detected more communities using shorter bin widths, and these communities  
 1765 were more similar to the brain’s anatomy than those communities detected using a longer bin  
 1766 width (see figure 3.16). The only exception being that we detected more communities. This  
 1767 could indicate that we detected both positively and negatively correlated communities, but  
 1768 we haven’t done any further investigation so we cannot say for sure.

1769 When we used the sign reversed rectified correlated networks, we tended to find fewer  
 1770 communities. Each community contained cells from many different anatomical regions, at



(A)  $\rho_{\text{signal}}$  Variation of information.

(B)  $\rho_{\text{signal}}$  Adjusted Rand Index.

FIGURE 3.15: Distance and similarity measures between the anatomical division of the neurons, and the communities detected in the network based on the signal correlations  $\rho_{\text{signal}}$ . (A) The variation of information is a ‘distance’ measure between clusterings. The distance between the anatomical ‘clustering’ and the community clustering increases as the time bin width increases. (B) The adjusted Rand index is a similarity measure between clusterings. The detected communities become less similar to the anatomical division of the cells as the time bin width increases.

1771 both long and short bin widths (see figures 3.17a, 3.17b, 3.17c, 3.17d). The communities  
 1772 bore little relation to the anatomical distribution of the cells, this can be seen in figure 3.17f,  
 1773 the values close to zero indicate that the similarity between the two clusterings are around  
 1774 chance level. This indicates that there was not much structure in the negatively correlated  
 1775 networks beyond that captured by the sparse weighted configuration model.

## 1776 3.5 Discussion

1777 It is well established that the brain uses correlated behaviour in neuronal ensembles to repre-  
 1778 sent the information taken in through sensation (Cohen and Maunsell, 2009; Litwin-Kumar,  
 1779 Chacron, and Doiron, 2012; deCharms and Merzenich, 1996). However, most studies that  
 1780 examine the nature of these correlations in-vivo, study an ensemble of cells from only one  
 1781 or two brain regions (Cohen and Kohn, 2011; Wierzynski et al., 2009; Patterson et al., 2014;  
 1782 Girard, Hupé, and Bullier, 2001). Furthermore, recent results have shown that behaviour can  
 1783 drive correlated activity in multiple brain regions, including those not normally associated  
 1784 with motor control (Stringer et al., 2019; Gründemann et al., 2019; Allen et al., 2019). In this  
 1785 study, we utilised one of the newly recorded large datasets containing electrophysiological  
 1786 recordings from multiple brain regions simultaneously. We investigated correlated behaviour  
 1787 in these different brain regions and we investigated correlated behaviour between neurons in  
 1788 different regions, during spontaneous behaviour.

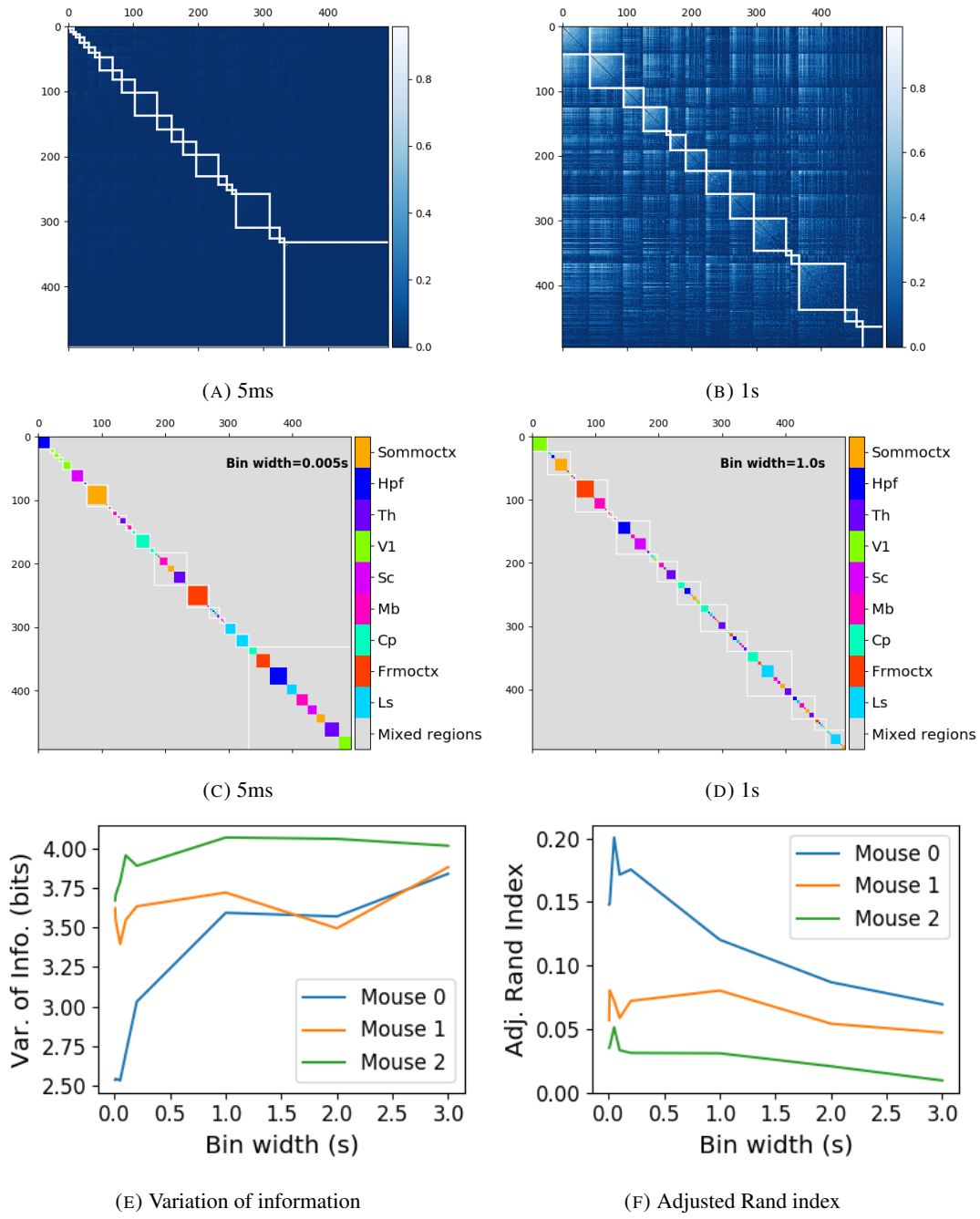


FIGURE 3.16: (A-B) Absolute correlation matrices with detected communities indicated by white lines. These communities are based on the absolute value of the total correlation between each pair of cells. Those entries within a white square indicate that both of those neurons are in the same community. Matrices shown are for 5ms and 1s time bin widths respectively. Main diagonal entries were set to 0. (C-D) Matrices showing the anatomical distribution of pairs along with their community membership. Regional membership is indicated by the colour bar. (E) Variation of information between the anatomical division of the cells, and the detected communities. (F) Adjusted Rand index between the anatomical division, and the detected communities.

### 3.5. Discussion

---

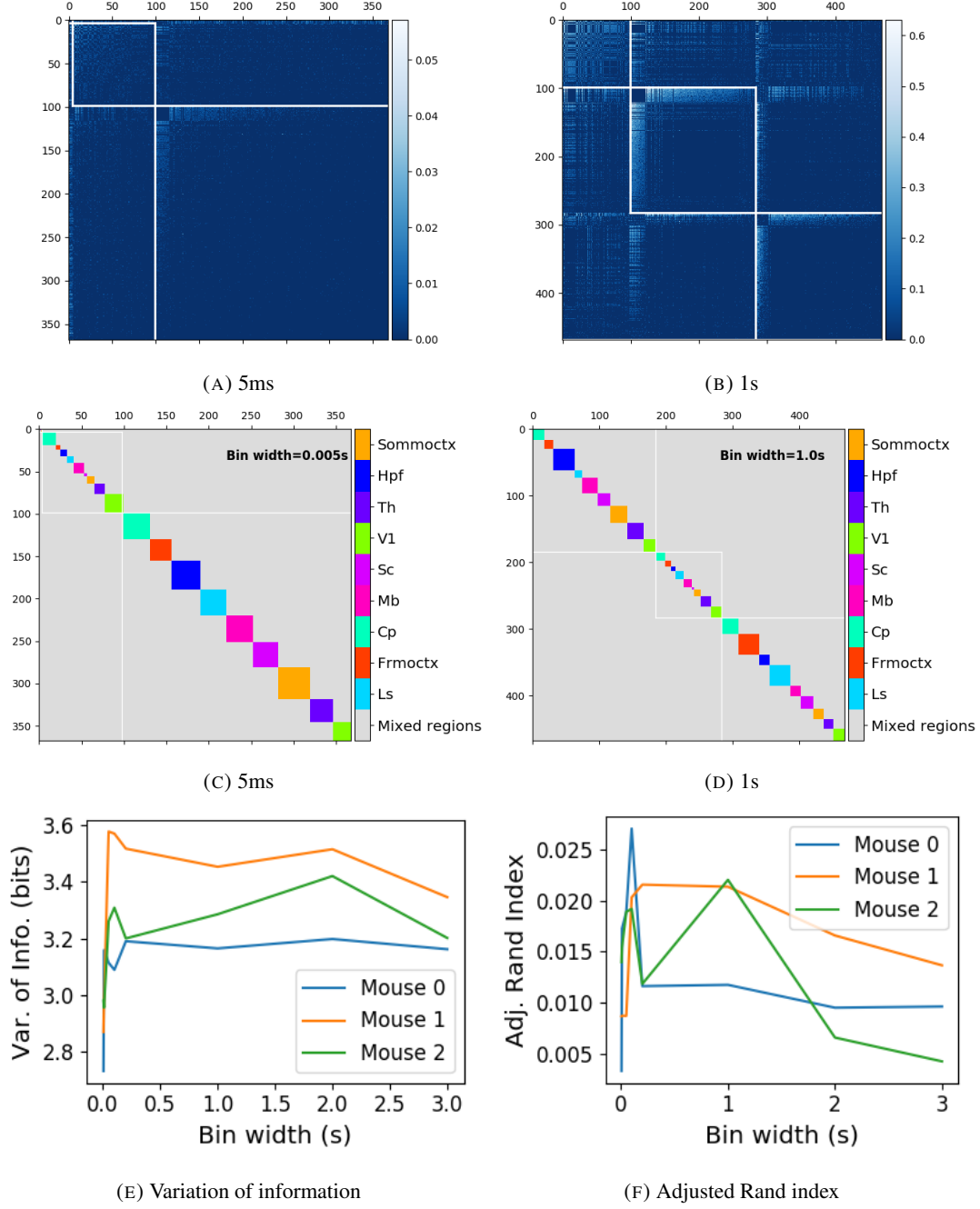


FIGURE 3.17: (A-B) Sign reversed rectified correlation matrices with detected communities indicated by white lines. Those entries within a white square indicate that both of those neurons are in the same community. Matrices shown are for 5ms and 1s time bin widths respectively. Main diagonal entries were set to 0. (C-D) Matrices showing the anatomical distribution of pairs along with their community membership. Regional membership is indicated by the colour bar. (E) Variation of information between the anatomical division of the cells, and the detected communities. (F) Adjusted Rand index between the anatomical division, and the detected communities.

1789 A number of studies have found that the timescale of correlated behaviour induced by a  
1790 stimulus can be modulated by the stimulus structure and behavioural context. For example,  
1791 the spike train correlations between cells in weakly electric fish are modulated by the spa-  
1792 tial extent of the stimulus (Litwin-Kumar, Chacron, and Doiron, 2012), and neurons in the  
1793 marmoset primary auditory cortex modulate their spike timing (and therefore correlation) in  
1794 response to stimulus features without modulating their firing rate (deCharms and Merzenich,  
1795 1996). Furthermore, the width of the time bins over which spike counts are measured has  
1796 been shown to have an effect on the magnitude of those correlations (Cohen and Kohn, 2011).  
1797 Despite this, very little research has been done comparing correlation measures from the same  
1798 dataset at different timescales. We investigated this by varying the time bin width used to bin  
1799 spike times into spike counts from as short as 5ms up to 3s.

1800 In order to further investigate the effect of these correlations at different timescales, we  
1801 regarded our neuronal ensemble as a weighted undirected graph, where each neuron is rep-  
1802 resented by a node, and the weight on each edge is the correlation between the neurons  
1803 connected by that edge. We then applied a novel clustering method from network science  
1804 (Humphries et al., 2019) to identify communities in these networks. Communities in a net-  
1805 work graph refer to sets of nodes that are more strongly connected to each other than the  
1806 nodes outside of their set. Another way to put this is to say that the nodes in a community  
1807 are more strongly connected than *expected*. What connection strength might be expected is  
1808 defined by a null network model. We chose a null network model that matched the sparsity  
1809 and total strength of our correlation based data networks. So, if two cells were in the same  
1810 community, those cells were more correlated than would be expected given the correlation  
1811 strength of their ensemble.

1812 These networks, and the community detection process, were completely agnostic of the  
1813 anatomical division of the cells in our ensemble. When we compared the detected commu-  
1814 nities with the anatomical division of the cells using distance and similarity measures for  
1815 clusterings, we found that the detected communities were more similar to the anatomical  
1816 division at shorter timescales. That is, when we used a wider time bin to count spikes, and  
1817 computed pairwise correlations with these spike counts, the correlated communities tended to  
1818 exist within anatomical regions at shorter timescales, and tended to span anatomical regions  
1819 at longer timescales. This could reflect localised functional correlations at short time scales  
1820 rippling outwards across brain regions at longer timescales. The brain may be processing  
1821 some information quickly locally, and carrying out further, perhaps more detailed, represen-  
1822 tation over a longer timescale across many regions using the representations that were just

### 3.5. Discussion

---

1823 built locally.

1824 These changes in communities across timescales could also be driven by the anatomy  
1825 of the individual cells. For example, it may simply take longer to transmit action potentials  
1826 over longer distances, hence correlated activity over longer timescales will exist between  
1827 anatomical regions, rather than within. However, the switch to almost exclusively multi-  
1828 regional functional networks at 1s bin widths, rather than a mixture of multi-region, and  
1829 single-region suggests that the inter-regional correlations either overpower, or inhibit the  
1830 local correlations. So there may be more at play than just timescales.

1831 We acknowledged that the region spanning correlated communities that we detected at  
1832 longer time scales could exist due to collating activity driven by distinct spontaneous activi-  
1833 ties. In order to account for this, we modelled the spike counts as a linear function of the  
1834 top 500 principal components of a video of the mouse's face filmed simultaneously with the  
1835 electrophysiological readings. We applied our network noise rejection and community de-  
1836 tection process to the weighted undirected networks formed by the spike count correlations  
1837 (or noise correlations) and the signal correlations that we calculated using our model. For the  
1838 spike count correlation networks, we found much the same results as for the total correlations  
1839 as described above. For the signal correlations, the communities detected in these networks  
1840 bore little relation to the anatomical division of the cells. Recent findings have shown that  
1841 behavioural data accounts for correlations in many brain regions that would otherwise be  
1842 dismissed as noise (Stringer et al., 2019), our finding to shows that these correlations are still  
1843 governed by the timescale division between local communication and across-region commu-  
1844 nication.

1845 There is a lot of room for further investigation based on this research. For a start, the  
1846 data that we used here were collected from nine different regions in the mouse brain, but  
1847 none of these regions were part of the somatosensory cortex. Given that a mouse experiences  
1848 so much of its environment through its sense of smell, some data from this region would be  
1849 interesting to investigate. On the same theme, the mice in the experiment from which the  
1850 data were collected were headfixed and placed on a rotating ball, but were otherwise behav-  
1851 ing spontaneously. Had these mice been exposed to a visual, aural, or olfactory stimulus,  
1852 we could have examined the responses of the cells in the brain regions corresponding to vi-  
1853 sion, hearing, and olfaction, and compared these responses to the responses from the other  
1854 brain regions. Furthermore, we could have investigated the interaction between the sets of  
1855 responses.

1856 Another space for further investigation is the community detection. The algorithm that we

1857 used here never detects overlapping communities. But functional communities could indeed  
1858 have overlaps. Clustering methods that detect overlapping clusters do exist (Baadel, Thabtah,  
1859 and Lu, 2016). Applying one of those algorithms could yield some interesting results. Also,  
1860 the community detection algorithm that we used here cannot process graphs with negative  
1861 weights, this forced us to separate positive and negative correlations before applying our  
1862 network noise rejection and community detections process, or use the absolute value of our  
1863 correlations. A community detection algorithm that can work on weighted undirected graphs  
1864 with negative weights could yield some interesting results here.

1865 **Chapter 4**

1866 **A simple two parameter distribution  
1867 for modelling neuronal activity and  
1868 capturing neuronal association**

1869 *Abstract*

1870 Recent developments in electrophysiological technology have lead to an increase in the size  
1871 of electrophysiology datasets. Consequently, there is a requirement for new analysis tech-  
1872 niques that can make use of these new datasets, while remaining easy to use in practice. In  
1873 this work, we fit some one or two parameter probability distributions to spiking data collected  
1874 from a mouse exposed to visual stimuli. We show that the Conway-Maxwell-binomial dis-  
1875 tribution is a suitable model for the number of active neurons in a neuronal ensemble at any  
1876 given moment. This distribution fits these data better than binomial or beta-binomial distribu-  
1877 tions. It also captures the correlated activity in the primary visual cortex induced by stimulus  
1878 onset more effectively than simply measuring the correlations, at short timescales (< 10ms).  
1879 We also replicate the finding of Churchland et al (2010) relating to stimulus onset quenching  
1880 neural variability in cortical areas, and we show a correspondence between this quenching  
1881 and changes in one of the parameters of the fitted Conway-Maxwell-binomial distributions.

1882 **4.1 Introduction**

1883 Recent advances in electrophysiological technology, such as ‘Neuropixels’ probes (Jun et al.,  
1884 2017) have allowed extracellular voltage measurements to be collected from larger numbers  
1885 of cells than traditional methods, in multiple brain regions simultaneously, and routinely.  
1886 These larger datasets require innovative methods to extract information from the data in a  
1887 reasonable amount of time, ‘reasonable’ being subjective in this case.

1888 Theoretically, all the information at any given moment in an electrophysiological dataset  
1889 with  $n$  neurons could be captured by calculating the probability distribution for every possi-  
1890 ble spiking pattern. This would require defining a random variable with  $2^n$  possible values, a  
1891 task that quickly becomes impossible as  $n$  increases. Attempts at approximating this random  
1892 variable often involve measuring pairwise or higher order correlations (Schneidman et al.,  
1893 2006; Flach, 2013; Ganmor, Segev, and Schneidman, 2011). But pairwise correlations may  
1894 not be enough to characterise instantaneous neural activity (Tkačik et al., 2014). Further-  
1895 more, these kinds of models tend to ignore the temporal structure of neuronal data, in favour  
1896 of smaller model size, and scalability.

1897 Higher order correlations would be helpful here, but defining and quantifying these cor-  
1898 relations can be tricky (Staude, Grün, and Rotter, 2010). If we use the interaction parameters  
1899 arising from the exponential family model as measures of higher order correlations, mea-  
1900 suring these correlations becomes computationally impractical quite quickly (the number  
1901 of ‘three neuron correlations’ to measure scales with  $\binom{n}{3}$ ). In this work, we dispense with  
1902 measuring correlations directly, and we attempt to characterise correlated behaviour using a  
1903 parameter in statistical model.

1904 In this work, we examined the ability of simple distributions to model the number of  
1905 active (spiking) neurons in a neuronal ensemble at any given timepoint. We compared a  
1906 little-known distribution named the Conway-Maxwell-binomial distribution to the binomial  
1907 distribution and the beta-binomial distribution. The binomial distribution is a probability dis-  
1908 tribution over the number of successes in a sequence of independent and identical Bernoulli  
1909 trials. The beta-binomial distribution is similar, but allows for a bit more flexibility while still  
1910 being a model for heterogeneity. Similar to the binomial and beta-binomial, the Conway-  
1911 Maxwell-binomial distribution is a probability distribution over the number of successes in a  
1912 series of Bernoulli trials, but allows over- and under-dispersion relative to the binomial dis-  
1913 tribution. This distribution should therefore be a good candidate for our purposes. We found  
1914 that Conway-Maxwell-binomial distribution was usually the best candidate of the three that

## 4.2. Data

---

1915 we examined.

1916 We also observed some interesting changes in the number of active neurons in the primary  
1917 visual cortex and hippocampus at stimulus onset and some changes in this activity in the  
1918 thalamus which were sustained for the full duration of the stimulus presentation. This let us  
1919 know that there were some responses to model.

1920 We found that fitting a Conway-Maxwell-binomial distribution was a better method of  
1921 capturing association between neurons than measuring the spike count correlation for the  
1922 short time bins that we used (< 10ms).

1923 Finally, we also wanted to investigate parallels between the parameters of the Conway-  
1924 Maxwell-binomial distribution and quantities that have been established as relevant to sen-  
1925 sory processing. So, we replicated the findings made by Churchland et al. (2010) relating  
1926 to a reduction in neural variability at stimulus onset in the macaque cortical regions, but for  
1927 data taken from the mouse primary visual cortex. We compared these findings to the values  
1928 of the fitted Conway-Maxwell-binomial distribution parameters.

## 1929 4.2 Data

1930 We used data collected by Nick Steinmetz and his lab ‘CortexLab at UCL’ (Steinmetz, Caran-  
1931 dini, and Harris, 2019). The data can be found online <sup>1</sup> and are free to use for research  
1932 purposes.

1933 Two ‘Phase3’ Neuropixels (Jun et al., 2017) electrode arrays were inserted into the brain  
1934 of an awake, head-fixed mouse for about an hour and a half. These electrode arrays recorded  
1935 384 channels of neural data each at 30kHz and less than 7 $\mu$ V RMS noise levels. The sites  
1936 are densely spaced in a ‘continuous tetrode’-like arrangement, and a whole array records  
1937 from a 3.8mm span of the brain. One array recorded from visual cortex, hippocampus, and  
1938 thalamus, the other array recorded from motor cortex and striatum. The data were spike-  
1939 sorted automatically by Kilosort and manually by Nick Steinmetz using Phy. In total 831  
1940 well-isolated individual neurons were identified.

### 1941 4.2.1 Experimental protocol

1942 The mouse was shown a visual stimulus on three monitors placed around the mouse at right  
1943 angles to each other, covering about  $\pm 135$  degrees azimuth and  $\pm 35$  degrees elevation.

---

<sup>1</sup><http://data.cortexlab.net/dualPhase3/>

1944 The stimulus consisted of sine-wave modulated full-field drifting gratings of 16 drift di-  
1945 rections ( $0^\circ, 22.5^\circ, \dots, 337.5^\circ$ ) with 2Hz temporal frequency and 0.08 cycles/degree spatial  
1946 frequency displayed for 2 seconds plus a blank condition. Each of these 17 conditions were  
1947 presented 10 times in a random order across 170 different trials. There were therefore 160  
1948 trials with a drifting-grating visual stimulus present, and 10 trials with a blank stimulus.

1949 **4.3 Methods**

1950 **4.3.1 Binning data**

1951 We converted the spike times for each cell into spike counts by putting the spike times into  
1952 time bins of a given ‘width’ (in milliseconds). We used time bins of 1ms, 5ms, and 10ms.  
1953 We used different time bin widths to assess the impact of choosing a bin width.

1954 **4.3.2 Number of *active* neurons**

1955 To count the number of active neurons in each neuronal ensemble, we split the time interval  
1956 for each trial into bins of a given width. We counted the number of spikes fired by each cell  
1957 in each bin. If a cell fired *at least* one spike in a given bin, we regarded that cell as active in  
1958 that bin. We recorded the number of active cells in every bin, and for the purposes of further  
1959 analysis, we recorded each cell’s individual spike counts.

1960 It should be noted that when we used a bin width of 1ms, the maximum number of  
1961 spikes in any bin was 1. For the wider time bins, some bins had spike counts greater than  
1962 1. Consequently when using a bin width of 1ms, the number of active neurons and the total  
1963 spike count of a given bin were identical. But for wider bin widths, the total spike count was  
1964 greater than the number of active neurons.

1965 So for the 1ms bin width, the activity of a neuron and the number of spikes fired by that  
1966 neuron in any bin can be modelled as a Bernoulli variable. But for wider time bins, only the  
1967 activity can be modelled in this way.

1968 **4.3.3 Moving windows for measurements**

1969 When taking measurements (e.g. moving average over the number of active neurons) or  
1970 fitting distributions (eg. the beta binomial distribution) we slid a window containing a certain  
1971 number of bins across the data, and made our measurements at each window position. For  
1972 example, when analysing 1ms bin data, we used a window containing 100 bins, and we slid

### 4.3. Methods

---

| Bin width (ms) | Window size (bins) | Window size (ms) | Windows per trial |
|----------------|--------------------|------------------|-------------------|
| 1ms            | 100                | 100ms            | 296               |
| 5ms            | 40                 | 200ms            | 286               |
| 10ms           | 40                 | 400ms            | 266               |

TABLE 4.1: Details of the different bin width and analysis window sizes used when binning spike times, and analysing those data.

1973 the window across the time interval for each trial moving 10 bins at a time. So that for  
 1974 3060ms of data, we made 296 measurements.

1975 For the 5ms bin width data, we used windows containing 40 bins, and slid the window 2  
 1976 bins at a time when taking measurements.

1977 For the 10ms bin width data, we used windows containing 40 bins, and slid the window  
 1978 1 bin at a time when taking measurements (see table 4.1 for concise details).

1979 By continuing to use windows containing 40 bins, we retained statistical power but sac-  
 1980 rificed the number of measurements taken.

1981 There was an interval between each trial with a grey image in place of the moving of  
 1982 the moving bar stimulus. This interval varied in time. But we included some of this interval  
 1983 when recording the data for each trial. We started recording the number of active neurons,  
 1984 and the number of spikes from each neuron from 530ms before each trial until 1030ms after  
 1985 each trial. This way, we could see the change in our measurements at the onset of a stimulus  
 1986 and the end of stimulus presentation.

1987 As mentioned in section 4.3.2, we recorded the number of active neurons in each bin, and  
 1988 the spike count for each neuron in each bin. The actual measurements we took using these  
 1989 data in each window were as follows:

1990 **Moving average** The average number of active cells in each window.

1991 **Moving variance** The variance of the number of active cells in each window.

1992 **Average correlation** We measured the correlation between the spike counts of each pair of  
 1993 cells in the ensemble, and took the average of these measurements.

1994 **Binomial  $p$**  We fitted a binomial distribution to the data in each window and recorded the  
 1995 fitted probability of success,  $p$  in each case.

1996 **Beta-binomial  $\alpha, \beta$**  We fitted a beta-binomial distribution to the data in each window, and  
 1997 recorded the values of the fitted shape parameters,  $\alpha$  and  $\beta$ , of each distribution.

1998 **Conway-Maxwell-binomial distribution  $p, \nu$**  We fitted a Conway-Maxwell-binomial dis-  
1999 tribution to the data in each window, and recorded the fitted values of  $p$  and  $\nu$  for each  
2000 distribution.

2001 **Log-likelihoods** We also recorded the log-likelihood of each of the fitted distributions for  
2002 each window.

2003 **4.3.4 Fano factor**

The *Fano factor* of a random variable is defined as the ratio of the variable's variance to its mean.

$$F = \frac{\sigma^2}{\mu} \quad (4.1)$$

2004 We measured the Fano factor of the spike count of a given cell by measuring the mean and  
2005 variance of the spike count across trials, and taking the ratio of those two quantities. When  
2006 calculated in this way the Fano factor can be used as a measure of neural variability that  
2007 controls for changes in the firing rate. This is similar to the calculation used in (Churchland  
2008 et al., 2010).

2009 **4.3.5 Probability Distributions suitable for modelling ensemble activity**

2010 We present here three different probability distributions that could be suitable to model the  
2011 number of active neurons in an ensemble. Each distribution has the set  $\{0, \dots, n\}$  as its sup-  
2012 port, where  $n$  is the number of neurons in the ensemble. These are simple distributions with  
2013 either two or three parameters each. However, we regard  $n$  as known when using these dis-  
2014 tributions for modelling, so in effect each distribution has either one or two free parameters.

2015 **Association**

2016 *Association* between random variables is similar to the correlation between random variables  
2017 but is more general in concept. The correlation coefficient is a measure of association; and  
2018 association doesn't necessarily have a mathematical definition like correlation does. Essen-  
2019 tially, an association between two random variables is a dependency of any kind. Positively  
2020 associated variables tend to take the same value, and negatively associated variables tend to  
2021 take different values. In this research, we work with probability distributions of the num-  
2022 ber of successes in a set of Bernoulli trials. These Bernoulli variables may or may not be  
2023 associated.

### 4.3. Methods

---

2024 A probability distribution over the number of successes in  $n$  Bernoulli trials, where the  
2025 Bernoulli variables may be associated, could constitute a good model for the number of active  
2026 neurons in an ensemble of  $n$  neurons. As long as the observation period is divided into time  
2027 bins short enough so that any neuron is unlikely to fire more than spike in any time bin.

2028 **Binomial distribution**

The binomial distribution is a two parameter discrete probability distribution that can be thought of as a probability distribution the number of successes from  $n$  independent Bernoulli trials, each with the same probability of success. The parameters of the binomial distribution are  $n$  the number of trials, and  $0 \leq p \leq 1$ , the probability of success for each of these trials. A random variable with the binomial distribution can take values from  $\{0, \dots, n\}$ .

The probability mass function of the distribution is

$$P(k; n, p) = \binom{n}{k} p^k (1-p)^{n-k} \quad (4.2)$$

2029 As a model for the activity of a neuronal ensemble, the main problem with the binomial  
2030 distribution is that it treats each neuron, represented as a Bernoulli trial, as independent. It is  
2031 well known that neurons are not independent, and that correlated behaviour between neurons  
2032 is vital for representing sensory information (Cohen and Maunsell, 2009). The binomial dis-  
2033 tribution falls short in this regard, but it is useful as performance benchmark when assessing  
2034 the performance of other models.

2035 **Beta-binomial distribution**

2036 The beta distribution is the conjugate distribution of the binomial distribution. The beta-  
2037 binomial distribution is the combination of the beta distribution and the binomial distribution,  
2038 in that the probability of success for the binomial distribution is sampled from the beta dis-  
2039 tribution. This allows the beta-binomial distribution to capture some over dispersion relative  
2040 to the binomial distribution.

The beta-binomial distribution is a three parameter distribution,  $n$  the number of Bernoulli trials, and  $\alpha \in \mathbb{R}_{>0}$  and  $\beta \in \mathbb{R}_{>0}$  the shape parameters of the beta distribution. The probability mass function for the beta-binomial distribution is

$$P(k; n, \alpha, \beta) = \binom{n}{k} \frac{B(k + \alpha, n - k + \beta)}{B(\alpha, \beta)} \quad (4.3)$$

2041 where  $B(\alpha, \beta)$  is the beta function.

This probability distribution can be reparametrised in a number of ways. One of which defines new parameters  $\pi$  and  $\rho$  by

$$\pi = \frac{\alpha}{\alpha + \beta} \quad (4.4)$$

$$\rho = \frac{1}{\alpha + \beta + 1} \quad (4.5)$$

2042 This reparametrisation is useful because  $\pi$  acts as a location parameter analogous to the  $p$   
2043 parameter of a binomial distribution. A value of  $\rho > 0$  indicates over-dispersion relative to a  
2044 binomial distribution.

2045 As a model for the activity of a neuronal ensemble, the beta-binomial distribution is  
2046 more suitable than a binomial distribution because the over-dispersion of the beta-binomial  
2047 distribution can be used to model positive association between the neurons. An extreme  
2048 example of this over-dispersion/positive association can be seen in figure 4.1b. In this figure,  
2049 the neurons are positively associated and so tend to take the same value, consequently the  
2050 probability mass of the beta-binomial distribution builds up close to  $k = 0$  and  $k = n$ . It is  
2051 worth noting that the location parameter for each distribution has the same value,  $p = \pi =$   
2052 0.5.

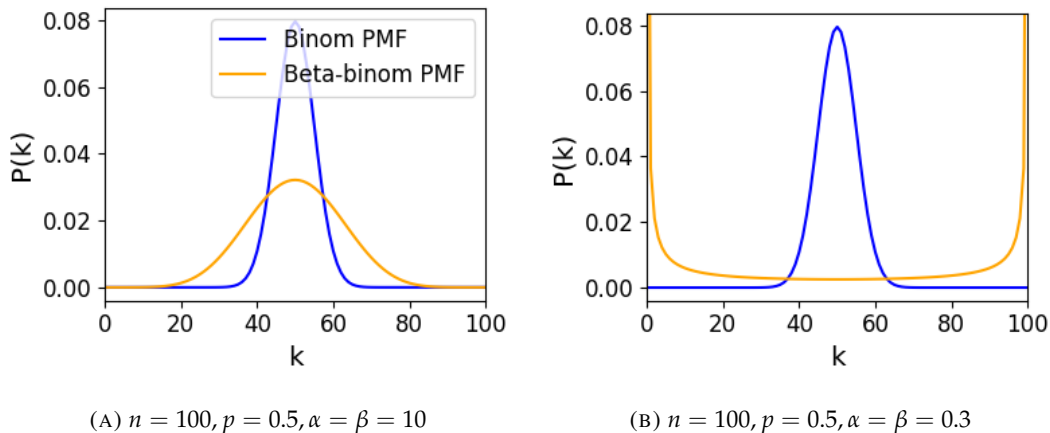


FIGURE 4.1: Figures showing the over-dispersion possible for a beta-binomial distribution relative to a binomial distribution. Parameters are shown in the captions.

2053 **Conway-Maxwell-binomial distribution**

2054 The Conway-Maxwell-binomial distribution (COMb distribution) is a three parameter generalisation of the binomial distribution that allows for over dispersion and under dispersion

### 4.3. Methods

---

relative to the binomial distribution. The parameters of the distribution are  $n$  the number of Bernoulli trials, and two shape parameters  $0 \leq p \leq 1$ , and  $\nu \in \mathbb{R}$ .

The probability mass function of the COMb distribution is

$$P(k; n, p, \nu) = \frac{1}{S(n, p, \nu)} \binom{n}{k}^{\nu} p^k (1-p)^{n-k} \quad (4.6)$$

where

$$S(n, p, \nu) = \sum_{j=0}^n \binom{n}{j}^{\nu} p^j (1-p)^{n-j} \quad (4.7)$$

The only difference between this PMF and the PMF for the standard binomial is the introduction of  $\nu$  and the consequent introduction of the normalising function  $S(n, p, \nu)$ .

Indeed, if  $\nu = 1$  the COMb distribution is identical to the binomial distribution with the same values for  $n$  and  $p$ . We can see in figure 4.2d that the KL-divergence  $D_{KL}(P_{COMb}(n, p, \nu) || P_{Bin}(n, p)) = 0$  along the line where  $\nu = 1$ . The analytical expression for the divergence is

$$D_{KL}(P_{COMb}(k; n, p, \nu) || P_{Bin}(k; n, p)) = (\nu - 1) E_{P_{COMb}(k; n, p, \nu)} \left[ \log \binom{n}{k} \right] \quad (4.8)$$

$$- \log S(n, p, \nu) \quad (4.9)$$

At  $\nu = 1$ , we have  $S(n, p, 1)$  which is just the sum over the binomial PMF, so  $S(n, p, 1) = 1$  and therefore  $D_{KL}(P_{COMb}(n, p, \nu) || P_{Bin}(n, p)) = 0$ .

If  $\nu < 1$  the COMb distribution will exhibit over-dispersion relative to the binomial distribution. If  $p = 0.5$  and  $\nu = 0$  the COMb distribution is the discrete uniform distribution, and if  $\nu < 0$  the mass of the COMb distribution will tend to build up near  $k = 0$  and  $k = n$ . This over-dispersion represents positive association in the Bernoulli variables. An example of this over-dispersion can be seen in figure 4.2b.

If  $\nu > 1$  the COMb distribution will exhibit under-dispersion relative to the binomial distribution. The larger the value of  $\nu$  the more probability mass will build up at  $n/2$  for even  $n$ , or at  $\lfloor n/2 \rfloor$  and  $\lceil n/2 \rceil$  for odd  $n$ . This under-dispersion represents negative association in the Bernoulli variables. An example of this under-dispersion can be seen in figure 4.2a.

It should be noted that the  $p$  parameter of the COMb distribution does not correspond to the mean of the distribution, as is the case for the binomial  $p$  parameter, and beta-binomial  $\pi$  parameter. That is, the COMb  $p$  parameter is not a location parameter. An illustration of this can be seen in figure 4.2c. This is because an interaction between the  $p$  and  $\nu$  parameters skews the mean. There is no analytical expression for the mean of the COMb distribution.

| $\nu$ | Relative dispersion | Association between neurons/variables |
|-------|---------------------|---------------------------------------|
| < 1   | over                | positive                              |
| 1     | none                | none                                  |
| > 1   | under               | negative                              |

TABLE 4.2: Relative dispersion of the COMb distribution, and association between Bernoulli variables as represented by the value of the  $\nu$  parameter.

2076 Since the COMb distribution has the potential to capture positive and negative associa-  
2077 tions between the neurons/Bernoulli variables, it should be an excellent candidate for mod-  
2078 elling the number of active neurons in a neuronal ensemble.

2079 We wrote a dedicated Python package to enable easy creation and fitting of COMb dis-  
2080 tribution objects. The format of the package imitates the format of other distribution objects  
2081 from the `scipy.stats` Python package. The COMb package can be found here:  
2082 [https://github.com/thomasjdelaney/Conway\\_Maxwell\\_Binomial\\_Distribution](https://github.com/thomasjdelaney/Conway_Maxwell_Binomial_Distribution)

### 2083 4.3.6 Fitting

2084 We fitted binomial, beta-binomial, and Conway-Maxwell-binomial (COMb) distributions to  
2085 the neural activity in each of the overlapping windows covering each trial. To fit the distribu-  
2086 tions we minimised the appropriate negative log likelihood function using the data from the  
2087 window.

There is an analytical solution for maximum likelihood estimate of the binomial distribution's  $p$  parameter.

$$\hat{p} = \frac{1}{n} \sum_{i=1}^N k_i \quad (4.10)$$

2088 We minimised the negative log likelihood function of the beta-binomial distribution nu-  
2089 merically. We calculated the negative log likelihood for a sample directly, by taking the sum  
2090 of the log of the probability mass function for each value in the sample. We minimised the  
2091 negation of that function using the `minimise` function of the `scipy.optimize` Python  
2092 package.

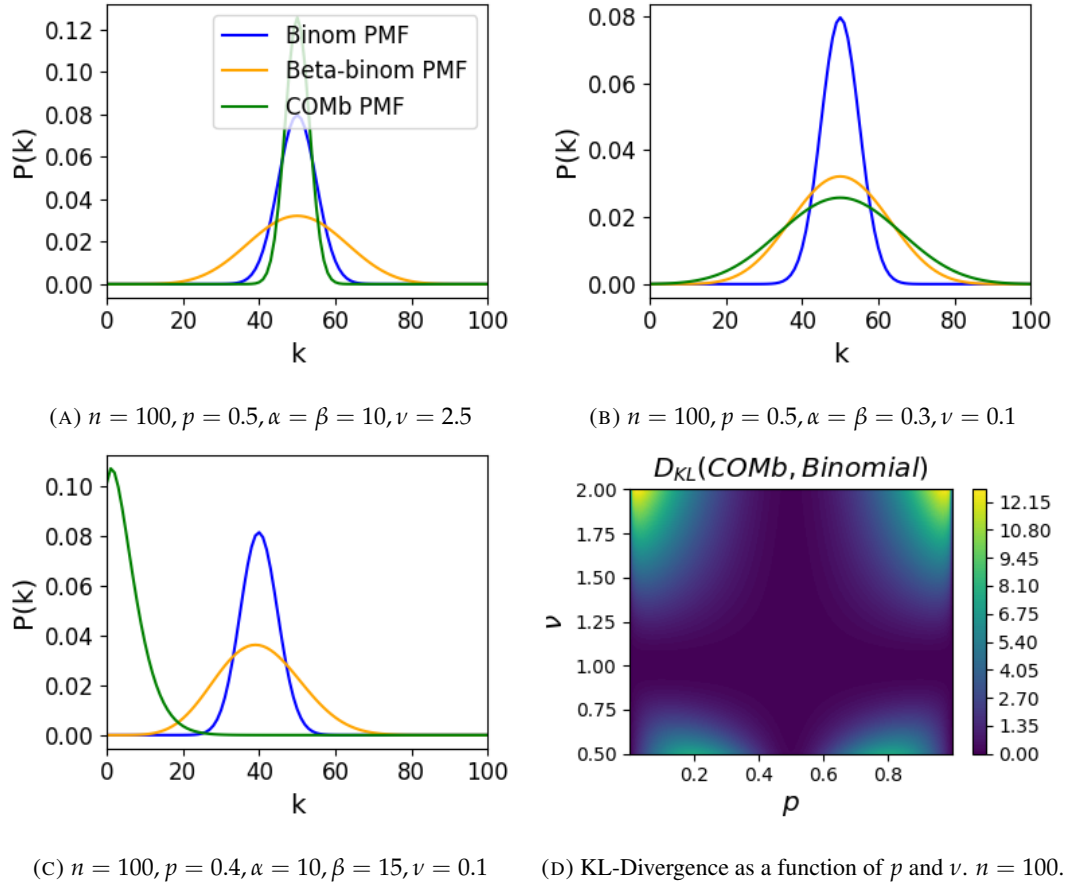


FIGURE 4.2: Figures showing (A) the under-dispersion and (B) over-dispersion permitted by the COMb distribution relative to a binomial distribution. (C) illustrates that the  $p$  parameter of the COMb distribution does not correspond to the mean of the distribution, as it does for the binomial and beta-binomial distributions. (D) shows a heatmap for the value of the Kullback-Liebler divergence between the COMb distribution and the standard binomial distribution with same value for  $n$ , as a function of  $p$  and  $\nu$ . Parameters are shown in the captions.

The log likelihood function of the COMb distribution given some sample  $\{k_1, \dots, k_N\}$  is

$$\ell(p, \nu | k_1, \dots, k_N) = N [n \log(1 - p) - \log S(n, p, \nu)] \quad (4.11)$$

$$+ \log \frac{p}{1 - p} \sum_{i=1}^N k_i \quad (4.12)$$

$$+ \nu \sum_{i=1}^N \log \binom{n}{k_i} \quad (4.13)$$

2093 We minimised the negation of this function using numerical methods. More specifically, we  
2094 used the `minimise` function of the `scipy.optimize` Python package.

2095 **4.3.7 Goodness-of-fit**

2096 After fitting, we measured the goodness-of-fit of each model/distribution with their log like-  
2097 lihood. We calculated this directly using the `logpmf` functions of the distribution objects in  
2098 Python.

2099 **4.4 Results**

2100 We defined a neuron as *active* in a time bin if it fires at least one spike during the time interval  
2101 covered by that bin. We measured the number of active neurons in the primary visual cortex  
2102 of a mouse in 1ms bins across 160 trials of a moving bar visual stimulus. We then slid a  
2103 100ms window across these 1ms bins taking measurements, and fitting distributions along  
2104 the way. We did the same for neurons in the thalamus, hippocampus, striatum, and motor  
2105 cortex. We repeated the analysis for 5ms time bins with 40 bin windows, and 10ms time bins  
2106 with 40 bin windows.

2107 **4.4.1 Increases in mean number of active neurons and variance in number of  
2108 active neurons at stimulus onset in some regions**

2109 We measured the average number of active neurons, and the variance of the number of active  
2110 neurons in a 100ms sliding window starting 500ms before stimulus onset until 1000ms after  
2111 stimulus onset. We found differences in the response across regions. There were no observed  
2112 changes in response to the stimulus in the motor cortex or the striatum. The changes in the  
2113 other regions are detailed below.

## 4.4. Results

---

### 2114 Primary visual cortex

2115 We found a transient increase in both the average and variance of the number of active neu-  
2116 rons at stimulus onset, followed by a fall to pre-stimulus levels, followed by another transient  
2117 increase (see figure 4.3). The oscillation in both of these measurements appear to reflect the  
2118 frequency of the stimulus (see Data section 4.2.1), and it is known that stimulus structure can  
2119 influence response structure(Litwin-Kumar, Chacron, and Doiron, 2012). We see a similar  
2120 but lower amplitude oscillation at the end of the stimulus presentation.

### 2121 Hippocampus

2122 In the hippocampus we observed a transient increase in the average number of active neurons  
2123 and in the variance of the number of active neurons at stimulus onset (see figure 4.4). The  
2124 increase lasted about 125ms, and the subsequent fall to baseline took the a similar amount of  
2125 time.

### 2126 Thalamus

2127 In the thalamus we observed a transient increase in the both the average and variance of  
2128 the number of active neurons on stimulus onset, followed by a fall to pre-stimulus levels,  
2129 followed by a sustained increase until the stimulus presentation ends.

2130 As one you might expect for a visual stimulus, the change in the average number of active  
2131 neurons was greatest in the primary visual cortex. In this region, this quantity doubled on  
2132 stimulus onset. In contrast, in the hippocampus and the thalamus, the average number of  
2133 active neurons only increased by a fraction of the unstimulated baseline value. The duration  
2134 of the response in V1 and the hippocampus at stimulus onset was 300 – 400ms, but the  
2135 response in the thalamus appeared to last for the duration of stimulus presentation. The V1  
2136 also showed a change in the average number of active neurons at stimulus end. The change  
2137 was similar to that observed at stimulus onset, but smaller in magnitude (see figures 4.3, 4.4,  
2138 and 4.5)

### 2139 4.4.2 Conway-Maxwell-binomial distribution is usually a better fit than bino- 2140 mial or beta-binomial

2141 Since the Conway-Maxwell-binomial distribution has not been fitted to neuronal data before,  
2142 it is not clear that it would be a better fit than the binomial or beta-binomial distributions.  
2143 In order to find out which parametric distribution was the best fit for the largest proportion

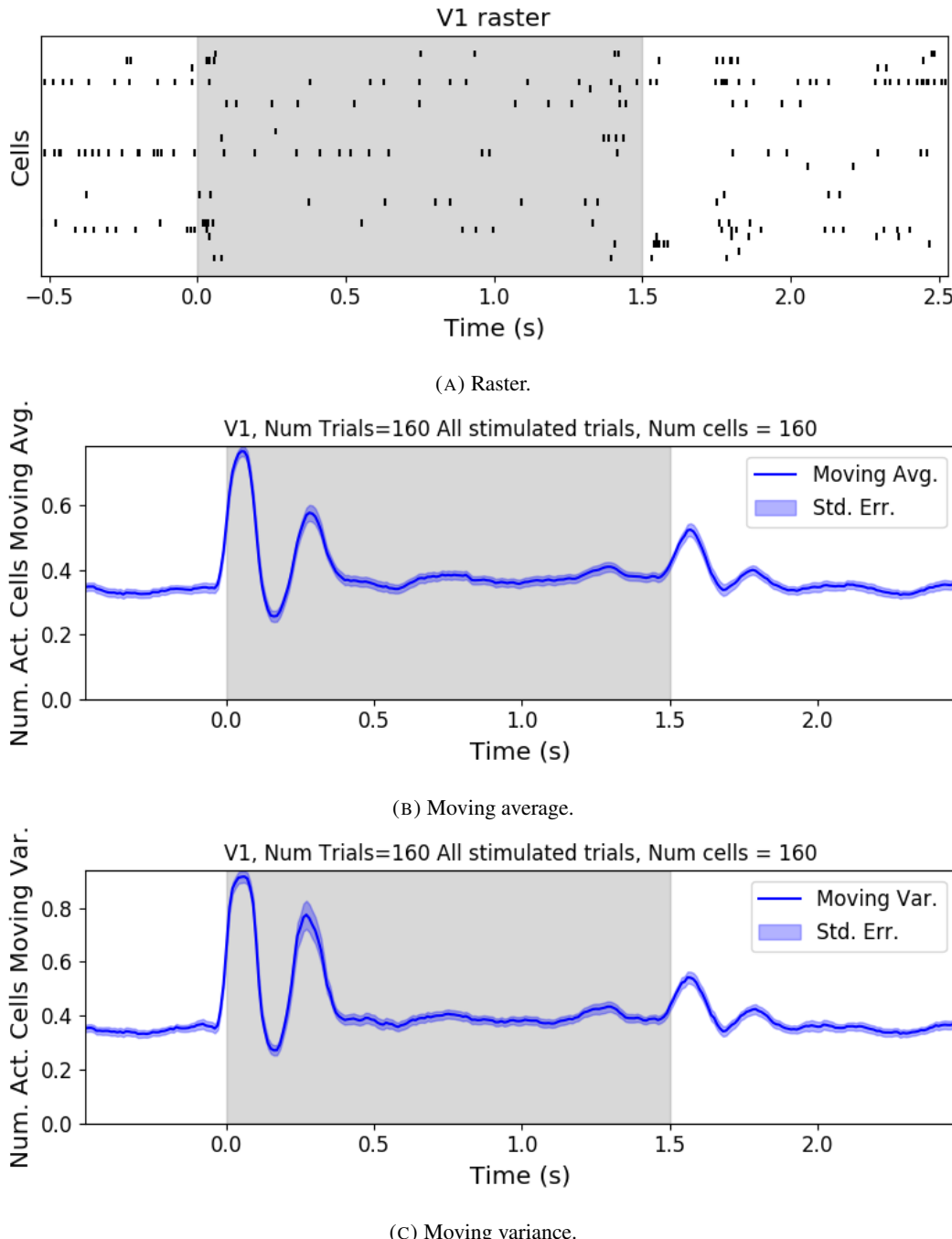


FIGURE 4.3: (A) Raster plot showing the spikes fired by 33 randomly chosen neurons in the primary visual cortex. (B-C) (B) average and (C) variance of the number of active neurons, measured using a sliding window 100ms wide, split into 100 bins. The midpoint of the time interval for each window is used as the timepoint (x-axis point) for the measurements using that window. The grey shaded area indicates the presence of a visual stimulus. The opaque line is an average across the 160 trials that included a visual stimulus of any kind. We can see a transient increase in the average number of active neurons and the variance of this number, followed by a fluctuation and another increase.

#### 4.4. Results

---

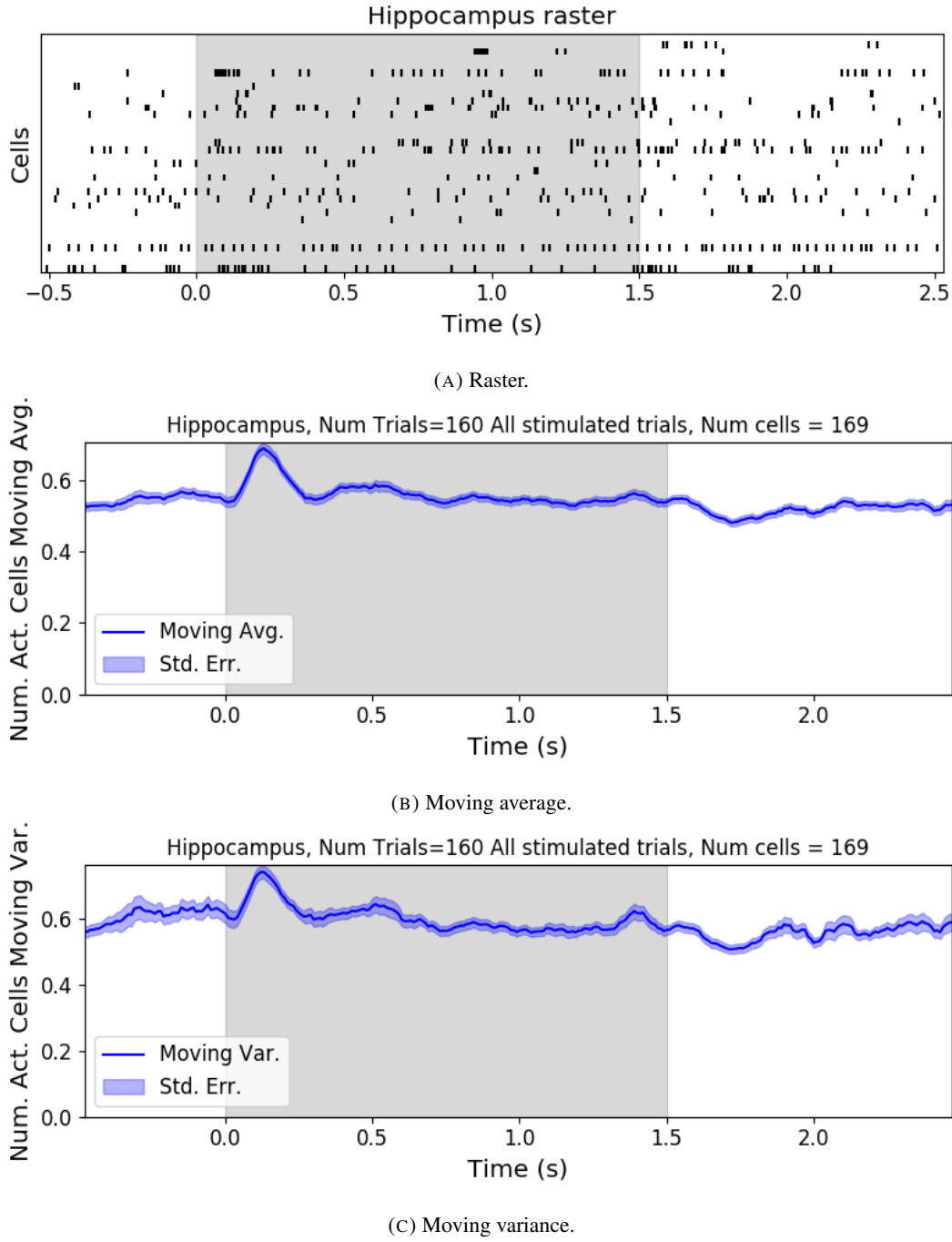


FIGURE 4.4: (A) Raster plot showing the spikes fired by 33 randomly chosen neurons in the hippocampus. (B-C) (B) average and (C) variance of the number of active neurons, measured using a sliding window 100ms wide, split into 100 bins. The midpoint of the time interval for each window is used as the timepoint (x-axis point) for the measurements using that window. The grey shaded area indicates the presence of a visual stimulus. The opaque line is an average across the 160 trials that included a visual stimulus of any kind. We can see a transient increase in the average number of active neurons and the variance of this number at stimulus onset.

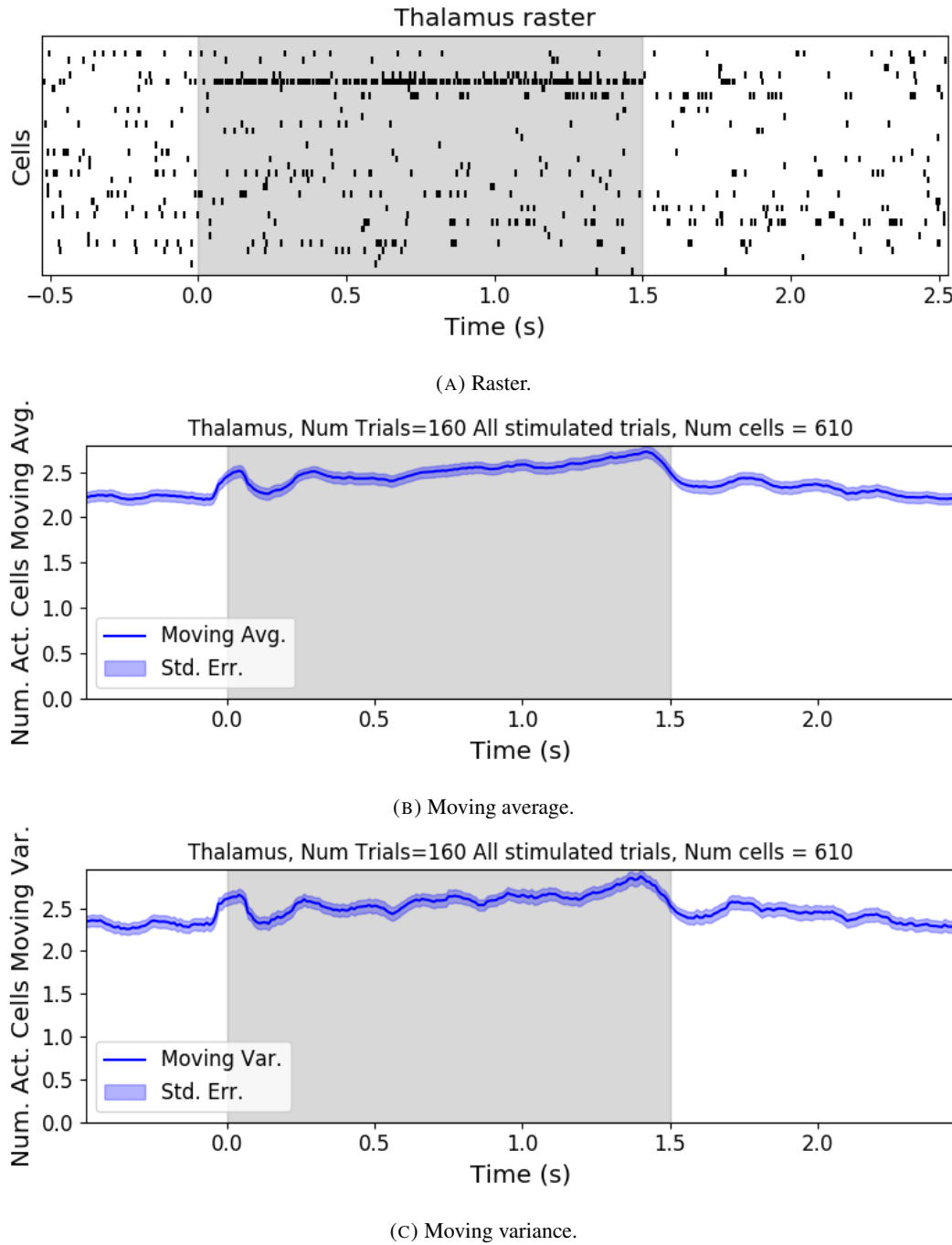


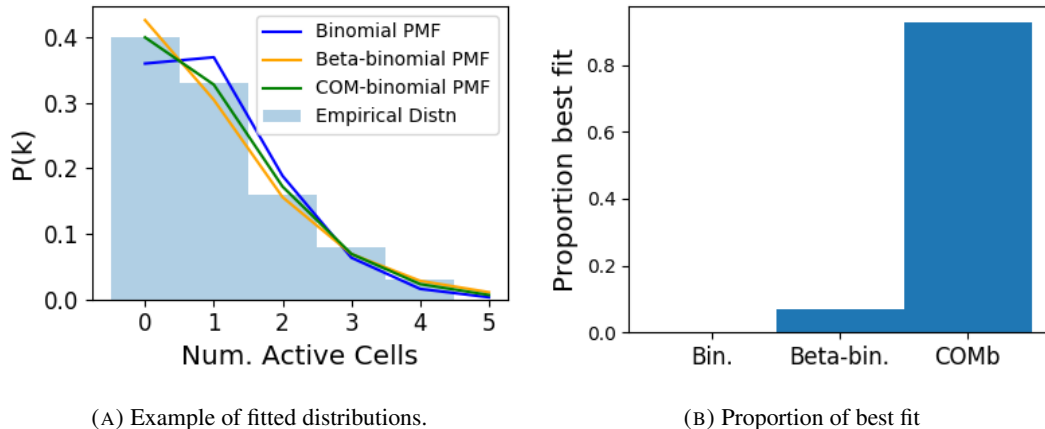
FIGURE 4.5: (A) Raster plot showing the spikes fired by 33 randomly chosen neurons in the thalamus. (B-C) (B) average and (C) variance of the number of active neurons, measured using a sliding window 100ms wide, split into 100 bins. The midpoint of the time interval for each window is used as the timepoint (x-axis point) for the measurements using that window. The grey shaded area indicates the presence of a visual stimulus. The opaque line is an average across the 160 trials that included a visual stimulus of any kind. We can see an immediate increase at stimulus onset, a subsequent fall, and another sustained increased until the stimulus presentation ends.

#### 4.4. Results

---

of our data, we fit a binomial, a beta-binomial, and a Conway-Maxwell-binomial (COMb) distribution to each window for each bin width, and each region. Then we assessed the goodness-of-fit of each distribution by calculating the log-likelihood of each fitted distribution using the associated sample. We measured the proportion of samples for which each distribution was the best fit, for each bin width value and each region.

We found that the COMb distribution was the best fit for most of the samples regardless of bin width or region. The bin width had an effect on the number of samples for which the COMb distribution was the best fit. The results are summarised in table 4.3. For a bin width of 1ms, the COMb distribution was the best fit for over 90% of samples, the beta-binomial distribution was the best fit for less than 10% of samples, and the binomial distribution was the best fit for less than 1% of samples, across regions. For 5ms bins, the COMb distribution was the best fit for 70 – 80% of samples, the beta-binomial distribution was the best fit for 20 – 30% of the samples, and again the binomial distribution was the best fit for less than 1% of samples, across regions. Finally, for 10ms bins, the COMb distribution was the best fit for 53 – 80% of samples, the beta-binomial distribution was the best fit for 20 – 47% of the samples, and the binomial distribution was the best fit for less than 0.1% of samples, across regions.



(A) Example of fitted distributions.

(B) Proportion of best fit

FIGURE 4.6: (A) An example of the binomial, beta-binomial, and Conway-Maxwell-binomial distributions fitted to a sample of neural activity. The Conway-Maxwell-binomial distribution is the best fit in this case. The histogram shows the empirical distribution of the sample. The probability mass function of each distribution is indicated by a different coloured line. (B) Across all samples in all trials, the proportion of samples for which each fitted distribution was the best fit. The Conway-Maxwell-binomial distribution was the best fit for 93% of the samples taken from V1 using a bin width of 1ms.

| Bin Width (ms) | Binomial | Beta-binomial | COMb     |
|----------------|----------|---------------|----------|
| 1ms            | < 1%     | < 10%         | > 90%    |
| 5ms            | < 0.1%   | 20 – 30%      | 70 – 80% |
| 10ms           | < 0.1%   | 20 – 47%      | 53 – 80% |

TABLE 4.3: Proportion of samples for which each distribution was the best fit, grouped by bin width. The COMb distribution is the best fit most of the time.

2161 **4.4.3 Conway-Maxwell-binomial distribution captures changes in association  
2162 at stimulus onset**

2163 We fit a Conway-Maxwell-binomial (COMb) distribution to the number of active neurons in  
2164 the 1ms time bins in a 100ms sliding window. We also measured the correlation coefficient  
2165 between the spike counts of all possible pairs of neurons, and took the average of these  
2166 coefficients. We did this for all the trials with a visual stimulus. We observed a reduction in  
2167 the COMb distribution's  $\nu$  parameter at stimulus onset from around 1 to between 0 and 1 (see  
2168 figure 4.7a). A value of  $\nu$  less than 1 indicates positive association between the neurons (see  
2169 section 4.3.5). We might expect to see this positive association reflected in the correlation  
2170 coefficients, but this is not the case. We see no change in the time series of average correlation  
2171 measures at stimulus onset.

2172 This may be due to the very short time bin we used in this case. We know that using small  
2173 time bins can artificially reduce correlation measurements (Cohen and Kohn, 2011). In this  
2174 case, fitting the COMb distribution may be a useful way to measure association in a neuronal  
2175 ensemble over very short timescales (< 10ms).

2176 **4.4.4 Replicating stimulus related quenching of neural variability**

2177 Churchland et al. (2010) inspected the effect of a stimulus on neural variability. One of the  
2178 measures of neural variability that they employed was the Fano factor of the spike counts of  
2179 individual cells (see section 4.3.4). They found a reduction in neural variability as measured  
2180 by the Fano factor in various cortical areas in a macaque at the onset of various visual stimuli,  
2181 or a juice reward (Churchland et al., 2010).

2182 We measured the Fano factor of the spike count of each cell in each brain region, during  
2183 each trial. We measured the mean and standard error of these Fano factors from 500ms  
2184 before stimulus onset until 1000ms after stimulus end. For the primary visual cortex, we  
2185 found a transient reduction in the Fano factor immediately after stimulus onset. We used  
2186 a Mann-Whitney U test to check that the Fano factors measured in a window starting at

#### 4.4. Results

---

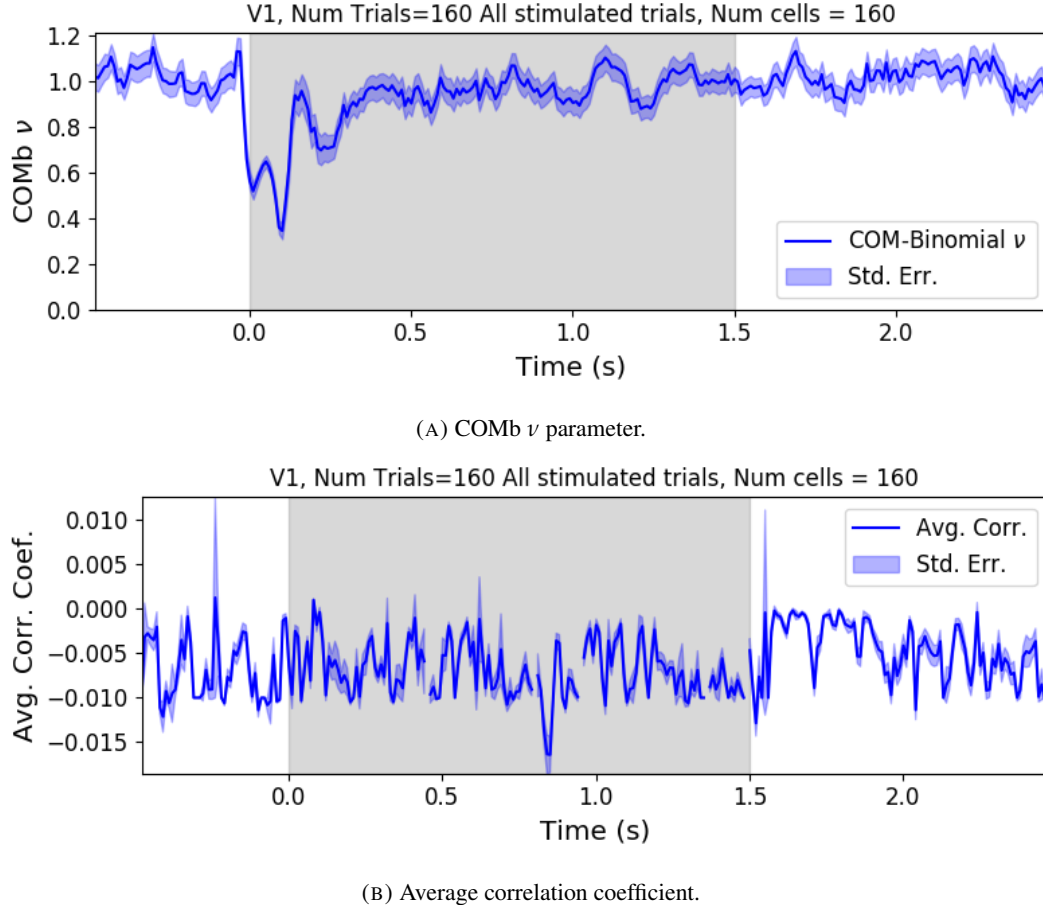


FIGURE 4.7: (A) We fit a Conway-Maxwell-binomial distribution to the number of active neurons in 1ms time bins of a 100ms sliding window. We did this for all trials with a visual stimulus and took the average across those trials. We see a transient drop in value for the distribution's  $\nu$  parameter at stimulus onset. This shows an increase in positive association between the neurons. (B) We measured the correlation coefficient between the spike counts of all possible pairs of neurons in the same sliding window. The took the average of those coefficients. We also did this for every visually stimulated trial, and took the average across trials. The increase in positive association is not reflected with an increase in average correlation.

stimulus onset and ending 100ms later were significantly lower than the factors measured in a window ending at stimulus onset ( $p < 0.001$ , see figure 4.8a). We did not get this statistically significant result in any other region.

Our findings agree with those of Churchland et al. for the primary visual cortex. However Churchland also found a reduction in the Fano factor in the dorsal premotor cortex (PMd) at stimulus onset. Our measurements from the mouse motor cortex show no change at stimulus onset (see figure 4.8b). This could indicate some difference in the functionality of the motor cortex in a macaque and the motor cortex of a mouse.

Similar to these findings in the Fano factor, we found a reduction in the  $\nu$  parameter of the COMB distribution on stimulus onset in V1 (figure 4.7a) and in no other region from

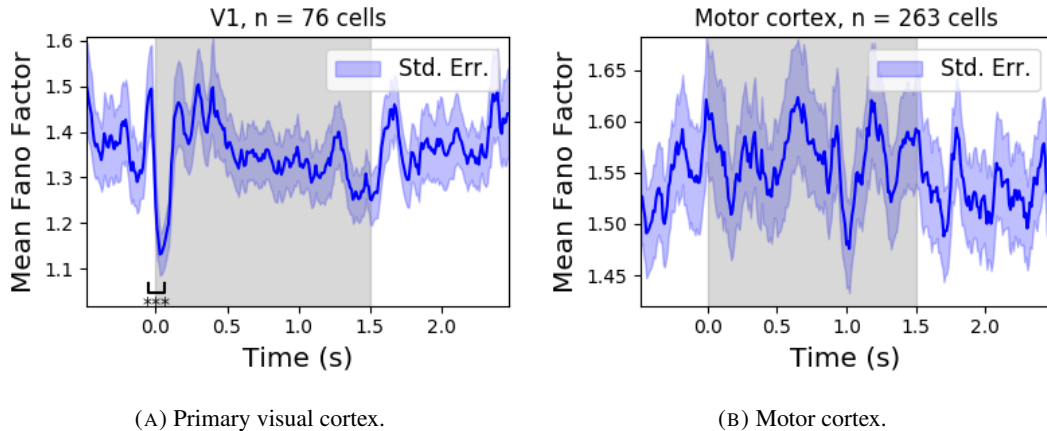


FIGURE 4.8: (A) The mean Fano factor of the spike counts of the cells in the primary visual cortex. Means were taken across cells first, then across trials. There was a significant decrease in the Fano factors immediately after stimulus onset. (B) The mean Fano factor of the spike counts of the cells in the motor cortex. No significant change in measurements at any point.

2197 which we had data. Specifically, the  $\nu$  parameter reduced from around 1, to between 1 and 0.  
 2198 This represents a change from no association between the neurons, to a positive association.  
 2199 It is possible that this positive association may be responsible for the reduction in the Fano  
 2200 factor.

## 2201 4.5 Discussion

2202 Our aim in this research was to develop a new statistical method for analysing the activity  
 2203 of a neuronal ensemble at very short timescales. We wanted our method to use information  
 2204 taken from the whole ensemble, but we also wanted the method to be quick and easy to  
 2205 implement. It is likely that analysis methods with these characteristics will become valuable  
 2206 as electrophysiological datasets include readings from more cells over longer time periods. In  
 2207 this case, we used the number of active, or spiking, neurons in a very short time bin ( $< 10\text{ms}$ )  
 2208 as a measure of ensemble activity.

2209 First of all, we showed that there were changes in response that we could model at these  
 2210 very short time scales in some of the brain regions from which we had recordings. We ob-  
 2211 served changes in the average number of active neurons, and the variance of the number of  
 2212 active neurons in three different brain regions in response to visual stimuli. Since we know  
 2213 that correlated behaviour is associated with sensory perception (deCharms and Merzenich,  
 2214 1996), we might hope to measure the pairwise correlations within the neuronal population  
 2215 in order to further investigate these responses. But, using such short time bins can produce

#### 4.5. Discussion

---

artificially small spike count correlation measurements (Cohen and Maunsell, 2009). Overcoming this limitation was one of our objectives for our new method. In order to do this, we abandoned the idea of measuring the correlations directly and embraced the concept of *association*. In order to quantify the association between neurons, we used the Conway-Maxwell-binomial distribution to model the number of active (spiking) neurons in an ensemble as a sum of possibly associated Bernoulli random variables.

We showed that the Conway-Maxwell-binomial distribution performed better than the more common options of the binomial and beta-binomial distributions. Furthermore, we showed that the positively associated behaviour between neurons in the primary visual cortex could be captured by fitting a Conway-Maxwell-binomial distribution, but was not captured by the more standard approach of measuring the spike count correlation. The associated behaviour could not be measured using spike count correlations, because of the very short bins required to capture short timescale behaviour.

We replicated a famous result from Churchland et al (2010) relating to the quenching of neural variability in cortical areas at stimulus onset, and in doing so, we established a correspondence between the association quantifying parameter of the Conway-Maxwell-binomial (COMb) distribution and the neural variability as measured by the Fano factor. We found a reduction in the  $\nu$  parameter of the COMB distribution at stimulus onset, indicating a change from no association to positive association between neurons in V1. We found a corresponding reduction in the Fano factor of the individual cells in V1. The positive association between neurons induced by the stimulus would constrain the neurons to fire at the same time. The stimulus also induced a larger number of neurons to spike. These two actions combined could cause an increase in the firing rate of individual cells that is greater in magnitude than the increase in firing rate variability. If this is indeed the case, then the association as captured by the COMB distribution could be regarded as one of the ‘natural parameters’ of the ensemble response for short timescales. That is, a quantity that directly measures some aspect of the behaviour of the ensemble. In this case, it the correlated behaviour of the individual neurons is captured.

This work could be just a first step in creating analysis methods based on the Conway-Maxwell-binomial distribution, or similar statistical models. One way to extend the method would be to pair it up with the ‘Population Tracking model’ (O’Donnell et al., 2017). This model attempts to characterise the interaction between an ensemble and each member of the ensemble by quantifying the probability of spiking for a given a cell, given the number of active cells in the whole population. Combining this model with the COMB distribution

2250 would give us a model that could accurately fit the number of active neurons at any moment,  
2251 and that gives a probability of firing for each cell, and therefore probabilities for full spiking  
2252 patterns, without adding a huge number of parameters to fit.

2253 A more complex way to extend the model would be to fit a Conway-Maxwell-binomial  
2254 distribution to data recorded from multiple brain regions simultaneously, with a different fit  
2255 for each region, then to analyse the temporal relationship between the fitted parameters of  
2256 each region. If we analysed the time series of the COMB distribution parameters from the  
2257 different regions, looking at cross-correlations between regions, this may give some results  
2258 relating to the timescales in which information is processed in different brain regions.

2259 **Chapter 5**

2260 **Studies with practical limitations &**  
2261 **negative results**

2262 *Abstract*

2263 Here I will present some details on research topics that I started, but that unfortunately did not  
2264 lead anywhere useful. There are two pieces of research, based on two papers. Each paper is  
2265 related to the overall theme of my PhD of analysing and modelling behaviours of populations  
2266 of neurons. The first part is based on a model of parallel spike trains including higher order  
2267 interactions by Shimazaki et al (2012). The second part is based on a multiscale model for  
2268 making inferences on hierarchical data.

2269 **5.1 Dynamic state space model of pairwise and higher order neu-**  
2270 **ronal correlations**

2271 In their paper Shimazaki et al (2012) aimed to model spike trains from populations of neurons  
2272 in parallel, with pairwise and higher order dynamic interactions between the trains. They  
2273 modelled the spike trains as multi-variate binary processes using a log-linear model, and they  
2274 extracted spike interaction parameters using a Bayesian filter/EM-algorithm. They developed  
2275 a goodness-of-fit measure for the model to test if including these higher order correlations  
2276 is necessary for an accurate model. Their measure was based on the Bayes factor but they  
2277 also assessed the suitability of higher order models using the AIC and BIC. So the increase  
2278 in the number of parameters associated with fitting higher order interactions was taken into  
2279 account. They tested the performance of the model on synthetic data with known higher  
2280 order correlations. They used the model to look for higher order correlations in data from  
2281 awake behaving animals. They use the model to demonstrate dynamic appearance of higher  
2282 order correlations in the monkey motor cortex (Shimazaki et al., 2012).

2283 We used the available Python repository to implement the model, and we successfully  
2284 worked through the tutorial provided. But we found that the model did not scale well to  
2285 larger populations. We attempted to fit the model to a population of 10 neurons and found we  
2286 didn't manage to finish the process. Since, our goal was to find a model to scale to hundreds  
2287 or thousands of neurons, we decided that this model was no longer worth pursuing.

2288 **5.2 A multiscale model for hierarchical data applied to**  
2289 **neuronal data**

2290 In their paper Kolaczyk et al (2001) developed a framework for a modelling hierarchically  
2291 aggregated data, and making inferences based on a model arising from this framework. They  
2292 assumed that a hierarchical aggregation existed on the data in question, where each element at  
2293 each level of the hierarchy had some associated measurements, an associated mean process,  
2294 which was the expected value of these measurements. They also assumed that the measure-  
2295 ments of each parent were equal to the sum of the measurements from all of its children.  
2296 They showed that these assumptions gave rise to a relationship between parent and child  
2297 measurements across all levels of the hierarchy, where the product of the likelihood of the  
2298 parameters of the lowest level of the hierarchy can be expressed as products of conditional  
2299 likelihoods of the elements of higher levels of the hierarchy (Kolaczyk and Huang, 2010).

2300 They gave examples of these expressions for measurements sampled from Gaussian dis-  
2301 tributions, and Poisson distributions, and showed the definitions of the hierarchical param-  
2302 eters which reparametrise the distribution of these data taking the hierarchy into account.  
2303 They go on to suggest prior distributions for this multiscale model, and integrate these priors  
2304 to give posterior distributions for the measurements from each element at each level in the hi-  
2305 erarchy, and expressions for the MAP estimated parameters of each the associated processes  
2306 (Kolaczyk and Huang, 2010).

2307 We implemented their model in Python by creating some synthetic data from Poisson  
2308 distributions, and defining a hierarchy by agglomerating these data. We calculated the MAP  
2309 estimates using our knowledge of the hierarchy, and using the expressions given in the paper.  
2310 We found that the MAP estimates were far less accurate than would be achieved by simply  
2311 ignoring the hierarchy during estimation, and using a maximum likelihood approach. After  
2312 that, we decided to move on.



2313 **Chapter 6**

2314 **Discussion**

2315 In this project, we attempted to address some of the challenges in data collection from  
2316 large neuronal ensembles (specifically with calcium imaging) and some of the problems in  
2317 analysing the data collected from large neuronal ensembles.

2318 Firstly, we investigated the relationship between cell biochemistry, action potentials and  
2319 the fluorescence traces produced by fluorescent calcium indicators. We did this by building  
2320 a biophysical model that takes in a spike train and returns the fluorescence trace that that  
2321 spike would induce. The model included mechanics for the binding of calcium to fluorescent  
2322 and endogenous mobile and immobile buffers, and the consequent changes in concentration  
2323 of free and bounded calcium. The model consisted of 17 parameters, 13 of which were  
2324 set according to data from the literature, and 4 of which were free parameters. We trained  
2325 the model using simultaneously collected spiking and calcium imaging data (Berens et al.,  
2326 2018). We fitted the model by matching the  $\Delta F/F_0$  in response to an action potential, and  
2327 by matching the power spectrum of the actual fluorescence trace. This meant that our model  
2328 would include the correct amount of noise as well as return the correct change in amplitude  
2329 in response to an action potential.

2330 Since our model produced fluorescence traces, we could apply spike inference algorithms  
2331 to the modelled fluorescence traces that our model produced after training, and compare the  
2332 performance of the algorithms on the modelled traces to their performance on the real traces.  
2333 We used three spike inference algorithms, two of which were based on modelling the cal-  
2334 cium trace as an autoregression (Friedrich and Paninski, 2016; Pnevmatikakis et al., 2016),  
2335 and another inference algorithm that was a little more biologically inspired, but amounted to  
2336 a very similar algorithm (Deneux et al., 2016). We compared the performance of the algo-  
2337 rithms by using them to infer spikes from 20 real and modelled fluorescence traces induced  
2338 by 20 corresponding real spike trains. We then used several binary classification measures  
2339 (true positive rate, accuracy etc.) to asses the quality of the spike inference for the real and

2340 modelled fluorescence traces. We found that the spike inference algorithms performed sim-  
2341 ilarly on real and modelled traces, showing that our model is capturing at least some of the  
2342 characteristics of the real fluorescence traces.

2343 In order to investigate the effect of indicator characteristics on the modelled fluorescence  
2344 trace and spike inference quality, we perturbed the indicator's affinity and dissociation rate  
2345 in parallel, keeping the ratio of the two the same for all perturbations. We measured the SNR  
2346 of the trace, and the true positive rate of the spike inference algorithms at each perturbed  
2347 value pair. We found that perturbing the values lower caused in decrease in SNR and spike  
2348 inference quality. This shows that our model could be used to test theoretical fluorescent cal-  
2349 cium indicators without having to actually manufacture them. Experimental neuroscientists  
2350 could also use our model to judge which indicator characteristics are most influential in their  
2351 experimental context.

2352 We then investigated the effect of perturbing buffer concentration, and indicator concen-  
2353 tration, on the signal-to-noise ratio of the modelled fluorescence trace and spike inference  
2354 quality. This was a worthwhile experiment because endogenous buffer concentrations vary  
2355 from cell to cell (Bartol et al., 2015; Maravall et al., 2000; Neher and Augustine, 1992), as  
2356 does indicator expression (Chen et al., 2013). We found that extreme perturbations away  
2357 from the indicator concentration taken from the literature lowered the SNR of the trace, and  
2358 the spike inference quality. We also found that increases in the concentration of endogenous  
2359 buffer above the value taken from the literature caused a decrease in the SNR and spike infer-  
2360 ence quality. This reiterates that the indicator and endogenous buffers compete to bind with  
2361 free calcium molecules, and this has an effect on fluorescence and consequently on spike  
2362 inference.

2363 We then created some synthetic spike trains with controlled mean firing rates sampled  
2364 the rates from an Ornstein-Uhlenbeck process. We found that the higher the firing rate, the  
2365 lower the accuracy of the spike inference algorithms. But the mean firing could perhaps be  
2366 inferred from the amplitude of the fluorescence traces. The higher firing rate, the higher the  
2367 amplitude. Calibrating the model to facilitate and accurate measurement would require some  
2368 kind of ground truth, but relative comparisons could be made without any other knowledge  
2369 of the underlying spiking process.

2370 One obvious limitation to our model is the lack of binding mechanics for both the indi-  
2371 cator and endogenous buffers. Greenberg et al included these mechanics in their successful  
2372 spike inference model. We felt that the timescale of these binding mechanics was so small in  
2373 comparison to the fluorescence dynamics that omitting them would make no difference. But

2374 it is possible that their inclusion would improve our model.

2375 After investigating the difficulties with inferring spiking data from calcium imaging data,  
2376 we moved from data collection to analysis and we decided to implement a new network anal-  
2377 ysis method on data from a neuronal ensemble. Using an electrophysiological dataset with  
2378 spike sorted data from 9 different brain regions in 3 mice (Steinmetz, Carandini, and Harris,  
2379 2019), we binned the spike times for each cell into spike counts for each cell and measured  
2380 the correlation coefficients between these spike counts for a selection of cells evenly dis-  
2381 tributed across the 9 regions. We repeated these measurements for time bin widths ranging  
2382 from 5ms to 3s. We rectified these measurements and, for a given time bin width, used them  
2383 as weights for a weighted undirected graph where each node represents a neuron, and the  
2384 weight of each edge is the correlation between the neurons represented by the nodes on that  
2385 edge. We applied a novel spectral analysis and community detection method (Humphries  
2386 et al., 2019) to this network. This clustered the nodes in our ensemble into communities  
2387 whose behaviour was more correlated than expected. Our measure of 'expected correlation  
2388 strength' were based on a random network that matched our data network's sparsity and total  
2389 weight. We compared the detected communities to the anatomical division of our cells using  
2390 clustering comparison measures. We then conditioned the binned spike counts on the be-  
2391 haviour of the mouse using the principal components of a video of the mouses face recorded  
2392 simultaneously with the electrophysiology. We broke the total covariance down into 'spike  
2393 count covariance' and 'signal covariance' components conditioning on the behavioural data  
2394 and using the law of total covariance. We then repeated our analysis for spike count corre-  
2395 lations, and signal correlation. Finally, since our community detection method was only valid  
2396 on graphs with non-negative weights, we used different methods for creating a non-negative  
2397 graph from our total correlations, and we repeated our analysis on those graphs.

2398 Our first finding was that the time bin width used to bin spike times into spike counts had  
2399 a effect on the mean magnitude of the correlations measured. The wider the bin, the higher  
2400 the correlations. Not only that, we separated the pairs into positively and negative correlated  
2401 pairs, and we found that positively correlated pairs have greater correlation coefficients when  
2402 using a wider bin, and negatively correlated pairs have more negative correlation coefficients  
2403 when using a wider bin. We also found that the width of the bin used had an effect on the  
2404 distribution of the spike counts. For smaller bin widths, the distribution of spike counts was  
2405 better represented by a skewed distribution like the Poisson distribution. For wider bins, the  
2406 spike counts were better represented by a Gaussian distribution.

2407 Next we investigated the differences between correlations within regions and between

regions. When we divided the pairs according to those two groups, we found that the mean within-region correlations were higher at every bin width, and the difference between the two means grew with increasing bin width. When we split the pairs of cells according to their regions, we found that the mean within-region correlations in any given region were usually greater than the mean between-region correlations for any region pair involving that region. The difference between the mean within-region correlation and the highest between-region correlations involving that region grew smaller with increasing bin width. To investigate this further, we plotted these mean correlations in matrices. Although the mean within-region correlations were usually the highest value in their row or column, as the bin width increased, the mean between-region correlations grew in magnitude relative to the within-region figure.

Next we chose a null network model, and we used the ‘Network Noise Rejection’ process (Humphries et al., 2019) to check for additional structure in our correlation based data network that was not captured by the null model. We found additional structure for any bin width that we used. We also found that the dimensionality of the additional structure reduced as we increased the bin width. This could mean that the processes or representations that take place over longer timescales within the brain also take place in a lower dimensional space.

We applied a community detection method (Humphries, 2011) to the signal correlation networks arising from the network noise rejection. We found that the number of communities detected decreased with increasing bin width. We also noticed that at shorter bin widths, the detected communities were more likely to consist of cells from one brain region only. We investigated this further by using clustering comparison methods to compare the detected communities with the anatomical division of the cells. We found that for short timescales  $< 50\text{ms}$  correlated communities tended to exist within anatomical regions, and for longer timescales  $> 100\text{ms}$ , the correlated communities tended to exist across anatomical regions. This is broadly in agreement with a similar finding for EEG data from humans performing semantic or memory tasks (Stein and Sarnthein, 2000). Von Stein et al. (2000) found that visual processing taking place locally in the visual system was captured in the gamma frequency range (25 – 70Hz), while semantic processing was captured in the beta range (12 – 18Hz), and tasks involving mental imagery and working memory retention were captured in the theta and alpha ranges (4 – 8Hz, and 8 – 12Hz respectively).

We then conditioned our correlation measures on the the mouse’s behaviour. This allowed us to create spike count correlation (or noise correlation) networks, and signal correlation networks (Cohen and Kohn, 2011). We applied our analysis to these networks. For the

spike count correlation networks we found very similar results to the total correlation networks. More communities at smaller bin widths, and communities resembled the anatomical division at smaller bin widths. Given that recent findings show that behaviour can account for correlated spiking in many areas of the brain (Stringer et al., 2019), these results for the spike count correlation show that this correlated behaviour is still processed locally at short timescales, while processes and representations that take more time make use of correlated activity across multiple regions.

For the signal correlations, we still found additional structure in these networks. But we always detected a smaller number of communities. These communities also had no relation to the anatomical division of the cells. This result shows that there are groups of cells across multiple brain regions that are activated similarly by certain behaviours.

All of the networks so far were based on rectified correlation measures, because the network noise rejection and community detection processing is (currently) only valid for networks with non-negative weights. For the final part of our analysis, we tried different ways of transforming our total correlations into non-negative quantities before applying our analysis. First of all we took the absolute value of our correlation measures. Our results were very similar to those for the rectified correlations with the exception that we detected more communities consistently. It is possible that using this method detects both positively and negatively correlated communities.

We also tried reversing the sign of all the correlations, then rectifying the network. We hope that this would allow us to detect the negatively correlated communities. We did detect communities in these networks, but never more than three, and these communities bore no relationship with the anatomical distribution of the cells.

There is a lot of potential for network science applications in computational neuroscience. For example, some pairwise measure other than correlation coefficients could be used as the weights of the graph. A directed measure like synaptic connectivity could be used as the basis for directed graphs. The analysis methods applicable to directed graphs could give insights about the formation of synaptic connections, or the dynamic changes in these connections over time. Other methods of community detection could be used on directed or undirected graphs. We used a ‘hard’ clustering method in our research, that is, each neuron could be a member of one cluster/community only. ‘Fuzzy-clustering’ methods do exist, where each element of the set to be clustered could be a member of more than one cluster (Baadel, Thabtah, and Lu, 2016).

Having spent much time investigating correlated behaviour using coefficients of spike

counts, we decided to try another method for capturing correlated behaviour in neuronal ensembles. We used electrophysiological data taken from 5 brain regions of an awake mouse exposed to visual stimuli (Steinmetz et al., 2019). We modelled the number of active neurons in a given brain region as the number of successes in a collection of dependent Bernoulli random variables using the Conway-Maxwell-binomial distribution. To avoid violating the Bernoulli assumption, we binned the spike times using 1ms bins. The Conway-Maxwell-binomial distribution is a two parameter extension of the standard binomial distribution. The extra parameter allows the distribution to capture possible positive or negative association between the Bernoulli trials (Kadane, 2016). This means that we are assuming that all the neurons are dependent in the same way. This is not an accurate assumption, but it allows us model the data in a simple way.

First of all we established that there were changes in the number of active neurons in response to the visual stimuli. This was the case in the hippocampus, thalamus, and primary visual cortex. Each region had its own signature response. We measured the mean and variance of the number of active neurons in a sliding window starting before stimulus onset, and finishing after the end of stimulus presentation.

As well as the Conway-Maxwell-binomial distribution, we also fitted binomial, and beta-binomial distributions to the number of active neurons in a sliding window. We found that the Conway-Maxwell-binomial distribution was the best fit for over 90% of the samples. This means that the COMb distribution is capturing some dependency between the neurons, because the binomial distribution assumes independence. Also the COMb distribution captures this dependence more accurately than the beta-binomial distribution, which does have some capacity for over dispersion.

Next we showed that the Conway-Maxwell-binomial distribution captured the change in association at stimulus onset better than the correlation coefficient. The extremely small bin width artificially shrunk the correlation coefficient to the point where this measurement didn't detect any correlated activity. But the association parameter of the COMb distribution detected some positive association between the neurons at stimulus onset. So, for particularly short time bins, where neurons can be treated as Bernoulli random variables, the Conway-Maxwell-binomial distribution is a good way to capture correlated behaviour. There are other measurements for capturing association to which this distribution should be compared. Cross-correlograms could be used for some measure of synchrony, for example.

Finally, we replicated a famous finding of Churchland et al. (2010) relating to the quenching of neural variability at stimulus onset, thereby finding a parallel between this reduction

2509 in the Fano factor and a reduction in the association parameter of the COMb distribution.

2510 We showed that computational neuroscientists can make progress by being inventive with  
2511 their statistical models. A similar distribution to investigate would be the Conway-Maxwell-  
2512 Poisson distribution. This is similar to the standard Poisson distribution, but with an addi-  
2513 tional parameter that allows for over- or under- dispersion relative to a Poisson distribution.  
2514 This might be ideal for modelling firing rates of individual neurons. Some interaction be-  
2515 tween the fitted parameters could capture the association between neurons.

2516 There is one technology that has the potential to take over from both electrophysiology  
2517 and calcium imaging. The technique of voltage imaging has become more useful in recent  
2518 years. The aim for neuroscience would be to develop a voltage imaging dye or protein that  
2519 images the membrane potential of a neuron with enough spatial and temporal resolution to  
2520 detect action potentials. Genetically encoded voltage indicators have been developed, and  
2521 enable targeting of specific neuronal ensembles. But their spatial resolution is not yet high  
2522 enough to single out individual cells (Bando et al., 2019). These indicators have the potential  
2523 to take over from calcium imaging, and if imaging deep within the brain becomes possible,  
2524 electrophysiology could also be replaced. This is speculation, but the potential is there.



# 2525 Bibliography

- 2526 Allen, William E. et al. (2019). “Thirst regulates motivated behavior through modulation of  
2527 brainwide neural population dynamics”. In: *Science* 364.6437.
- 2528 Baadel, S., F. Thabtah, and J. Lu (2016). “Overlapping clustering: A review”. In: *2016 SAI  
2529 Computing Conference (SAI)*, pp. 233–237.
- 2530 Baldassano, Christopher et al. (2017). “Discovering Event Structure in Continuous Narrative  
2531 Perception and Memory”. In: *Neuron* 95.3, 709 –721.e5.
- 2532 Bando, Yuki et al. (2019). “Genetic voltage indicators”. In: *BMC Biology* 17.1, p. 71.
- 2533 Bartol, Thomas M. et al. (2015). “Computational reconstitution of spine calcium transients  
2534 from individual proteins”. In: *Frontiers in Synaptic Neuroscience* 7, p. 17.
- 2535 Berens, Philipp et al. (May 2018). “Community-based benchmarking improves spike rate in-  
2536 ference from two-photon calcium imaging data”. In: *PLOS Computational Biology* 14.5,  
2537 pp. 1–13.
- 2538 Bezanson, Jeff et al. (Sept. 2012). “Julia: A Fast Dynamic Language for Technical Comput-  
2539 ing”. In: *MIT*.
- 2540 Buccino, Alessio P. et al. (2019). “SpikeInterface, a unified framework for spike sorting”. In:  
2541 *bioRxiv*.
- 2542 Chen, Tsai-Wen et al. (July 2013). “Ultrasensitive fluorescent proteins for imaging neuronal  
2543 activity”. In: *Nature* 499, 295–300.
- 2544 Churchland, Mark M. et al. (2010). “Stimulus onset quenches neural variability: a widespread  
2545 cortical phenomenon”. eng. In: *Nature neuroscience* 13.3. 20173745[pmid], pp. 369–378.
- 2546 Cohen, Marlene R. and Adam Kohn (2011). “Measuring and interpreting neuronal corre-  
2547 lations”. In: *Nature Neuroscience* 14.7, pp. 811–819.
- 2548 Cohen, Marlene R. and John H. R. Maunsell (2009). “Attention improves performance pri-  
2549 marily by reducing interneuronal correlations”. eng. In: *Nature neuroscience* 12.12. 19915566[pmid],  
2550 pp. 1594–1600.
- 2551 Dana, Hod et al. (Sept. 2014). “Thy1-GCaMP6 Transgenic Mice for Neuronal Population  
2552 Imaging In Vivo”. In: *PloS one* 9, e108697.

- 2553 deCharms, R. Christopher and Michael M. Merzenich (1996). “Primary cortical representation of sounds by the coordination of action-potential timing”. In: *Nature* 381.6583,  
2554 pp. 610–613.
- 2556 Deneux, Thomas et al. (July 2016). “Accurate spike estimation from noisy calcium signals  
2557 for ultrafast three-dimensional imaging of large neuronal populations in vivo”. In: *Nature  
2558 Communications* 7.1.
- 2559 Dombeck, Daniel A. et al. (2010). “Functional imaging of hippocampal place cells at cellular  
2560 resolution during virtual navigation”. In: *Nature Neuroscience* 13.11, pp. 1433–1440.
- 2561 Éltes, Tímea et al. (2019). “Improved spike inference accuracy by estimating the peak am-  
2562 plitude of unitary [Ca<sub>2+</sub>] transients in weakly GCaMP6f-expressing hippocampal pyra-  
2563 midal cells”. In: *The Journal of Physiology* 597.11, pp. 2925–2947.
- 2564 Faas, Guido C. et al. (2011). “Calmodulin as a direct detector of Ca<sub>2+</sub> signals”. In: *Nature  
2565 Neuroscience* 14.3, pp. 301–304.
- 2566 Fiala, John C. and Kristen M. Harris (1999). *Dendrite Structure*.
- 2567 Flach, Boris (Sept. 2013). “A Class of Random Fields on Complete Graphs with Tractable  
2568 Partition Function”. In: *IEEE transactions on pattern analysis and machine intelligence*  
2569 35, pp. 2304–6.
- 2570 Forney, G. D. (1973). “The viterbi algorithm”. In: *Proceedings of the IEEE* 61.3, pp. 268–  
2571 278.
- 2572 Fosdick, Bailey et al. (Aug. 2016). “Configuring Random Graph Models with Fixed Degree  
2573 Sequences”. In: *SIAM Review* 60.
- 2574 Friedrich, Johannes and Liam Paninski (2016). “Fast Active Set Methods for Online Spike In-  
2575 ference from Calcium Imaging”. In: *Advances in Neural Information Processing Systems*  
2576 29. Ed. by D. D. Lee et al. Curran Associates, Inc., pp. 1984–1992.
- 2577 Ganmor, Elad, Ronen Segev, and Elad Schneidman (2011). “Sparse low-order interaction  
2578 network underlies a highly correlated and learnable neural population code”. In: *Pro-  
2579 ceedings of the National Academy of Sciences* 108.23, pp. 9679–9684.
- 2580 Girard, P., J. M. Hupé, and J. Bullier (2001). “Feedforward and Feedback Connections Be-  
2581 tween Areas V1 and V2 of the Monkey Have Similar Rapid Conduction Velocities”. In:  
2582 *Journal of Neurophysiology* 85.3. PMID: 11248002, pp. 1328–1331.
- 2583 Greenberg, David et al. (Nov. 2018). “Accurate action potential inference from a calcium  
2584 sensor protein through biophysical modeling:” in:
- 2585 Gründemann, Jan et al. (2019). “Amygdala ensembles encode behavioral states”. In: *Science*  
2586 364.6437.

## Bibliography

---

- 2587 Hodgkin, A. L. and A. F. Huxley (1939). “Action Potentials Recorded from Inside a Nerve  
2588 Fibre”. In: *Nature* 144.3651, pp. 710–711.
- 2589 Humphries, Mark et al. (Jan. 2019). “Spectral rejection for testing hypotheses of structure in  
2590 networks”. In:
- 2591 Humphries, Mark D. (2011). “Spike-Train Communities: Finding Groups of Similar Spike  
2592 Trains”. In: *Journal of Neuroscience* 31.6, pp. 2321–2336.
- 2593 Jun, James J. et al. (2017). “Fully integrated silicon probes for high-density recording of  
2594 neural activity”. In: *Nature* 551.7679, pp. 232–236.
- 2595 Kadane, Joseph B. (June 2016). “Sums of Possibly Associated Bernoulli Variables: The  
2596 Conway–Maxwell-Binomial Distribution”. In: *Bayesian Anal.* 11.2, pp. 403–420.
- 2597 Kilhoffer, Marie-Claude et al. (Sept. 1992). “Use of Engineered Proteins With Internal Tryp-  
2598 tophean Reporter Groups and Perturbation Techniques to Probe the Mechanism of Ligand-  
2599 Protein Interactions: Investigation of the Mechanism of Calcium Binding to Calmodulin”.  
2600 In: *Biochemistry* 31.34, pp. 8098–8106.
- 2601 Koch, Christoff (1999). *Biophysics of Computation: Information Processing in Single Neu-*  
2602 *rons*. Oxford University Press.
- 2603 Kolaczyk, Eric and Haiying Huang (Sept. 2010). “Multiscale Statistical Models for Hierar-  
2604 chical Spatial Aggregation”. In: *Geographical Analysis* 33, pp. 95 –118.
- 2605 Lee, Suk-HO et al. (July 2000). “Differences in Ca<sup>2+</sup> buffering properties between excitatory  
2606 and inhibitory hippocampal neurons from the rat”. In: *The Journal of Physiology* 525.
- 2607 Litwin-Kumar, Ashok, Maurice Chacron, and Brent Doiron (Sept. 2012). “The Spatial Struc-  
2608 ture of Stimuli Shapes the Timescale of Correlations in Population Spiking Activity”. In:  
2609 *PLoS computational biology* 8, e1002667.
- 2610 Maravall, M et al. (May 2000). “Estimating intracellular calcium concentrations and buffer-  
2611 ing without wavelength ratioing”. In: *Biophysical Journal* 78.5, pp. 2655–2667.
- 2612 Maugis, Pa (Jan. 2014). “Event Conditional Correlation: Or How Non-Linear Linear Depen-  
2613 dence Can Be”. In:
- 2614 Meilă, Marina (2007). “Comparing clusterings—an information based distance”. In: *Journal*  
2615 *of Multivariate Analysis* 98.5, pp. 873 –895.
- 2616 Murray, John D. et al. (2014). “A hierarchy of intrinsic timescales across primate cortex”. In:  
2617 *Nature Neuroscience* 17.12, pp. 1661–1663.
- 2618 Neher, E. and G. J. Augustine (1992). “Calcium gradients and buffers in bovine chromaffin  
2619 cells”. eng. In: *The Journal of physiology* 450. 1331424[pmid], pp. 273–301.

- 2620 O'Donnell, Cian et al. (Jan. 2017). "The population tracking model: a simple, scalable statistical model for neural population data". English. In: *Neural Computation* 29.1, pp. 50–93.
- 2623 Okun, Michael et al. (2015). "Diverse coupling of neurons to populations in sensory cortex". In: *Nature* 521.7553, pp. 511–515.
- 2625 Ouzounov, Dimitre G. et al. (2017). "In vivo three-photon imaging of activity of GCaMP6-labeled neurons deep in intact mouse brain". eng. In: *Nature methods* 14.4. 28218900[pmid], pp. 388–390.
- 2628 Patterson, Carlyn A. et al. (2014). "Similar adaptation effects in primary visual cortex and area MT of the macaque monkey under matched stimulus conditions". In: *Journal of Neurophysiology* 111.6. PMID: 24371295, pp. 1203–1213.
- 2631 Peron, Simon P. et al. (2015). "A Cellular Resolution Map of Barrel Cortex Activity during Tactile Behavior". In: *Neuron* 86.3, pp. 783–799.
- 2633 Pnevmatikakis, E.A. et al. (Jan. 2016). "Simultaneous Denoising, Deconvolution, and Demixing of Calcium Imaging Data". In: *Neuron* 89.2, pp. 285–299.
- 2635 Pnevmatikakis, Eftychios et al. (Nov. 2013). "Bayesian spike inference from calcium imaging data". In: *Conference Record - Asilomar Conference on Signals, Systems and Computers*.
- 2637 Pnevmatikakis, Eftychios et al. (Sept. 2014). "A structured matrix factorization framework for large scale calcium imaging data analysis". In:
- 2639 Schneidman, Elad et al. (2006). "Weak pairwise correlations imply strongly correlated network states in a neural population". eng. In: *Nature* 440.7087. 16625187[pmid], pp. 1007–1012.
- 2642 Shannon, C. E. (1948). "A Mathematical Theory of Communication". In: *Bell System Technical Journal* 27.3, pp. 379–423.
- 2644 Shimazaki, Hideaki et al. (2012). "State-space analysis of time-varying higher-order spike correlation for multiple neural spike train data". eng. In: *PLoS computational biology* 8.3. 22412358[pmid], e1002385–e1002385.
- 2647 Staude, Benjamin, Sonja Grün, and Stefan Rotter (2010). "Higher-Order Correlations and Cumulants". In: *Analysis of Parallel Spike Trains*. Ed. by Sonja Grün and Stefan Rotter. Boston, MA: Springer US, pp. 253–280.
- 2650 Stein, Astrid von and Johannes Sarnthein (2000). "Different frequencies for different scales of cortical integration: from local gamma to long range alpha/theta synchronization". In: *International Journal of Psychophysiology* 38.3, pp. 301 –313.

## Bibliography

---

- 2653 Steinmetz, Nick, Matteo Carandini, and Kenneth D. Harris (2019). "Single Phase3" and  
2654 "Dual Phase3" *Neuropixels Datasets*.
- 2655 Steinmetz, Nick et al. (Mar. 2019). "Eight-probe Neuropixels recordings during spontaneous  
2656 behaviors". In:
- 2657 Stevenson, Ian H. and Konrad P. Kording (2011). "How advances in neural recording affect  
2658 data analysis". In: *Nature Neuroscience* 14.2, pp. 139–142.
- 2659 Stringer, Carsen et al. (2019). "Spontaneous behaviors drive multidimensional, brainwide  
2660 activity". In: *Science* 364.6437.
- 2661 Tada, Mayumi et al. (2014). "A highly sensitive fluorescent indicator dye for calcium imaging  
2662 of neural activity in vitro and in vivo". In: *European Journal of Neuroscience* 39.11,  
2663 pp. 1720–1728.
- 2664 Tian, Lin et al. (2009). "Imaging neural activity in worms, flies and mice with improved  
2665 GCaMP calcium indicators". eng. In: *Nature methods* 6.12. 19898485[pmid], pp. 875–  
2666 881.
- 2667 Tkačik, Gašper et al. (2014). "Searching for collective behavior in a large network of sen-  
2668 sory neurons". eng. In: *PLoS computational biology* 10.1. 24391485[pmid], e1003408–  
2669 e1003408.
- 2670 Treves, Alessandro and Stefano Panzeri (1995). "The Upward Bias in Measures of Informa-  
2671 tion Derived from Limited Data Samples". In: *Neural Computation* 7.2, pp. 399–407.
- 2672 Vinh, Nguyen Xuan, Julien Epps, and James Bailey (Dec. 2010). "Information Theoretic  
2673 Measures for Clusterings Comparison: Variants, Properties, Normalization and Correc-  
2674 tion for Chance". In: *J. Mach. Learn. Res.* 11, 2837–2854.
- 2675 Vogelstein, Joshua T. et al. (Oct. 2010). "Fast nonnegative deconvolution for spike train infer-  
2676 ence from population calcium imaging". In: *Journal of neurophysiology* 104.6, 295–300.
- 2677 Wierzynski, Casimir M. et al. (2009). ""State-Dependent Spike-Timing Relationships be-  
2678 tween Hippocampal and Prefrontal Circuits during Sleep"". In: "Neuron" "61" ."4", "587  
2679 –596".
- 2680 Zariwala, Hatim A. et al. (2012). "A Cre-dependent GCaMP3 reporter mouse for neuronal  
2681 imaging in vivo". eng. In: *The Journal of neuroscience : the official journal of the Society  
2682 for Neuroscience* 32.9. 22378886[pmid], pp. 3131–3141.
- 2683 Zou, Hui and Trevor Hastie (2005). "Regularization and variable selection via the Elastic  
2684 Net". In: *Journal of the Royal Statistical Society, Series B* 67, pp. 301–320.